Study of High Spin States In Nuclei Near Z=82

By

Tanmoy Roy

Enrolment No: PHYS04201104003

Variable Energy Cyclotron Centre, Kolkata

A thesis submitted to

The Board of Studies in Physical Sciences

In partial fulfillment of requirements

For the Degree of

DOCTOR OF PHILOSOPHY

of

HOMI BHABHA NATIONAL INSTITUTE

February, 2017

Homi Bhabha National Institute[1]

Recommendations of the Viva Voce Committee

As members of the Viva Voce Committee, we certify that we have read the dissertation prepared by **Tanmoy Roy** entitled "**Study of High Spin States In Nuclei Near Z=82**" and recommend that it may be accepted as fulfilling the thesis requirement for the award of Degree of Doctor of Philosophy.

Chairman – Dr. S.R. Banerjee, VECC	**Date:** 08/5/2017
Guide / Convener – Dr. Gopal Mukherjee, VECC	**Date:** 08/05/17
Co-guide - <Name> (if any)	**Date:**
Examiner – Prof. A.K. Jain, IIT Roorkee (A. K. Jain)	**Date:** 8/5/2017
Member 1- Dr. Asimananda Goswami, SINP	**Date:** 08.05.2017
Member 2- Dr. Tilak Ghosh, VECC	**Date:** 08.05.17

Final approval and acceptance of this thesis is contingent upon the candidate's submission of the final copies of the thesis to HBNI.

I/We hereby certify that I/we have read this thesis prepared under my/our direction and recommend that it may be accepted as fulfilling the thesis requirement.

Date: 08/05/2017

Place: Kolkata

<Signature>
Co-guide (if applicable)

<Signature>
Guide

[1] This page is to be included only for final submission after successful completion of viva voce.

STATEMENT BY AUTHOR

This dissertation has been submitted in partial fulfillment of requirements for an advanced degree at Homi Bhabha National Institute (HBNI) and is deposited in the Library to be made available to borrowers under rules of the HBNI.

Brief quotation from this dissertation are allowable without special permission, provided that accurate acknowledgement of source is made. Requests for permission for extended quotation from or reproduction of this manuscript in whole or in part may be granted by the Competent Authority of HBNI when in his or her judgement the proposed use of the material is in the interests of scholarship. In all other instances, however, permission must be obtained from the author.

Tanmoy Roy

Tanmoy Roy

DECLARATION

I, hereby declare that the investigation presented in the thesis has been carried out by me. The work is original and has not been submitted earlier as a whole or in part for a degree/diploma at this or any other Institution/University.

Tanmoy Roy .

Tanmoy Roy

ACKNOWLEDGMENTS

This journey of last five years in my life was like a roller coaster ride, full of surprises and a bag of mixed emotions. In this expedition, I would like to express my sincere gratitude to my supervisor Dr. Gopal Mukherjee for his constant guidance and inspiration. During the course of time, his various advises not only helped me to rectify my mistakes but also helped me to look at things from different perspectives.

I am very much indebted to the directors of VECC, Prof. Rakesh Kumar Bhandari, Prof. Dinesh Kumar Srivastava, Raja Ramanna Fellow, Prof. Alok Chakrabarti and Shri Amitava Roy for providing appropriate working atmosphere and full fledged facilities to the research scholars to carry out their research work efficiently. At the same time I am extremely grateful to Prof. Amit Roy, Prof. Sailajananda Bhattacharya, Prof. S.R. Banerjee, Head, Physics Group, VECC, Prof. Chandana Bhattacharya, Head, Experimental Nuclear Physics Division, VECC, Prof. Asimananda Goswami from Saha Institute of Nuclear Physics for their encouragement and critical advises.

Special thanks to Prof. Jane Alam, DEAN, HBNI, VECC, Dr. Sarmishtha Bhattacharyya, Dr. Tumpa Bhattacharjee, Dr. Rudrajyoti Palit from TIFR, Dr. N. Madhavan and Dr. S. Nath from IUAC for their suggestions and help whenever I needed them during my Ph. D work.

It was a great pleasure to be able to participate in various experiments with Dr. T.K. Ghosh, Dr. K. Banerjee, Dr. S. Kundu, Dr. T.K. Rana, Dr. S. Mukhopadhyay, Dr. S. Pal, Dr. D. Pandit, Dr. A. Dey, Dr. A. Dhal, Dr. H. Pai, Dr. S. Dasgupta, Dr. M.R. Gohil, Pratap Roy, Ratnesh Pandey, Dr. V. Shrivastava, Dr. B. Dey, Soumik, Debasish, Santu, Arijit, Jai da, Jayanta, Amiya, Anindita di, Pulak da, Ratan da and Pintu, members of the nuclear experimental physics group which enabled me to learn various experimental nitty-gritty from a very close quarter.

The help of all the collaborators in the present work, from different institutions (VECC, TIFR, IUAC, SINP, UGC-DAE Kolkata) and the target making laboratory members of

IUAC, Mr. Abhilash and Dr. Kabiraj is gratefully acknowledged. The effort of the operators of the accelerators at VECC, TIFR and IUAC, and all the participating group in the CLOVER Array Collaboration are also acknowledged.

I was extremely fortunate to have friends like Abhirup, Somnath, Debojit, Subhendu, Arindam, Asif name a few and my juniors Asgar, Utsab, Debasish, Arunava, Noor, Sarwar, Rana, Pabrisa, S. Mukherjee, Pingal, Rajendra, Dipak, Homenath, Ajit, Shabnam, Ranabir, Safikul, Soumen, Santanu, Sanchari, Mitali, Shreyasi, Sumit, Mahfuzur with whom I have shared a lot of joyful moments in last few years.

Last but not least, I am very grateful to my father, mother and younger brother for their unconditional love and support through out this journey without which it would have not reach to its culmination.

I sincerely apologize inadvertent omission of any name from the above list of acknowledgement.

Tanmoy Roy

Tanmoy Roy

VECC, Kolkata

SYNOPSIS

Nuclei with magic number of protons and neutrons show spherical structures whereas the nuclei with proton and neutron numbers near the mid-shell are mostly deformed. The heaviest known magic numbers for proton and neutron are Z = 82 and N = 126, respectively.^{208}Pb with Z = 82 and N =1 26, is the heaviest stable doubly magic nucleus. The Tl, Pb, and Bi nuclei around this doubly magic ^{208}Pb are mostly spherical. However, this spherical symmetry is broken for the lighter isotopes of these nuclei when the neutron Fermi level moves towards the mid-shell. The shape of a nucleus and the generation of angular momenta in a nucleus depends sensitively on the single particle nucleonic levels around the Fermi level. The high-j orbitals are specifically important, not only for determining the shape of a nucleus near the ground state but also for the high spin structure of a nucleus. The low (high) components of a high-j orbital come down in energy very sharply for prolate (oblate) deformation. So, these orbitals have large shape driving effect. Moreover, these orbitals experience larger Coriolis force for a rotating nucleus and thereby becomes accessible at higher angular momenta which affects the high spin states of a nucleus. On the other hand, if the high-j orbitals are available near the Fermi level of a nucleus, higher spin states can be generated at a relatively lower excitation energy where lower energy states have much smaller angular momenta. This gives rise to spin-gap isomers.

For the nuclei in mass A=190 region with proton number near Z=82, the intruder $\pi h_{9/2}$ (9/2[505], 1/2[541]) and $\pi i_{13/2}$ (13/2$^+$[606], 1/2$^+$ [660]) orbitals come down in energy for both oblate and prolate nuclear deformations. Whereas, in the neutron sector, the $i_{13/2}$(1/2$^+$[660], 13/2$^+$[606]) orbitals compete with $p_{3/2}$ (3/2[512], 1/2[521]) and $f_{5/2}$ (5/2[503], 1/2[510]) for neutron occupation.

In the present thesis work, the motivation was the experimental investigation of the effect and relative importance of these high-j proton and neutron orbitals on the high spin states in the nuclei near proton magic number Z = 82. For this study, two systems were chosen, ^{195}Bi and ^{195}Tl where proton Fermi level lies just above and below the Z=82 shell closure, respectively. The high-spin states in these nuclei were studied by populating them via heavy-ion fusion evaporation reaction and the de-excited gamma- rays were detected by high-resolution clover HPGe detectors.

For Bismuth nuclei with Z=83, the proton Fermi level lies just above the Z = 82 shell closure and near the high-j $h_{9/2}$ orbital. Because of the proximity of the spherical shell closures at Z = 82 and N = 126, the heavier Bi isotopes with neutron number N $\geq$ 114 are spherical and the high spin states are mostly generated by single particle excitation [1,2]. However, rotational bands, indicating deformed shape, have been observed in ^{191,193}Bi isotopes with neutron number N $\leq$ 112 [3,11]. This is apparently due to the involvement of the high-j $i_{13/2}$ neutron orbital which becomes available for neutron number N $<$ 114. In the transitional nucleus ^{195}Bi a rotational band based on $13/2^{+}$ state ($\pi i_{13/2}$ configuration) has been observed indicating the onset of deformation at N = 112 for Bi isotopes. However, the information on the high spin states in this nucleus is very limited as only 9 (with one tentative state) excited states were known prior to the present work [5]. This also include a long-lived isomeric state having spin parity of $29/2^{(-)}$ with half-life of 750 ns at an excitation energy of about 2.4 MeV. A few transitions bypassing this isomeric state were also known but the high spin states were known only up to less than 3 MeV. Therefore, the effect of high-j unpaired neutron orbitals are not known in this important transitional nucleus. In comparison to ^{195}Bi, the information of high spin states in neighouring odd-A Bi isotopes are very rich with the observation of several band structures up to an excitation energy more than 5.5 MeV and 45/2 $\hbar$ of angular momentum. Moreover, several long-lived isomeric states were also known in this nucleus with half-lives ranging from 3 μs to 85 μs. Because of the presence of these high-j orbitals, several isomeric states are known in this mass region. For example, $29/2^{-}$ state is a well-known isomeric state in $^{195-201}$Bi isotopes with configuration $\pi h_{9/2} \otimes \nu_{12}{}^{+}$. There is also $31/2^{-}$ known isomeric state in Bi isotope with configuration $\pi i_{13/2} \otimes \nu_{9}{}^{-}$. There is also $31/2^{-}$ known isomeric state in Bi isotope with configuration $\pi i_{13/2} \otimes \nu_{9}{}^{-}$.

There have been several attempts to produce the high spin states in ^{195}Bi nucleus with various heavy-ion fusion evaporation reactions using ^{16}O, ^{19}F and ^{20}Ne projectiles on various targets but the high spin states could not be populated beyond those limited number of states as mentioned above, although the projectiles could be able to populate angular momentum more than 40 $\hbar$. It was, therefore, presumed that there may exists a high-spin long lived isomer in ^{195}Bi which prevented the observation of the higher spin states.

In this thesis work, an experiment was designed to preferentially identify this possible high-spin isomer and its decay. The reaction ^{169}Tm(^{30}Si,4n)^{195}Bi at a beam energy of 146 MeV on the target was used to populate the high spin states of this nucleus. Prior to these ^{193}Bi was populated with ^{169}Tm(^{30}Si,6n)^{193}Bi fusion evaporation reaction at beam energy of 168 MeV as a test case. Since the interest was to detect isomer, the decay γ-rays were detected at the focal plane of a Recoil separator. The experiment was, therefore, performed at the Pelletron-Linac facility at Inter University Accelerator Centre (IUAC), New Delhi using the HYbrid Recoil mass Analyzer (HYRA). The residues were separated from the large background of fission fragments by HYRA and brought at the focal plane where they were implanted on Si-pad detectors after passing through a Multi Wire Proportional Counter (MWPC). The delayed γ-rays were detected using a clover HPGe detector. There was another clover HPGe detector placed near the target chamber.

The time difference (ΔT) between the arrival of the residues, obtained from the MWPC, and the detection of a γ-ray in the clover detector was used to find the half-life of the isomer. For this, a matrix between the energy of the γ-rays, E_γ and ΔT was formed from which the ΔT spectrum was projected, gated by various decay gamma-rays. The method was tested from the observation of the known decay gamma- rays from a 3-μs isomer in ^{193}Bi and reproducing its half-life. The observation of the 457-keV prompt γ-ray of ^{195}Bi at the focal plane clover detector confirmed the presence of a new higher-spin isomer in this nucleus with half-life longer or of the order of the transit time of ^{195}Bi residues from the target site to the focal plane. The time of flight of evaporation residue at HYRA was measured to be 1.53(9) μs. A half-life of 1.6(1)μs was obtained for the new isomer by fitting the ΔT spectrum gated by 457-keV γ-ray. This was confirmed from other ΔT spectra gated by other transitions. Three new transitions were also observed in this nucleus and the excitation energy and most likely spin- parity of the new isomer was also established as 3336 keV and $(31/2^-)$, respectively. From a systematic comparison of the configuration and excitation energy of nearby high spin isomers in the neighbouring Bi isotopes, the configuration of the new isomer has been assigned as $\pi i_{13/2} \otimes \nu_9{}^-$. The Total Routhian Surface (TRS) calculations for this three quasi particle configuration of the new high spin isomer suggest an oblate deformation. The same calculations for other configurations in ^{195}Bi and even-even ^{194}Pb core indicated that the proton $i_{13/2}$ orbital has large shape driving effect towards the oblate shape in these nuclei.

In the case of Thallium (Tl) nuclei with Z = 81, rotational bands corresponding to oblate deformation has been reported in $^{191-201}$Tl isotopes [6–10] based on the proton in the 9/2[505] intuder orbital. The decoupled bands based on the $\pi h_{9/2}$ intruder orbital with prolate deformation has been reported in the lighter isotopes of ^{187,189}Tl [6, 11]. Also, the neutron pair alignments of the oblate bands based on the $\pi h_{9/2}$ configuration in ^{191,193}Tl [6, 7] take place in $\nu i_{13/2}$ orbital. As neutron number increases to 114, in case of Tl, the $\nu i_{13/2}$ orbital closes up and nearby $p_{3/2}$ and $f_{5/2}$ orbitals open up for neutron occupation. Therefore, ^{195}Tl can be considered as a transitional nucleus in this respect. Moreover, as the high-j orbitals exist near the proton and neutrons Fermi levels for these nuclei and the proton particle angular momentum (j_π) and neutron hole angular momentum (j_ν) are mutually perpendicular, they satisfy the criteria for the emergence of exotic high-spin phenomena, like magnetic rotation and nuclear chirality for near spherical and triaxial deformed shapes. Some of these bands are reported for the odd-odd Tl isotopes in this mass region. However, the odd-A nuclei with N = 114 are not well studied. The previous investigation of the high spin states in ^{195}Tl was done by using the ^{197}Au(α, 6n)^{195}Tl fusion evaporation reaction and using only four Ge(Li) detectors [12]. Therefore, high-spin states could not be produced in that work and was therefore, limited to below band crossing region of the $\pi h_{9/2}$[505] band with no information on the neutron pair alignment or other exotic high-spin phenomena. Therefore, in order to investigate in detail about the high-spin states in ^{195}Tl, it has to be populated by heavy-ion induced reaction to generate higher spins and also using a more efficient gamma detector array to observe the weakly populated states.

In order to investigate the high-spin states in ^{195}Tl in this thesis work, an experiment was performed at the TIFR-BARC pelletron facility at Mumbai, using heavy-ion induced fusion evaporation reaction ^{185,187}Re(^{13}C, xn)^{195}Tl at 75 MeV of beam energy. The Indian National Gamma Array (INGA) consisted of 15 Compton-suppressed clover (HPGe) detectors were used to detect the prompt gamma-rays. Data were taken with digital data acquisition system, based on Pixie-16 modules. E_γ-E_γ matrix, E_γ-E_γ-E_γ cube were made for further analysis to build the level scheme from γ-ray coincidence and intensity relations. For spin assignment of each level from the multipolarity of the de-exciting gamma-rays, directional correlation ratio (RDCO) matrix was prepared with 157^0 detector data on one axis and 90^0 data on other axis for analysis. Similarly, for the parity assignment from the type (E/M) of the γ-rays, two integrated polarization asymmetry (IPDCO) ratio matrices were made for perpendicular and parallel scattered events in the crystals of the clover detectors.

In this work, the previously known level scheme of ^{195}Tl has been extended considerably with the placement of 57 new transitions. The ground state band based on $\pi h_{9/2}$ orbital, which was known up to $27/2^-$ state has been extended beyond first band crossing up to $39/2^-$ $\hbar$ spin and $\sim$ 5.3 MeV of excitation energy. The three-quasi particle (qp) s-band above band-crossing is accompanied by a very weak band structure with several interconnecting transitions, which has been interpreted as a possible candidate of a gamma band to the former.

With the added advantage of multi-polarity (RDCO) and polarization (IPDCO) measurement using clover HPGe detectors, compared to earlier angular distribution measurement only, the type and multipolarity of some the known transitions have been altered and consequently, the spin-parity of the concerned levels are modified. Because of these modifications, the configuration of the three-qp band based on $15/2^-$ state has been modified from $\pi h_{9/2} \otimes \nu i_{13/2},\ \nu j$ to $\pi i_{13/2} \otimes \nu i_{13/2},\ \nu j$, where νj is $\nu(p_{3/2},\ f_{5/2})$. It has been observed for the first time that the higher energy part of this band above $33/2^-$ $\hbar$ spin has been bifurcated into two bands. The stronger populated one is the continuation of the 3-qp band after another neutron pair alignment attains 5-qp configuration. The other weakly populated band is connected to the former through several interconnecting gamma transitions. These two bands are quite degenerate to each other based on 5-qp $\pi i_{13/2} \otimes \nu i^{-3}_{13/2}(p_{3/2}f_{5/2})^{-1}$ configuration. The total Routhian surface calculation done for the above stated configuration shows the presence of a triaxial minimum. These mutually orthogonal particle-hole angular momentum along with the core rotational angular momentum forms a chiral geometry. Therefore, these two bands seems to be candidates of doubly degenerate bands which needs to be confirmed through lifetime measurement.

Apart from these, a few number of excited states have been identified in this nucleus which do not show any regular pattern. These are interpreted as originated from the single particle excitations in the $\pi s_{1/2}$, $\pi d_{3/2}$, $\pi i_{13/2}$, etc., however, no rotational band has been observed based on the $\pi i_{13/2}$ configuration in this nucleus.

In conclusion, the present knowledge on the high spin states in ^{195}Bi and ^{195}Tl have been extended substantially in the present thesis work. The dilemma of non-observance of the high-spin states in ^{195}Bi has been solved by identifying a new long-lived high-spin isomer with a half-life of 1.6(1) μs. An oblate deformation is suggested for this isomeric state. The decay pattern of the isomer has also been identified. On the other hand, in ^{195}Tl, the level scheme has been extended beyond band-crossing in the ground band and several new band structures have been identified with the inclusion of 57 new gamma- transition. In this thesis work, it has been observed that the $\pi i_{13/2}$ level has more deformation driving effect (towards oblate shape) for the Bismuth nucleus in which the Fermi level lies above the Z = 82 shell closure, whereas no rotational band based on this configuration has been observed in Thallium nucleus for which the Fermi level lies below the Z = 82 shell closure. However, a rich variety of high-spin level structures have been observed in the ^{195}Tl nucleus unlike in ^{195}Bi in the low as well as higher excitation energies. This needs to be further investigated whether it is due to the presence of isomer or because of more competition of positive parity $\nu i_{13/2}$ and negative $\nu(p_{3/2}f_{5/2})$ orbitals for the neutron number N = 114 in ^{195}Tl than for the neutron number N = 112 in ^{195}Bi nucleus.

The present thesis work also opens up the possibilities of further investigation on some of the interesting aspects in the nuclei in this region. For example, the prediction of oblate deformation of the highest spin isomer in ^{195}Bi identified in this work, needs to be confirmed by establishing the band structure above this isomer. On the other hand, more works are needed (in particular, life-time measurements) to understand the nature of the possible doubly-degenerate band-like structures in ^{195}Tl. Moreover, the absence of rotational band based on $\pi h_{9/2}$ orbital in ^{195}Bi and the absence of rotational band based on $\pi i_{13/2}$ orbital in ^{195}Tl needs to be understood from theoretical approaches.

Bibliography

[1] G.K. Mabala et al., Eur. Phys. J. **A 25**, 49 (2005).

[2] W. F. Piel et al., Phys. Rev. **C 31**, 2087 (1985).

[3] P. Nieminen et al., Phys. Rev. **C 69**, 064326 (2004).

[4] A. Herzáň et al., Phys. Rev. **C 92**, 044310 (2015).

[5] H. Pai et al., Phys. Rev. **C 85**, 064317 (2012).

[6] W. Reviol et al., Physica Scripta **56**, 167 (1995).

[7] W. Reviol et al., Nucl. Phys **A 548**, 331 (1992).

[8] H. Pai et al., Phys. Rev. **C 88**, 064302 (2013).

[9] N. Mărginean et al., Eur. Phys. J. **A 46**, 329 (2010).

[10] S. Das Gupta et al., Phys. Rev. **C 88**, 044328 (2013).

[11] W. Reviol et al., Phys. Rev. **C 49**, R587 (2013).

[12] R. M. Lieder et al., Nucl. Phys **A 299**, 255 (1978).

LIST OF PUBLICATIONS

(A) Relevant to the present Thesis

In referred journals :

1. **A new high-spin isomer in ^{195}Bi.**

   T. Roy, G. Mukherjee, N. Madhavan, T.K. Rana, Soumik Bhattacharya, Md. A. Asgar, I. Bala, K. Basu, S.S. Bhattacharjee, C. Bhattacharya, S. Bhattacharya, S. Bhattacharyya, J. Gehlot, S.S. Ghugre, R.K. Gurjar, A. Jhingan, R. Kumar, S. Muralithar, S. Nath, H. Pai, R. Palit, R. Raut, R.P. Singh, A.K. Sinha, T. Varughese. Eur. Phys. J.A **51**, 153 (2015).

2. **Study of The Rotational Bands In ^{195}Tl**

   T. Roy, G. Mukherjee, Md. A. Asgar, H. Pai, M. R. Gohil, C. Bhattacharya, S. Bhattacharya, Soumik Bhattacharya, S. Bhattacharyya, T. Bhattacharjee, R. Palit, S. Saha, J. Sethi, Shital Thakur, B. S. Naidu, S. V. Jadav, R. Dhonti, A. Goswami. **Manuscript under prepartion.**

Results Reported in Conferences/Symposia :

1. **Shears Band based on a large multi-qp configuration in ^{195}Tl**

   T. Roy, H. Pai, Md. A. Asgar, G.Mukherjee, A. Dhal, and C. Bhattacharya. Proceedings of the DAE-BRNS Symp. on Nucl. Phys. Vol **60**, 262 (2015).

Tanmoy Roy.

2. **Rotational Bands in ^{195}Tl**

   T. Roy, H. Pai, Md. A. Asgar, G. Mukherjee, S. Bhattacharyya, M.R Gohil, T. Bhattacharjee, C. Bhattacharya, R. Palit, S. Saha, J. Sethi, T. Trivedi, Shital Thakur, B.S Naidu, S.V Jadav, R. Donthi, A. Goswami, and S. Chanda.

   Proceedings of the DAE Symposium on nuclear physics, Vol **59**, 88 (2014).

3. **A New Isomer in ^{195}Bi Identified at the Focal Plane of HYRA**

   T. Roy, G. Mukherjee, Md. A. Asgar, Soumik Bhattacharya, H. Pai, T.K Rana, S. Bhattacharyya, C. Bhattacharya, S. Bhattacharya, N. Madhavan, S. Nath, R.P. Singh, A. Jhingan, S. Muralithar, R. Kumar, J. Ghelot, T. Varughese, I. Bala, R.K. Gurjar, A.K. Sinha, S.S. Ghugre, R. Raut, S.S. Bhattacharjee, K. Basu, R. Palit.

   Proceedings of the DAE Symposium on nuclear physics, Vol **59**, 126 (2014).

Tanmoy Roy ,

(B) Other publications (in referred journals)

(a) **Return of backbending in 169 Tm and the effect of the N = 98 deformed shell gap**

Md. A. Asgar , **T. Roy**, G. Mukherjee, G. H. Bhat, J. A. Sheikh, A. Dhal, Soumik Bhattacharya, S. Bhattacharyya, C. Bhattacharya, S. Bhattacharya, A. Chaudhuri, K. Banerjee, S. Kundu, S. Manna, R. Pandey, J.K. Meena, R. Palit, S. Biswas, S. Saha, J. Sethi, P. Singh and D. Choudhury.

Phys. Rev. C **95**, 031304(R) (2017).

(b) **Deformed band structures at high spin in ^{200}Tl**

Soumik Bhattacharya, S. Bhattacharyya, S. Das Gupta, H. Pai, G. Mukherjee, R. Palit, F. R. Xu, Q. Wu, A. Shrivastava, Md. A. Asgar, R. Banik, T. Bhattacharjee, S. Chanda, A. Chatterjee, A. Goswami, V. Nanal, S. K. Pandit,

S. Saha, J. Sethi, **T. Roy**, and S. Thakur.

Phys. Rev. C **95**, 014301 (2017).

(c) **Physics of the Exotic Shape-Coexistence in the Presence of Tetrahedral Symmetry an Experimental Study of the Excited Bands in ^{160}Yb**

A. Saha, T. Bhattacharjee, D. Curien, J. Dudek, K. Mazurek, A. Góźdź, S. Tagami, Y. R. Shimizu, S. R. Banerjee, S. Rajbanshi, A. Bisoi, G. de Angelis, Soumik Bhattacharya, S. Bhattacharyya, S. Biswas, A. Chakraborty, S. Das Gupta, B. Dey, G. Duchene, A. Goswami, D. Mondal, D. Pandit, R. Palit, **T. Roy**, R. P. Singh, M. Saha Sarkar, S. Saha, and J. Sethi.

Communicated to Phys. Rev. C.

(d) **Survival of cluster correlation in dissipative binary breakup of ^{24,25}Mg**

S. Manna, T. K. Rana, C. Bhattacharya, S. Bhattacharya, S. Kundu, K. Banerjee, Pratap Roy, R. Pandey, Vishal Srivastava, A. Chaudhuri,**T. Roy**, T. K. Ghosh, G. Mukherjee, J. K. Meena, S. K. Pandit, K. Mahata, A. Shrivastava, and V. Nanal.

Phys. Rev. C **94**, 051601(R) (2016).

(e) **Fission fragment mass distributions in reactions populating ^{200} Pb**

A. Chaudhuri, A. Sen, T. K. Ghosh, K. Banerjee, Jhilam Sadhukhan, S. Bhattacharya, P. Roy, **T. Roy**, C. Bhattacharya, Md. A. Asgar, A. Dey, S. Kundu, S. Manna, J. K. Meena, G. Mukherjee, R. Pandey, T. K. Rana, V. Srivastava,

R. Dubey, Gurpreet Kaur, N. Saneesh, P. Sugathan, and P. Bhattacharya.

Phys. Rev. C **94**, 024617 (2016).

(f) **Experimental investigation of T = 1 analog states of ^{26} Al and ^{26} Mg**

Vishal Srivastava, C. Bhattacharya, T. K. Rana, S. Manna, S. Kundu, S. Bhattacharya, K. Banerjee, P. Roy, R. Pandey, G. Mukherjee, T. K. Ghosh, J. K. Meena, **T. Roy**, A. Chaudhuri, M. Sinha, A. K. Saha, Md. A. Asgar, A. Dey, Subinit Roy, and Md. M. Shaikh.

Phys. Rev. C **93**, 044601 (2016).

(g) **Experimental study of 26 Al through the 1n pick-up reaction ^{27} Al(d, t)**

Vishal Srivastava, C. Bhattacharya, T. K. Rana, S. Manna, S. Kundu, S. Bhattacharya, K. Banerjee, P. Roy, R. Pandey, G. Mukherjee, T. K. Ghosh, J. K. Meena, **T. Roy**, A. Chaudhuri, M. Sinha, A. K. Saha, Md. A. Asgar, A. Dey, Subinit Roy, and Md. M. Shaikh.

Phys. Rev. C **91**, 054611 (2015).

(h) **No influence of a N = 126 neutron-shell closure in fission-fragment mass distributions**

A. Chaudhuri, T. K. Ghosh, K. Banerjee, S. Bhattacharya, Jhilam Sadhukhan, S. Kundu, C. Bhattacharya, J. K. Meena, G. Mukherjee, A. K. Saha, Md. A. Asgar, A. Dey, S. Manna, R. Pandey, T. K. Rana, P. Roy, **T. Roy**, V. Srivastava, P. Bhattacharya, D. C. Biswas, B. N. Joshi, K. Mahata, A. Shrivastava, R. P. Vind, S. Pal, B. R. Behera, and Varinderjit Singh.

Phys. Rev. C **92**, 041601(R) (2015).

(i) **Direct evidence of washing out of nuclear shell effects**

A. Chaudhuri, T. K. Ghosh, K. Banerjee, S. Bhattacharya, Jhilam Sadhukhan, C. Bhattacharya, S. Kundu, J. K. Meena, G. Mukherjee, R. Pandey, T. K. Rana, P. Roy, **T. Roy**, and V. Srivastava.

Phys. Rev. C **91**, 044620 (2015).

Results Reported in Conferences/Symposia :

(a) **Decay Study of Neutron-rich ^{43}K using Total Absorption TAGS and High Resolution HRGS Gamma Spectroscopy Methods**

A. Dhal, G. Mukherjee, M. Bhattacharjee, V. Naik, S. Mukhopadhyay, D. Pandit, S. Pal, D. Mondal, P. Karmakar, **T. Roy**, Md. A. Asgar, Soumik Bhattacharya, S. Bhattacharyya, C. Bhattacharya, S. R. Banerjee, A. Chakrabarti.

Proceedings of the DAE-BRNS Symp. on Nucl. Phys., Vol **61** 96 (2016).

(b) **VECC array for NUclear Spectroscopy VENUS**

Soumik Bhattacharya, R. Banik, S. S. Alam, A. Saha, Md. A. Asgar, **T. Roy**, A. Chowdhury, I. Sheikh, P. Mukhopadhyay, A. Dhal, T. Bhattacharjee, S. Bhattacharyya, G. Mukherjee, S. Mukhopadhyay, D. Mondal, D. Pandit, S. Pal, S.R. Banerjee.

Proceedings of the DAE-BRNS Symp. on Nucl. Phys., Vol **61** 98 (2016).

(c) **Oblate band structure based on π $h_{9/2}$ orbital in ^{199}Tl**

Soumik Bhattacharya, S. Bhattacharyya, R. Banik, G. Mukherjee, S. Das Gupta, S. S. Alam, A. Dhal, Md. A. Asgar, **T. Roy**, A. Saha, T. Bhattacharjee, S. Mukhopadhyay, D. Pandit, D. Mondal, S. Pal, S. R. Banerjee.

Proceedings of the DAE-BRNS Symp. on Nucl. Phys., Vol **61** 188 (2016).

(d) **Half-life and β -feeding measurements of ^{217}Po by γ -spectroscopy method**

A. Dhal, R. Ghosh, A. G. Nair, G. Mukherjee, Md. A. Asgar, **T. Roy**, T. K. Rana, T. K. Ghosh, K. Banerjee, S. Kundu, R. Pandey, Pratap Roy, S. Manna, A. Sen, A. Dey, J. K. Meena, J. K. Sahoo, A. K. Saha, R. Banik, Soumik Bhattacharya, A. Saha, S. S. Alam, D. Mondal, D. Pandit, S. Mukhopadhyay, S. Pal, T. Bhattacharjee, S. Bhattacharyya, C. Bhattacharya, S. R. Banerjee.

Proceedings of the DAE-BRNS Symp. on Nucl. Phys., Vol **61** 266 (2016).

(e) **Study of multi-quasiparticle band structures in ^{197}Tl using α beam**

G. Mukherjee, S. Nandi, H. Pai, **T. Roy**, Md. A. Asgar, A. Dhal, R. Banik, Soumik Bhattacharya, A. Saha, S. S. Alam, S. Bhattacharyya, C. Bhattacharya, Pratap Roy, T. K. Ghosh, S. Kundu, K. Banerjee, T. K. Rana, R. Pandey, S. Manna, A. Sen, S Pal, S Mukhopadhyay, D. Pandit, D. Mondal, T. Bhattacharjee, A. Dey, J. K. Meena, A. K. Saha, J. K. Sahoo, R. Mondal Saha, A. Choudhury, S.R Banerjee.

Proceedings of the DAE-BRNS Symp. on Nucl. Phys., Vol **61** 270 (2016).

(f) **Study of nuclear structure in odd-odd ^{122,124}I**

S. S. Alam, A. Saha, T. Bhattacharjee, D. Banerjee, Md. A. Asgar, R. Banik, S. Bhattacharyya, Soumik Bhattacharya, A. Dhal, D. Mondal, G. Mukherjee, S. Mukhopadhyay, S. Pal, D. Pandit, **T. Roy**, S. R. Banerjee.

Proceedings of the DAE-BRNS Symp. on Nucl. Phys., Vol **61** 316 (2016).

(g) **Search for fadeout of collectivity in nuclear level density**

K. Banerjee, Pratap Roy, C. Bhattacharya, T. K. Ghosh, A. Sen, S. Bhattacharya, S. Kundu, T. K. Rana, G. Mukherjee, R. Pandey, S. Manna, **T. Roy**, Md. A. Asgar, A. Dey, D. Pandit, S. Mukhopadhyay.

Proceedings of the DAE-BRNS Symp. on Nucl. Phys., Vol **61** 374 (2016).

(h) **Further evidence of the absence of the shell effects in fission fragment mass distribution in ^{210}Po**

A. Sen, T. K. Ghosh, K. Banerjee, C. Bhattacharya, S. Bhattacharya, S. Kundu, G. Mukherjee, Md. A. Asgar, P. Bhattacharya, A. Dey, A. Dhal, M. Khan, J. K. Meena, R. Mondal Saha, S. Manna, R. Pandey, T. K. Rana, Pratap Roy, **T. Roy**, J. K. Sahoo, A. K. Saha, V. Srivastava.

Proceedings of the DAE-BRNS Symp. on Nucl. Phys., Vol **61** 378 (2016).

(i) **Study of higher excited states of ^{26}Al**

V. Srivastava, C. Bhattacharya, T. K. Rana, S. Manna, S. Kundu, S. Bhattacharya, K. Banerjee, P. Roy, R. Pandey, G. Mukherjee, T. K. Ghosh, J. K. Meena, **T. Roy**, A. Chaudhuri, M. Sinha, A. K. Saha, Md. A. Asgar, A. Dey, Subinit Roy, Md. Moin Shaikh.

Proceedings of the DAE-BRNS Symp. on Nucl. Phys., Vol **61** 514 (2016).

(j) **Role of clustering in decay of ^{24,25}Mg**

S. Manna, T. K. Rana, C. Bhattacharya, S. Bhattacharya, S. Kundu, K. Banerjee, Pratap Roy, R. Pandey, V. Srivastava, A. Chaudhuri, **T. Roy**, T. K. Ghosh, G. Mukherjee, J. K. Meena, S. K. Pandit, K. Mahata, A. Srivastava, V. Nanal.

Proceedings of the DAE-BRNS Symp. on Nucl. Phys., Vol **61** 542 (2016).

(k) **Geant4 Simulation of VECC array for Nuclear Spectroscopy VENUS**

Md. A. Asgar, G. Mukherjee, **T. Roy**, Soumik Bhattacharya, A. Dhal.

Proceedings of the DAE-BRNS Symp. on Nucl. Phys., Vol **61** 950 (2016).

(l) **Excited states of ^{26}Al studied via the reaction ^{27}Al(d,t)**

Vishal Srivastava, C. Bhattacharya, T. K. Rana, S. Manna, S. Kundu, S. Bhattacharya, K. Banerjee, P. Roy, R. Pandey, G. Mukherjee, T. K. Ghosh, J. K. Meena, **T. Roy**, A. Chaudhuri, M. Sinha, A. K. Saha, Md. A. Asgar, A. Dey, Subinit Roy and Md. Moin Shaikh.

EPJ Web of Conferences **117**, 07 022 (2016).

(m) **Nuclear structure study at low spin in ^{169}Tm.**

Md. A. Asgar, A. Dhal, **T. Roy**, G. Mukherjee, Soumik Bhattacharya, S. Bhattacharyya, C. Bhattacharya, S. Bhattacharya, A. Chaudhuri, K. Banerjee, S. Kundu, S. Manna, R. Pandey, and J.K. Meena.

Proceedings of the DAE-BRNS Symp. on Nucl. Phys., Vol **60** 80 (2015).

(n) **High spin gamma ray spectroscopy of ^{196}Tl.**

Md. A. Asgar, **T. Roy**, G. Mukherjee, H. Pai, S. Bhattacharyya, M.R Gohil, C. Bhattacharya, R. Palit, S. Saha, J. Sethi, T. Trivedi, Shital, Thakur, B.S Naidu, S.V Jadav, R. Donthi and A. Goswami.

Proceedings of the DAE-BRNS Symp. on Nucl. Phys. Vol **60** 172 (2015).

(o) **Geant4 simulation of a large volume segmented clover detector**

Md. A. Asgar, **T. Roy**, G. Mukherjee, and C. Bhattacharya.

Proceedings of the DAE-BRNS Symp. on Nucl. Phys. Vol **60** 960 (2015).

(p) **Study of one proton pick-up reaction ^{27}Al(d,^{3}He)**

Vishal Srivastava, C. Bhattacharya, T.K. Rana1, S. Manna, S. Kundu, S. Bhattacharya, K. Banerjee, P. Roy, R. Pandey, G. Mukherjee, T.K. Ghosh, J.K. Meena, **T. Roy**, A. Chaudhuri, M. Sinha, A. K.Saha, Md. A. Asgar, A. Dey, Subinit Roy and Md. Moin Shaikh.

Proceedings of the DAE-BRNS Symp. on Nucl. Phys. Vol **60** 342 (2015).

(q) **Effect of neutron shell closure in fission fragment mass distributions of ^{206,210}Po**

A. Chaudhuri, T. K. Ghosh, K. Banerjee, S. Bhattacharya, Jhilam Sadhukhan, S. Kundu, C. Bhattacharya, J. K. Meena, G. Mukherjee, A. K. Saha, **Md. A. Asgar**, A. Dey, S. Manna, R. Pandey, T. K. Rana, P. Roy, **T. Roy**, V. Srivastava, P. Bhattacharya, D. C. Biswas, B. N. Joshi, K. Mahata, A. Shrivastava, R. P. Vind, S. Pal, B. R. Behera, and Varinderjit Singh.

Proceedings of the DAE-BRNS Symp. on Nucl. Phys. Vol **60** 360 (2015).

(r) **Study of fusion-fission dynamics of ^{200}Pb through fission fragment mass distribution**

A. Chaudhuri, T. K. Ghosh, K. Banerjee, S. Bhattacharya, P. Roy, **T. Roy**, C. Bhattacharya, S. Kundu, J. K. Meena, G. Mukherjee, Md. A. Asgar, A. Dey, S. Manna, R. Pandey, T.K. Rana, A. Sen, M. Sinha, V. Srivastava, P. Bhattacharya, R. Dubey, N. Saneesh, P. Sugathan, and Gurpreet Kaur.

Proceedings of the DAE-BRNS Symp. on Nucl. Phys. Vol **60** 506 (2015).

(s) **Role of fusion fission process on fragment emission mechanism in ^{32}S+^{12}C reaction**

R. Pandey, C. Bhattacharya , S. Kundu1, K. Banerjee1, S. Manna, T. K. Rana1, J.K. Meena, **T. Roy**, A. Chaudhuri, Md. A. Asgar, V.Srivastava, A.Dey, M.Sinha, G. Mukherjee, P.Roy, T.K.Ghosh, S.Bhattacharya,A. Srivastava, K.Mahata, S.K.Pandit, P.Patle, S.Pal, V. Nanal.

Proceedings of the DAE-BRNS Symp. on Nucl. Phys. Vol **60** 544 (2015).

(t) **Evolution of collectivity in ^{160}Yb**

A. Saha, T. Bhattacharjee, S. Rajbanshi, A. Bisoi, D. Curien, J. Dudek, P. Petkov, D. Banerjee, S.R. Banerjee, Soumik Bhattacharya, S. Bhattacharyya, S. Biswas, A. Chakraborty, G.de Angelis, S.K. Das, S. Das Gupta, B. Dey, G. Duchene, A. Goswami, D. Mondal, D. Pandit, R. Palit, **T. Roy**, M. Saha Sarkar, S. Saha, R.P. Singh, J. Sethi.

Proceedings of the DAE-BRNS Symp. on Nucl. Phys. Vol **59** 268 (2014).

(u) **Mass distribution in ^{238}U(^{32}S,f) reaction**

L.S. Danu, B. K. Nayak, D. C. Biswas, B. V. John, A. Saxena, E. T. Mirgule, S. Mukhopadhyay, Y. K. Gupta, B. N. Joshi, G. Prajapati, V. V. Desai, S. V. Suryanarayana, A. Goswami, P. K. Joshi, S. K. Tandel, R. Palit, S. Saha, J. Sethi, S. Biswas, D. Choudhury, P Singh, R. G. Pillay, V. Nanal, **T. Roy**, Md Ali Asgar, P. V. Madhusudhana Rao, Naveen Kumar, U. Garg.

Proceedings of the DAE-BRNS Symp. on Nucl. Phys. Vol **59** 368 (2014).

(v) **Fragment emission mechanism in ^{12,13}C + ^{12}C reactions**

S. Manna, C. Bhattacharya, T.K. Rana, V. Srivastava, K. Banerjee, S. Kundu, P. Roy, R. Pandey, A. Chaudhury, **T. Roy**, T.K. Ghosh, G. Mukherjee, S. Bhattacharya, J.K. Meena, S.K. Pandit, K. Mahata, P. Patale, A. Shrivastava,

V. Nanal, S. Pal.

Proceedings of the DAE-BRNS Symp. on Nucl. Phys. Vol **59** 560 (2014).

(w) **Target Coulex and the Production of Po Isotopes by Fusion Evaporation Reaction**

Md. A. Asgar, **T. Roy**, G. Mukherjee, Soumik Bhattacharya, S.Bhattacharyya, C. Bhattacharya, S. Bhattacharya, A. Chaudhuri, K. Banerjee, S. Kundu, S. Manna, R. Pandey, and J.K. Meena R. Palit, S. Biswas, S. Saha, J. Sethi, P. Singh, and D. Choudhury.

Proceedings of the DAE Symp. on Nucl. Phys. Vol. **59** 246 (2014).

(x) **Characterization of a segmented clover detector**

Md. A. Asgar, **T. Roy**, G. Mukherjee, Soumik Bhattacharya, Abhirup Chaudhuri, V. Srivastava, S. Bhattacharyya, S. Bhattacharya, C. Bhattacharya, T.K. Ghosh, K. Banerjee, S. Kundu, R. Pandey, T.K. Rana, P. Roy, S. Manna, J.K. Sahoo, J.K. Meena, A.K. Saha, R. Mondal Saha, P. Mukhopadhyay, A. Choudhury, and I. Shaik.

Proceedings of the DAE Symp. on Nucl. Phys. Vol. **59** 882 (2014).

(y) **Clover detector setup at VECC**

Soumik Bhattacharya, B. Dey, A. Saha, A. Choudhury, S. Bhattacharyya, T. Bhattacharjee, S.R. Banerjee, S. Das Gupta, D. Mondal, G. Mukherjee, S. Mukhopadhyay, P. Mukhopadhyay, D. Pandit, S. Pal, **T. Roy**, I. Seikh.

Proceedings of the DAE-BRNS Symp. on Nucl. Phys. Vol **58** 904 (2013).

Contents

List of Figures

List of Tables

Chapter 1

Introduction

At the end of the 19^{th} century Henry Becquerel discovered radioactivity in uranium salt using photographic plate, this led to a new branch of physics. Later on Marie Curie and her husband Pierre Curie developed the theory of radioactivity and discovered two new elements polonium (Z=84) and radium (Z=88). In order to explain atomic spectra Ernest Rutherford in 1911 put forward the concept of nucleus which is positively charged and contains the entire mass of the atom, started the field of nuclear physics. Later on discovery of neutron and use of modern accelerator based research using various type of detector systems kept on enriching our knowledge about the atomic nucleus. In the last 100 years the parallel development of experimental techniques along with theoretical advancement not only improved our knowledge about this subject but also invention of various technologies became part of our day to day life.

Atomic nucleus is a many body complex system. Various nuclear structure model has been developed over the years to successfully interpret various excited states of a nucleus. The liquid drop model was successful in interpreting the binding energy per nucleons, saturation of nuclear force etc. [1, 2]. Later on the same model was used by to explain newly discovered phenomenon like nuclear fission [3–5]. But this model was inadequate to interpret the stability of magic (proton and neutron) number nuclei 2, 8, 20, 28, 50, 82 and 126. Later on spherical shell model was introduced with the nucleons under harmonic oscillator potential along with strong spin orbit interaction term to interpret these magic numbers by Haxel, Jensen, Suess [6] and Maria Goeppert-Mayer [7] independently. These model also interprets excited states in nuclei, particularly single particle excitation in magic nuclei or near shell closure (e.g., ^{209}Bi(Z=83, N=126)). The odd proton occupies $h_{9/2}$ state which makes the ground state spin and parity of ^{209}Bi is $J^{\pi}=9/2^{-}$ as seen in Figure. (1.1). The excited odd proton occupies spherical single particle states $f_{7/2}$, $i_{13/2}$, $f_{5/2}$, and $p_{3/2}$ which is analogous to the observance of $J^{\pi}= 7/2^{-}$, $13/2^{+}$, $5/2^{-}$ and $3/2^{-}$ states by Lipoglavsek et al., [8].

However, far from closed shells i.e., for mass numbers A$\simeq$25, 150<A<190 (rare earth nuclei) and A>220 (actinides) the spherical single particle model with an inert core could not explain the large quadrupole moment and enhanced quadrupole transition probability (BE2) values with pronounced rotational bands of I(I+1) characteristic (where I is the angular momentum of the states), led to the development of deformed shell model [9–11]. In 1955 Nilsson [14] incorporated strong spin orbit term and flatness determining term to the axially deformed harmonic oscillator potential [13] at the nuclear surface to generate a realistic average potential.

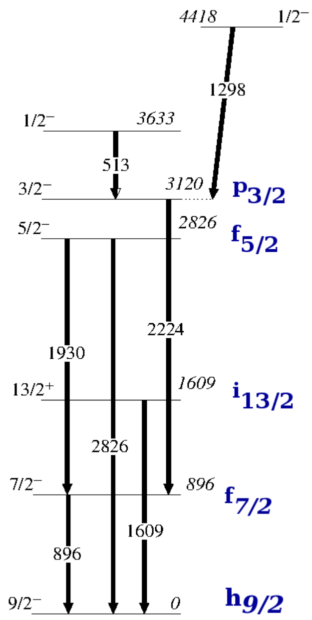

Figure 1.1: The level scheme of ^{209}Bi [8].

Later on various nuclear model had been proposed e.g., triaxial particle core model [5, 8, 14], cranking model etc. [18, 20, 21, 46] which were quite successful in interpreting the ground state rotational band along with the similar bands based on β- and γ- vibration states in nuclei in different mass region [12, 21, 22, 24].

Apart from this single particle and collecting nuclear phenomenon there has been various isomeric states and other exotic modes of nuclear excitation like magnetic rotation, chiral rotation etc. observed in various nuclei around proton magic number Z=82 [25, 35].

Nuclear isomers are metastable states with half-life $T_{1/2} \geq 10$ ns. There are various reason depending on detailed nuclear shell structure leads to such long lived nuclear states. Some of these reasons are discussed below with the pictorial representation in Figure. (1.2).

Shape isomers: The secondary energy minimum at large deformation lies much above the primary energy minimum of the ground state give rise to this type of isomers. This isomer can de-excite to the ground state via γ- ray emission or undergo fission to two lighter nuclei. The longest half-life of 14 ms fission isomer has been reported in ^{242}Am at an excitation energy of 2.2 MeV with major to minor axis ratio 2:1 [27].

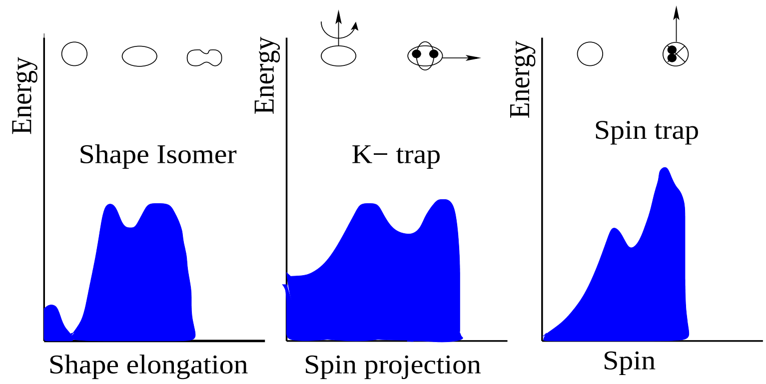

Figure 1.2: The excitation energy as a function of various nuclear variables. The secondary energy minimum is responsible for different kinds of isomer **(a)** Shape isomers, **(b)** K-traps, **(c)** Spin traps. In each case, various nuclear shape with respective angular momentum (as arrows) shown above.

K- isomers: Usually axially symmetric deformed nucleus with large difference in K quantum number (projection of angular momentum on the nuclear symmetry axis) de-excites from excited state to the ground state via electromagnetic transition of multipolarity (λ) following the selection rule $\lambda \geq \triangle$ K. However violation of the above stated selection rule leads to K trap isomers. In ^{180}Hf there is an I=8, K=8 isomer at 1.1 MeV with half-life of 5.5 hours [28]. It decays via 58 keV, λ=1 transition to an I=8, K=0 state violating $\lambda \geq \triangle$ K selection rule.

Spin trap isomers: This is the common form of isomer, whose existence depends on the difficulty in spin selection rules in accordance with the conservation of angular momentum. The decay to the lower energy states requires large change in nuclear spin with high multipolarity(λ) γ- ray emission or internal conversion. Some of the well known spin isomers in various odd Bi isotopes in mass region A$\sim$187-201 have been tabulated below in Table. 1.1.

Table 1.1: Some of the isomers observed in Bi isotopes near A$\sim$190 region are tabulated below with their respective excitation energy, spin-parity and configurations.

Nucleus	E_{Level} keV	States J^{π}	Half-life $T_{1/2}$	Configuration	References
^{187}Bi	252	$13/2^+$	$3.2^{+7.6}_{-2.0}$	$\pi i_{13/2}$	A. Hürstel et al., [29]
^{189}Bi	357	$13/2^+$	880(50)ms	$\pi i_{13/2}$	A. Hürstel et al., [29]
^{191}Bi	430	$13/2^+$	562(10)ns	$\pi i_{13/2}$	P. Nieminen et al., [30]
			400(40)ns		
^{193}Bi	0	$9/2^-$	67(3)s	$\pi h_{9/2}$	A. Herzáň et al., [31]
	605	$13/2^+$	153(10)ns	$\pi i_{13/2}$	
	2350	$29/2^+$	85(3)μs	$\pi h_{9/2} \otimes \nu_{11^-}$	
	2405	$(29/2^-)$	3.02(8)μs	$\pi h_{9/2} \otimes \nu_{12^+}$	
^{195}Bi	887	$13/2^+$	32(2)ns	$\pi i_{13/2}$	H. Pai et al., [32]
	2195	$23/2^+$	80(10)ns	$\pi h_{9/2} \otimes \nu_{7^-}$	
	(2396)	$29/2^{(-)}$	750(50)ns	$\pi h_{9/2} \otimes \nu_{12^+}$	
^{197}Bi	1601	$17/2^+$	16.2(17)ns	$\pi h_{9/2} \otimes \nu_{5^-}$	T. Chapuran et. al., [33]
	2360+$\triangle$	$(29/2^-)$	263(13)	$\pi h_{9/2} \otimes \nu_{9^-}$	
	2929	$(31/2^-)$	209(30)	$\pi h_{9/2} \otimes \nu_{9^-}$	
	1966.7+ $\triangle$	$(25/2^+)$	18ns		G.K. Mabala et al., [34]

Table 5.1: Continued...

Nucleus	E_{Level} keV	States J^{π}	Half-life $T_{1/2}$	Configuration	References
	2065	$25/2^+$	37ns		
^{197}Bi	2087.9	$(25/2^+)$	19ns		G.K. Mabala et al., [34]
	2357.4		53ns		
^{199}Bi	1647.5	$17/2^+$	34.1(24)	$\pi h_{9/2} \otimes \nu_{5^-}$	W.F. Piel et al., [35]
	1922.3	$21/2^+$	< 50	$\pi h_{9/2} \otimes \nu_{7^-}$	
	1922+ $\triangle$	$25/2^+$	101(31)	$\pi h_{9/2} \otimes \nu_{9^-}$	
	2523+ $\triangle$	$29/2^-$	168(13)	$\pi h_{9/2} \otimes \nu_{12^+}$	
^{201}Bi	1746.4	$17/2^+$	5.1(13)	$\pi h_{9/2} \otimes \nu_{5^-}$	W.F. Piel et al., [35]
	1932.2	$21/2^+$	< 40	$\pi h_{9/2} \otimes \nu_{7^-}$	
	1932+$\triangle$	$25/2^+$	118(28)	$\pi h_{9/2} \otimes \nu_{9^-}$	
	1971+$\triangle$	$27/2^+$	105(75)	$\pi h_{9/2} \otimes \nu_{9^-}$	
	2740+ $\triangle$	$29/2^-$	124(4)	$\pi h_{9/2} \otimes \nu_{12^+}$	

Apart from these high spin isomers, magnetic rotational bands reported in both ^{194}Tl and ^{197}Bi [34, 36] along with several Pb isotopes in mass A$\sim$190 region [37].

Magnetic Rotation: In early 1990s, rotation like patterns of gamma- rays (mostly M1 in nature) were discovered in near spherical nuclei $^{197,199,200}Pb$ [38, 39]. This regular band like structure appears for I>10, kinetic moment of inertia $J^{(2)} \sim 20$ MeV^{-1}, decreasing B(M1) values with increasing spin. This type of rotational band structure was interpreted as coupling of high-j particle and holes at the band head. Step-by-step alignment of the particle and hole spins into the direction of the total angular momentum resembling the closing of the blades of a pair of shears [40] give rise to angular momentum in a MR band. Recently, doubly degenerate bands are reported in odd-odd ^{194,198}Tl isotopes possessing chiral geometry [41,42].

Chiral Rotation: The chirality in nucleus was first predicted by Frauendorf and Meng [43]. The experimental signature of chiral partner bands are

i> The existence of near degenerate doublet bands of same spin and parity.

ii> Both bands should show a smooth variation i.e., there should be no or less staggering of S(I) (=(E(I)-E(I-1))/2I) as a function of spin(I).

iii> Both bands should have very similar physical properties like quasi-particle alignments (i_x), moment of inertia ($J^{(1)}$) and electromagnetic properties with similar characteristic staggering of the inband B(M1)/B(E2) ratio as a function of spin(I).

iv> The B(M1) and B(E2) transition strengths as a function of spin should be very similar for the chiral partner bands in the nucleus.

These effect is expected to occur in triaxially deformed nuclei at moderately high spin, where proton particle angular momentum $\mathbf{j}_\pi$ is along the short (s) axis, high-j neutron hole angular momentum $\mathbf{j}_\nu$ along the long (l) axis and collective (core rotational) angular momentum $\mathbf{R}$ along the intermediate axis (i). Depending on the rotation of the core (i.e., Right handed system or Left handed system) two identical chiral partner bands have been also reported in mass A $\sim$ 100 [44,45] and A $\sim$ 130 [46,47] region.

For the nuclei in mass A = 190 region with proton number near Z = 82, the intruder $\pi h_{9/2}$ (9/2[505], 1/2[541]) and $\pi i_{13/2}$ (13/2$^+$[606], 1/2$^+$ [660]) orbitals come down in energy for both oblate and prolate nuclear deformations. Whereas, in the neutron sector, the $i_{13/2}$ (1/2$^+$[660], 13/2$^+$[606]) orbitals compete with $p_{3/2}$ (3/2[512], 1/2[521]) and $f_{5/2}$ (5/2[503], 1/2[510]) for neutron occupation.

In the present thesis work, the motivation was the experimental investigation of the effect and relative importance of these high-j proton and neutron orbitals on the high spin states in the nuclei with proton number near the heaviest proton magic number Z=82. For this study, two systems were chosen, proton Fermi level lies just above the Z = 82 shell closure and ^{195}Bi in which ^{195}Tl in which the proton Fermi level lies just below it. The high-spin states in these nuclei were studied by populating them via heavy-ion fusion evaporation reaction and the de-excited gamma rays were detected by high-resolution clover HPGe detectors.

For Bismuth nuclei with Z = 83, the proton Fermi level lies just above the Z = 82 shell closure and near the high-j $h_{9/2}$ orbital. Because of the proximity of the spherical shell closures at Z = 82 and N = 126, the heavier Bi isotopes with neutron number N≥114 are spherical and the high spin states are mostly generated by single particle excitation [34, 35]. However, rotational bands, indicating deformed shape, have been observed in ^{191,193}Bi isotopes with neutron number N≤112 [30,31]. This is apparently due to the involvement of the high-j $i_{13/2}$ neutron orbital which becomes available for neutron number N<114. In the transitional nucleus ^{195}Bi a rotational band based on 13/2$^+$ state (πi$_{13/2}$ configuration) has been observed indicating the onset of deformation at N=112 for Bi isotopes. However, the information on the high spin states in this nucleus is very limited as only 9 (with one tentative state) excited states were known prior to the present work [32]. This also include a long-lived isomeric state having spin parity of $29/2^{(-)}$ with half-life of 750 ns at an excitation energy of about 2.4 MeV. A few transitions bypassing this isomeric state were also known but the high spin states were known only up to less than 3 MeV. Therefore, the effect of high-j unpaired neutron orbitals are not known in this important transitional nucleus. In comparison to that, in the neighbouring lighter isotope ^{195}Bi, information on the high spin states are very rich with the observation of several band structures up to an excitation energy of more than 5.5 MeV and 45/2 $\hbar$ of angular momentum. Moreover, several long-lived isomeric states were also known in this nucleus with half-lives of 3 μs to 85 μs. Because of the presence of high-j orbitals, several isomeric states are known in the nuclei in this region. For example, $29/2^-$ state is a well-known isomeric state in $^{195-201}$Bi isotopes with configuration $\pi h_{9/2} \otimes \nu_{12}{}^+$. There is also $31/2^-$ known isomeric state in Bi isotope with configuration $\pi \mathrm{i}_{13/2} \otimes \nu_9{}^-$. There is also $31/2^-$ known isomeric state in Bi isotope with configuration $\pi \mathrm{i}_{13/2} \otimes \nu_9{}^-$.

There have been several attempts to produce the high spin states in ^{195}Bi nucleus with various heavy-ion fusion evaporation reactions using ^{16}O, ^{19}F and ^{20}Ne projectiles on various targets but the high spin states could not be populated beyond those limited number of states as mentioned above although the above projectiles could be able to populate angular momentum more than 40 $\hbar$. It was, therefore, conjectured that there may exists a high-spin longer lived isomer in ^{195}Bi which prevented the observation of the higher spin states.

In this thesis work, the experiment was designed to preferentially identify this possible high-spin isomer and its decay. The reaction ^{169}Tm(^{30}Si,4n)^{195}Bi at a beam energy of

146 MeV on the target was used to populate the high spin states in this nucleus. Since the interest was to detect isomer, the decay γ-rays were detected at the focal plane of a Recoil separator. The experiment was, therefore, performed at the Pelletron-Linac facility at Inter University Accelerator Centre (IUAC), New Delhi using the HYbrid Recoil mass Analyzer (HYRA). The residues were separated from the large background of fission fragments by HYRA and brought at the focal plane where they were implanted on Si-pad detectors after passing through a Multi Wire Proportional Counter (MWPC). The delayed γ-rays were detected using a clover HPGe detector. There was another clover HPGe detector placed near the target chamber.

In the case of Thallium (Tl) nuclei with Z = 81, rotational bands corresponding to oblate deformation has been reported in $^{191-201}$Tl isotopes [48–52] based on the proton in the 9/2[505] state originated from the $\pi h_{9/2}$ intruder orbital and decoupled bands based on the $\pi h_{9/2}$ intruder orbital with prolate deformation has been reported in the lighter isotopes of $^{187-189}$Tl [48, 53]. Also, the neutron pair alignments of the oblate bands based on the $\pi h_{9/2}$ configuration in $^{191-193}$Tl [48, 49] take place in $\nu i_{13/2}$ orbital. As neutron number increases to 114, in case of Tl, the $\nu i_{13/2}$ orbital closes up and nearby $p_{3/2}$ and $f_{5/2}$ orbitals open up for neutron occupation. Therefore, ^{195}Tl can be considered as a transitional nucleus in his respect. Moreover, as the high-j orbitals exist near the proton and neutrons Fermi levels for these nuclei and the proton particle angular momentum (j_π) and neutron hole angular momentum (j_ν) are mutually perpendicular, they satisfy the criteria for the emergence of exotic high-spin phenomena, like magnetic rotation and nuclear chirality for near spherical and triaxial deformed shapes. Some of these bands are reported for the odd-odd Tl isotopes in this mass region. However, the odd-A nuclei near N = 114 are not well studied. The previous investigation of the high spin states in ^{195}Tl was done by using the ^{197}Au(α, 6n)^{195}Tl fusion evaporation reaction and using only four Ge(Li) detectors [54]. Therefore, high-spin states could not be produced in that work and was therefore, limited to below band crossing region of the $\pi h_{9/2}$[505] band with no information on the neutron pair alignment or other exotic high-spin phenomena. Therefore, in order to investigate in detail about the high-spin states in ^{195}Tl, it has to be populated by heavy-ion induced reaction to generate higher spins and also using a more efficient gamma detector array to observe the weakly populated states.

The present thesis has been arranged in the following way: A brief introduction of the nuclear models relevant to the present thesis work is described in chapter 2. Experimental techniques and data analysis have been discussed in chapter 3. Study of High Spin isomer in Bi isotopes and interpretation of results in Chapter 4, Study of rotational bands in ^{195}Tl and the interpretation of the results have been discussed in chapter 5. followed by summary and future outlook at the end of the thesis in chapter 6.

Bibliography

[1] C.F. Von Weizsčker, Z. Phys. **96**, 431 (1936).

[2] H.A. Bethe and R.F. Bacher. Rev. Mod. Phys. **8**, 82 (1936).

[3] L. Meitner and O.R. Frisch. Nature **143**, 239 (1939).

[4] J. Frenkel Phys. Rev. **55**, 987 (1939).

[5] N. Bohr and J.A. Wheeler. Phys. Rev. **56**, 426 (1939).

[6] O. Haxel, J.H.D. Jensen and H.E. Suess, Phys. Rev. **75**, 1766 (1949).

[7] M. G. Mayer Phys. Rev. **75**, 1969 (1949).

[8] M. Lipoglavsek et al., Phys. Lett. **B 593**, 61 (2004).

[9] J. Rainwater Phys. Rev. **79**, 432 (1950).

[10] A. Bohr Phys. Rev. **81**, 134 (1951).

[11] J. Rainwater Rev. Mod. Phys. **48**, 385 (1976).

[12] S. G. Nilsson. Mat. Fys. Medd. Dan. Vid. Selsk. **29**, 16 (1955).

[13] A. Bohr and B.R. Mottelson. Nuclear Structure, Vol. II, Chapter 4, Benjamin New York, 1975.

[14] A.S. Davydov and G.F. Filipov, Nucl. Phys. **A 8**, 237 (1958).

[15] J. Meyer-ter-Vehn et al., Phys. Rev. Lett. **32**, 1383 (1974).

[16] H.L. Yadav et al., Phys. Rev. Lett. **39**, 1128 (1977).

[17] D. R. Inglis Phys. Rev **96**, 1059 (1954).

[18] R. Bengston and S. Frauendrof. Nucl. Phys. **A 327**, 139 (1979).

[19] T. Bengston and I. Ragnarsson. Nucl. Phys. **A 436**, 14 (1985).

[20] W. Nazarewicz et al., Nucl. Phys. **A 512**, 61 (1990).

[21] C.A. Fields et al., Nucl. Phys. **A 389**, 218 (1982).

[22] S. Andre et al., Nucl. Phys. **A 243**, 229 (1975).

[23] W. Reviol et al., Nucl. Phys. **A 548**, 331 (1992).

[24] D. Ward et al., Nucl. Phys. **A 600**, 88 (1996).

[25] P. Walker and G. Dracoulis. Nature **399**, 35 (1999).

[26] A.K. Jain et al., Nuclear Data Sheet **128**, 1 (2015).

[27] H.C. Britt et al., At. Data Nucl. Data Tables **12**, 407 (1973).

[28] G. Audi et al., Nucl. Phys. **A 624**, 1 (1997).

[29] A. Hürstel et al., Eur. Phys. J. **A 21**, 365 (2004).

[30] P. Nieminen et al., Phys. Rev. **C 69**, 064326 (2004).

[31] A. Herzáň et al., Phys. Rev. **C 92**, 044310 (2015).

[32] H. Pai et al., Phys. Rev. **C 85**, 064317 (2012).

[33] T. Chapuran et al., Phys. Rev. **C 33**, 130 (1986).

[34] G.K. Mabala et al., Eur. Phys. J. **A 25**, 49 (2005).

[35] W. F. Piel et al., Phys. Rev. **C 31**, 2087 (1985).

[36] H. Pai et al., Phys. Rev. **C 85**, 064313 (2012).

[37] H. Hübel, Prog. Part. Nucl. Phys.**54**, 1 (2005).

[38] A. Kuhnert et al., Phys. Rev. **C 46**, 133 (1992).

[39] G. Baldsiefen et al., Phys. Lett. **B 275**, 252 (1992).

[40] R.M. Clark and A.O. Macchiavelli. Annu. Rev. Nucl. Part. Sci. **50**, 1 (2000).

[41] P.L. Masiteng et al., Phys. Lett. **B 719**, 83 (2013).

[42] E.A. Lawrie et al., Phys. Rev. **C 78**, 021305(R) (2008).

[43] S. Frauendrof and J.Meng et al., Nucl. Phys. **A 617**, 131 (1997).

[44] C. Vaman et al., Phys. Rev. Lett. **92**, 032501 (2004).

[45] J. Sethi et al., Phys. Lett. **B 725**, 85 (2013).

[46] S. Mukhopadhyay et al., Phys. Rev. Lett. **99**, 172501 (2007).

[47] A.D. Ayangeakaa et al., Phys. Rev. Lett. **110**, 172504 (2013).

[48] W. Reviol et al., Physica Scripta **56**, 167 (1995).

[49] W. Reviol et al., Nucl. Phys **A 548**, 331 (1992).

[50] H. Pai et al., Phys. Rev. **C 88**, 064302 (2013).

[51] N. M ărginean et al., Eur. Phys. J. **A 46**, 329 (2010).

[52] S. Das Gupta et al., Phys. Rev. **C 88**, 044328 (2013).

[53] W. Reviol et al., Phys. Rev. **C 49**, R587 (2013).

[54] R. M. Lieder et al., Nucl. Phys **A 299**, 255 (1978).

Chapter 2

Nuclear Models

Atomic nucleus is a complex system consisting of several protons and neutrons. These protons and neutrons interact among themselves through short range strong interaction. But the exact form of the nuclear potential is still not known after decades of intense research. Therefore, various nuclear properties are interpreted with the help several nuclear models based on both phenomenological arguments as well as on experimental facts. In this chapter few of these well known models are briefly described.

2.0.1 Liquid Drop Model

The liquid drop model was the first model that could describe various nuclear properties like I$\rangle$ Binding energy per nucleon $\frac{B(N,Z)}{A}|_{A\rangle 12} \simeq$ - 8.5 MeV and nuclear mass II$\rangle$ Fissioning of a nucleus and III$\rangle$ Saturation of nuclear force.

The basic assumption behind this proposition was nucleus is an incompressible liquid drop and nucleons are only interacting with its nearest neighbours. One can reproduce the the behaviour of binding energy per nucleon by fitting the Bethe and Weizsäcker [1,2] semi-empirical mass formula with the experimental data.

$$B.E(N,Z) = a_v A + a_s A^{2/3} + a_c \frac{Z^2}{A^{1/3}} + a_I \frac{(N-Z)^2}{A} - \delta(A) \tag{2.1}$$

where a_v = -15.68; a_s=18.56; a_c=0.717; a_I=28.1 [MeV] [3] and A= Atomic Mass No, Z/N= Proton/Neutron number.

$$\begin{aligned} \delta(A) &= 34A^{-\frac{3}{4}} && \text{for even-even} \\ &=0 && \text{for even-odd} \\ &= -34A^{-\frac{3}{4}} && \text{for odd-odd} \end{aligned} \tag{2.2}$$

The first term in Eq. (2.1) usually called the volume term, as it is proportional to A ($\propto r^3$, r=nuclear radius). The second term is responsible for surface energy as it is proportional to $A^{2/3}$($\propto r^2$). The third term takes into account coulomb energy associated with the coulomb repulsion of proton pairs ($\propto Z^2$) which is inversely proportional to the nuclear radius (r). Whereas the fourth term corresponds to nuclear symmetry energy to take into account of neutron excess (N-Z) in a nucleus. The last term takes care of paring effect among the like nucleons. Although this model is quite successful in explaining above stated nuclear phenomena but fails to interpret stability of nuclei around proton and neutron magic numbers 2, 8, 20, 28, 50, 82, 126. Also it is quite unsuccessful in explaining the two proton and neutron separation energy for magic number nuclei along with their magnetic moment.

2.0.2 Shell Model

The shell model considers that the nucleons are moving inside the nucleus independent of each other under the influence of an average potential. This potential is build up by the interaction of the individual nucleons. The approximate form of the potential will be such that the nucleons at the centre will not feel any force. But they will feel stronger binding force from the surface (r=R_0) to the interior of the nucleus.

$$\frac{\partial V(r)}{\partial r}|_{r=0} = 0 \tag{2.3}$$

$$\frac{\partial V(r)}{\partial r}|_{r<0} > 0 \tag{2.4}$$

At the same time finite range of the nuclear force puts the constraint V(r)= 0 when r > R_0.

So the realistic potential which satisfies the above mentioned criteria is Woods-Saxon potential [4]

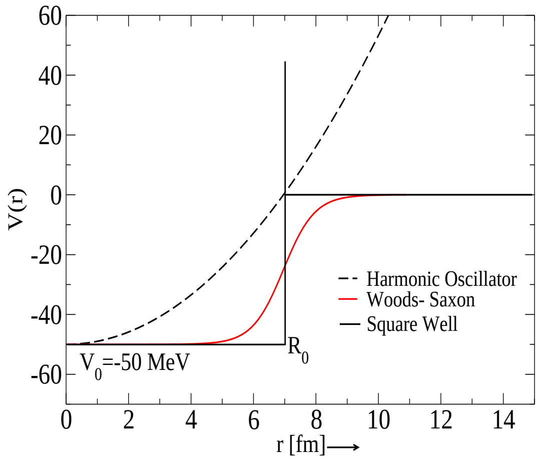

Figure 2.1: An illustration of three potential well used to model nuclear potential. Here V_0 is depth of the potential and R_0 is the radius of the nucleus.

$$V^{W.S}(r) = -\frac{V_0}{[1 + \frac{exp(r-R_0)}{a}]} \tag{2.5}$$

with $R_0=r_0A^{1/3}$; $V_0 \simeq 50$ [MeV]; $a \simeq 0.5$ [fm] $r_0 \simeq 1.2$ [fm]

Since the eigenfunction for this potential cannot be given in closed form, alternative I$\rangle$ Square well and II$\rangle$ Harmonic oscillator potentials are considered for qualitative understanding as well as for calculation.

$$\begin{aligned} V(r) = & -V_0 \qquad \text{for } r \leq R_0 \\ = & +\infty \qquad \text{for } r > R_0 \end{aligned} \tag{2.6}$$

$$V(r) = -V_0[1 - (\frac{r}{R_0})^2] \tag{2.7}$$

A schematic representation of the Square well, Harmonic oscillator and Woods-Saxon potentials have been shown in Figure. (2.1) with the nuclear potential depth of V_0=50 MeV and nuclear radius (r). The square potential has a flat bottom but sharp cut off at the boundary whereas the harmonic oscillator potential don't represent potential saturation at the centre of the nucleus without any specific nuclear boundary.

In case of harmonic oscillator potential one gets equidistant energy levels of energy

$$\epsilon_N = \hbar\omega_0(N + \frac{3}{2}) - V_0 \tag{2.8}$$

with N = 2(n-1) + l where n = 1, 2, ... and l = 0, 1, 2,.... where N is the number of quanta in the oscillator, n is the radial quantum number, l is the angular momentum quantum number and ω_0 is the oscillator frequency. But this potential can't reproduce magic numbers beyond 20, so latter Haxel, Jensen, Suess [5] and Maria Geopart Mayer [6] independently introduced a spin orbit coupling f(r) $\vec{\lambda}$. $\vec{s}$ term into the nuclear Hamiltonian.

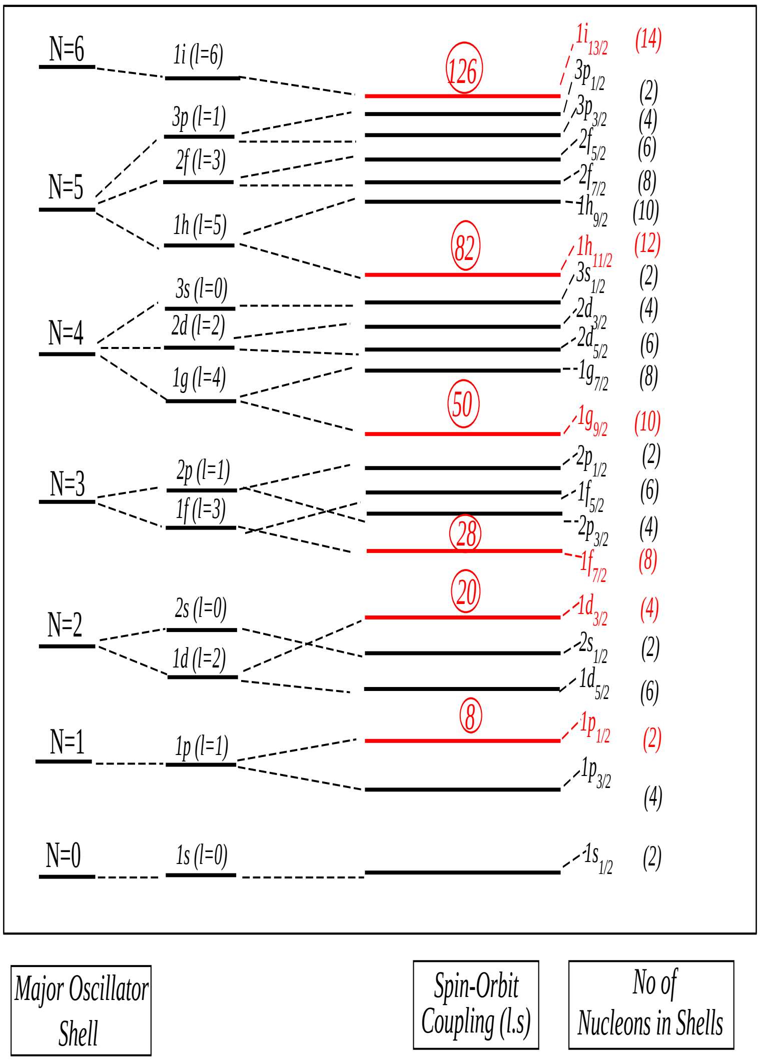

Figure 2.2: Schematic nuclear levels of the shell model with spin orbit term reproducing the nuclear magic numbers 8, 20, 28, 50, 82 and 126.

This gives the splitting to the degenerate levels with j= $l \pm \frac{1}{2}$ and energy difference between the splitted states by $\triangle$E(l) $\sim 2l{+}1$ which is shown in Figure. (2.2). An attractive spin orbit part of the nuclear potential always assures $l+\frac{1}{2}$ level is below the $l-\frac{1}{2}$ level, in comply with the experimental observation.

$$2\vec{l}.\vec{s} \mid sljm >= [j(j+1) - l(l+1) - \frac{3}{4}] \mid sljm > \tag{2.9}$$

2.0.3 Collective Model

Apart from the static liquid drop model, the nucleus may not necessarily be spherical, it can undergo dynamical shape and surface oscillations. In order to parametrize the radius vector pointing from the origin to the surface

$$R(\theta,\phi) = R_0(1+\alpha_{00} + \sum_{\lambda=1}^{\infty}\sum_{\mu=-\lambda}^{\infty} \alpha^*_{\lambda\mu} Y_{\lambda\mu}(\theta,\phi)) \tag{2.10}$$

where R_0 is the radius of the equivalent sphere with the same volume. The constant α_{00} describes the changes of the nuclear volume which can be expanded upto second order as [11]

$$\alpha_{00} = -\frac{1}{4\pi}\sum_{\lambda\geq 1,\mu} |\alpha_{\lambda\mu}|^2 \tag{2.11}$$

The deformations corresponding to $\lambda = 2$ look like ellipsoidal deformations with z-axis as the axis of symmetry. For quadrupole deformations there are five parameters $\alpha_{\lambda\mu}$, among them three parameters determine only orientation of the drop in space, corresponding to three Euler angles. By suitable rotation, the body-fixed system characterized by three axes 1, 2, 3 can be coincided with the principal axes of the mass distribution of the drop. The five coefficients $\alpha_{2\mu}$ reduces to two real independent variables a_{20} and a_{22}=a_{2-2} (a_{21}=

a_{2-1}=0) which together with the three Euler angles gives a complete description of the system. For convenience Hill - Wheeler [12] introduced coordinates β, γ ($\beta > 0$) through the relation

$$a_{20} = \beta_2 . \cos\gamma \tag{2.12}$$

$$a_{22} = \frac{1}{\sqrt{2}}\beta_2 . \sin\gamma \tag{2.13}$$

from which we have

$$\sum_{\mu} |\alpha_{2\mu}|^2 = a_{20}^2 + 2a_{22}^2 = \beta_2^2 \tag{2.14}$$

and

$$R(\theta,\phi) = R_0\{1 + \beta_2\sqrt{\frac{5}{16\pi}}(\cos\gamma(3\cos^2\theta - 1) + \sqrt{3}\sin\gamma\sin^2\theta\cos 2\phi)\} \tag{2.15}$$

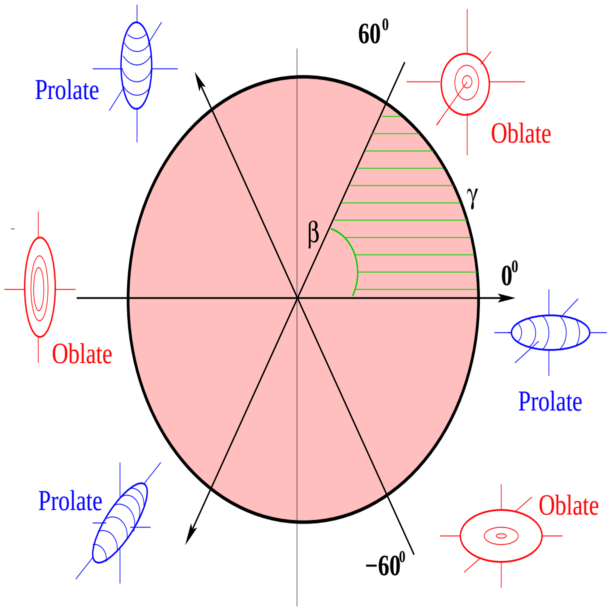

Figure 2.3: Schematic drawing of the nuclear shape with respect to the deformation parameters (β_2, γ) (Lund convention [8])

Figure. (2.3) illustrates the possible nuclear shapes in the (β_2, γ) half-plane between $\gamma = -120^0$ and 60^0. At $\gamma = -120^0$ and 60^0 nuclear shape is prolate whereas it is oblate at $\gamma = \pm 60^0$ and nuclear shape is triaxial when γ is not a multiple of 60^0.

The increments of the three semi-axis in the body-fixed frame as functions of β_2 and γ can be given in the following way

$$\delta R_k = R_0 \sqrt{\frac{5}{4\pi}} \beta_2 \cos(\gamma - \frac{2\pi}{3} k) \qquad \text{k=1,2,3} \tag{2.16}$$

In a deformed nucleus, the relation between axis lengths a, b and c as shown in Figure. (2.4) determines the nuclear shape. The deformed nucleus with $a \neq b \neq c$ corresponds to triaxial shape whereas $a = b \neq c$ represents axially- symmetric shape with a and b represents semi minor axis and c semi major axis length, respectively. A quadrupole shape with deformation [$\epsilon_2 = \frac{3(c/a-1)}{(1+2c/a)}$] $\epsilon_2 > 0$ correspond to prolate and $\epsilon_2 < 0$ to oblate shape.

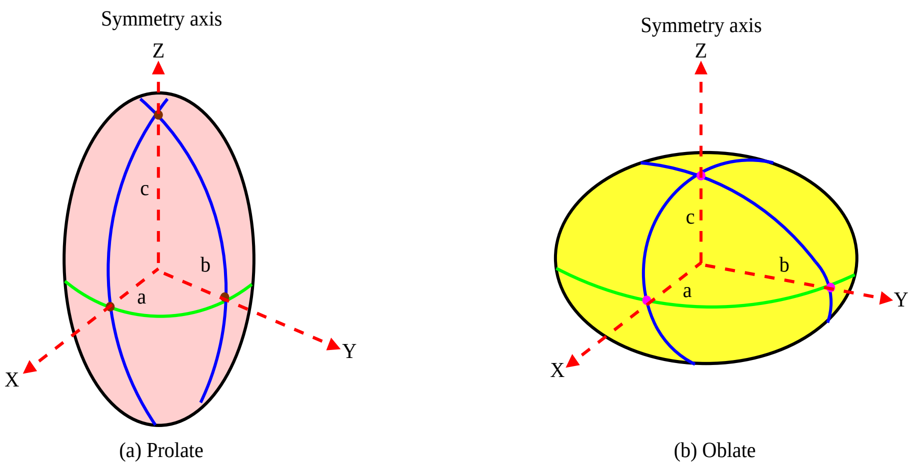

Figure 2.4: Schematic representation of prolate and oblate shapes with symmetry axis is along the z direction.

Typically, normal deformation is defined by an axis ratio ($c : a \simeq 1.2 : 1$) and superdeformation by ($c : a \simeq 2 : 1$).

2.0.4 Nilsson Model

In case of a deformed nucleus, the average nuclear potential can be approximated with anisotropic harmonic oscillator potential as

$$H = \frac{p^2}{2m} + \frac{1}{2}m[\omega_x^2 x^2 + \omega_y^2 y^2 + \omega_z^2 z^2] \tag{2.17}$$

with the three frequencies $\omega_x, \omega_y, \omega_z$ are proportional to the inverse of the half axes a_x, a_y, a_z of the ellipsoid.

$$\omega_\nu = \mathring{\omega}_0 \frac{R_0}{a_\nu} \qquad (\nu = x, y, z) \tag{2.18}$$

keeping the nuclear volume conserved the above stated frequencies satisfy the following relation

$$\omega_x \omega_y \omega_z = \mathring{\omega}_0{}^3 \tag{2.19}$$

The eigenstates of the above stated Hamiltonian are characterized by the quantum numbers n_x, n_y, n_z with eigenvalues as

$$E_0(n_x, n_y, n_z) = \hbar\omega_x(n_x + \frac{1}{2}) + \hbar\omega_y(n_y + \frac{1}{2}) + \hbar\omega_z(n_z + \frac{1}{2}) \tag{2.20}$$

In axially deformed nucleus, z axis is usually chosen as the axis of symmetry and the oscillator frequency is dependent on deformation ϵ_2 in the following way

$$\begin{aligned} \omega_\perp = \omega_x = \omega_y = \omega_0(\epsilon_2)(1 + \frac{1}{3}\epsilon_2) \\ \omega_z = \omega_0(\epsilon_2)(1 - \frac{2}{3}\epsilon_2) \end{aligned} \tag{2.21}$$

The distortion parameter ϵ_2 is obtained as $\epsilon_2 = \frac{\omega_\perp - \omega_z}{\omega_0}$. It is defined so that $\epsilon_2 > 0$ and $\epsilon_2 < 0$ correspond to the so called prolate and oblate shapes respectively. Using the criteria cited for ω_z and $\omega_\perp$, it can be shown that

$$\omega_0(\epsilon_2) = \mathring{\omega}_0(1 - \frac{1}{3}\epsilon_2^2 - \frac{2}{27}\epsilon_2^3)^{-\frac{1}{3}} = \mathring{\omega}_0(1 + \frac{1}{9}\epsilon_2^2 + ...) \tag{2.22}$$

Also this deformation parameter ϵ_2 is related the deformation parameter β_2 as

$$\epsilon_2 \approx \frac{3}{2}\sqrt{\frac{5}{4\pi}}\beta_2 \approx 0.95\beta_2 \tag{2.23}$$

It is convenient to use cylindrical coordinates to characterize the eigenstates in terms of quantum numbers n_z, n_ρ, m_l, where m_l is the projection of the orbital angular momentum on to the symmetry axis.

$$N = n_z + 2n_\rho + m_l = n_x + n_y + n_z = 2(n-1) + l \tag{2.24}$$

Here the eigenvalues in Eq.(2.20) can be expressed as

$$\begin{aligned} E_0(n_z, n_\rho, m_l) = &\hbar\omega_z(n_z + \frac{1}{2}) + \hbar\omega_\perp(2n_\rho + m_l + 1) \\ \simeq &\hbar\mathring{\omega}_0\{(N + \frac{3}{2}) + \epsilon_2(\frac{N}{3} - n_z)\} \end{aligned} \tag{2.25}$$

In axially symmetric nuclei m_l and s_z are good quantum numbers, which make the z-component j_z of the total angular momentum a good quantum number, in the following manner

$$\Omega = m_l + m_s = m_l \pm \frac{1}{2} \tag{2.26}$$

usually the eigenstates for an axially deformed nucleus is specified in terms of "Nilsson" quantum numbers (see Figure. (2.5)) along with parity (π) of the states as specified below

$$\Omega^\pi[N n_z m_l] \tag{2.27}$$

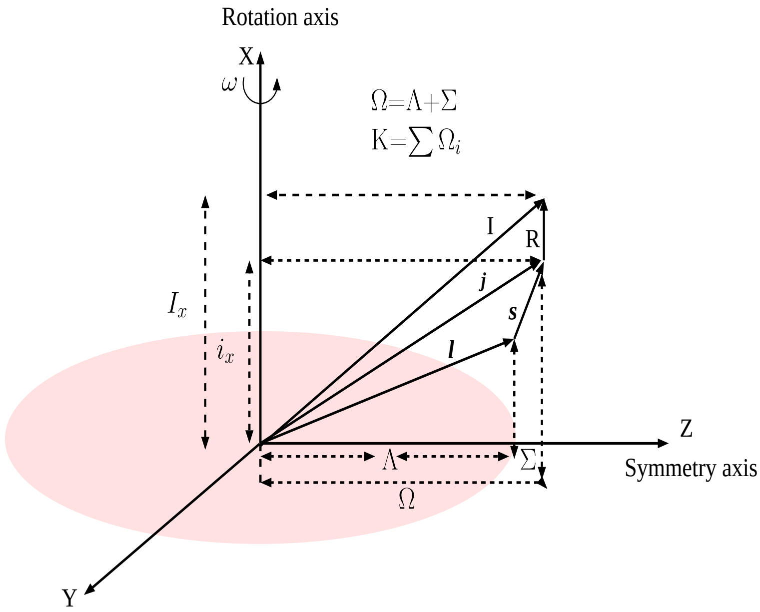

Figure 2.5: Asymptotic quantum numbers Λ, Σ and Ω for the Nilsson model are shown.

However in order to produce the magic numbers one has to incorporate a strong spin-orbit term in the Hamiltonian (H). At the same time a heavy nucleus feels a rather flat realistic average potential at the centre of the nucleus compared to the harmonic oscillator potential. Specially the nucleons at the surface (i. e., the nucleons with higher l values) feels a deeper average potential. To take into account of these two effects Nilsson [14] added two terms i. e., C $\overrightarrow{l}.\overrightarrow{s}$ and D l^2 into the deformed harmonic oscillator (2.17) along with nuclear deformation (ϵ_2) in the following manner

$$H = \frac{p^2}{2m} + \frac{1}{2}m[\omega_\perp^2(\epsilon_2)(x^2+y^2) + \omega_z^2 z^2] + C\overrightarrow{l}.\overrightarrow{s} + Dl^2 \tag{2.28}$$

where C gives the strength of the spin-orbit force and Dl^2 shifts the levels with higher l values downward as shown in Figure. (2.6). But in higher N quantum orbits the corresponding shift is too strong and later Dl^2 is replaced by D($l^2 - < l >^2_N$) [15] with $< l >^2_N = \frac{1}{2}N(N+3)$ is the expectation value of l^2 averaged over one major shell with quantum number N.

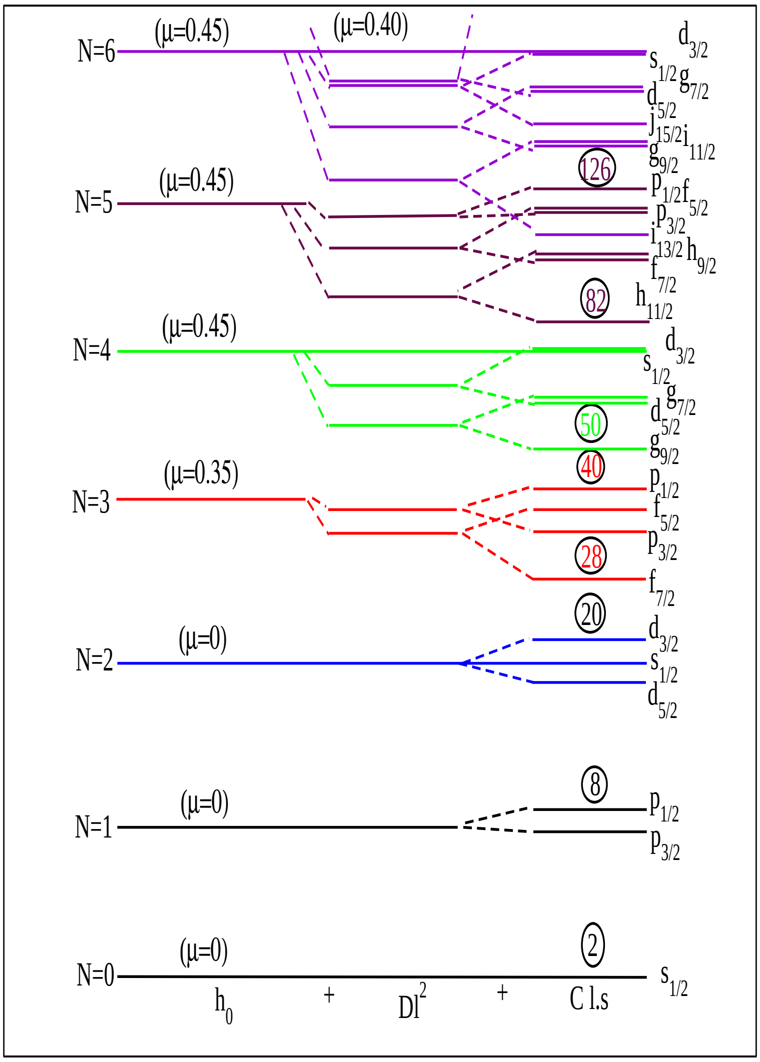

Figure 2.6: The energy levels of a spherical nucleus undergoes relative shift due to introduction of Dl^2 term in the asymmetric harmonic oscillator potential for deformed nucleus. The spin-orbit (C$l.s$) coupling term reproduces the magic number which lifts the l degeneracy of the different orbitals.

Nilsson introduced a deformation-dependent oscillator length b(ϵ_2)=$[\hbar/m\omega_0(\epsilon_2)]^{1/2}$ and dimensionless coordinates r$'$=R/b along with the previously mentioned two correction terms and the Hamiltonian in Eq.(2.28) transforms to

$$H = \hbar\omega_0(\epsilon_2)[-\frac{1}{2}\Delta' + \frac{1}{2}r'^2 - \beta_2 r'^2 Y_{20}] + Cl.s + D(l^2 - <l>_N^2) \tag{2.29}$$

$$C = -2\hbar\tilde{\omega}_0\kappa \qquad D = -\hbar\tilde{\omega}_0\kappa\mu \tag{2.30}$$

Whereas the effect of the Coulomb term in the Nilsson Hamiltonian is incorporated through an appropriate choice of the constants κ and μ [17].

So some of the characteristic features of the Nilsson diagram which are visible in Figure. (2.7) are as follows

1. The shells with single particle angular momentum j at zero deformation splits up into $(2j{+}1)/2$ levels for $\epsilon_2 \neq 0$. Each of these is twofold degenerate with eigenvalues $\pm\Omega$ and can be characterized by $|\Omega|$ and its parity.

2. The quadrupole field r'^2Y_{20} causes levels with lower Ω values to be shifted downwards for positive deformations (prolate shapes) and lifted upwards for negative deformations (oblate shapes). The lower Ω orbitals lie closer to the z-axis and positive quadrupole moment $\langle r'^2 Y_{20}\rangle$ for prolate shape reduces the energy eigen values of the Hamiltonian because of negative sign in Eq.(2.29). The nucleons feel a deeper deformed potential well for prolate deformation and vise versa for oblate deformation.

3. For larger deformation the shells having same quantum number Ω^π (different j values) can come very close to each other due to shape driving effect of the orbitals but they will never cross each other [16]. The repulsion $\triangle$E at the crossing point is proportional to the interaction strength and the properties of levels gets interchanged.

4. The slope of the Nilsson levels E_k are determined from the single-particle matrix element of the quadrupole operator $q=r'^2Y_{20}$ in the corresponding single-particle state $|k\rangle$

$$\frac{dE_k}{d\beta} = -\langle k|r'^2Y_{20}|k\rangle \tag{2.31}$$

5. The basis chosen for diagonalization of the Nilsson Hamiltonian is a superposition of spherical harmonic oscillator functions. The expansion coefficient is unity for a particular orbital (zero for rest of the orbitals) in case of smaller deformation ϵ_2. However if there are no neighbouring orbitals like in case of $1i_{13/2}$ and $2g_{9/2}$. then also there will not be much mixing and the corresponding levels are almost eigenstates of j^2.

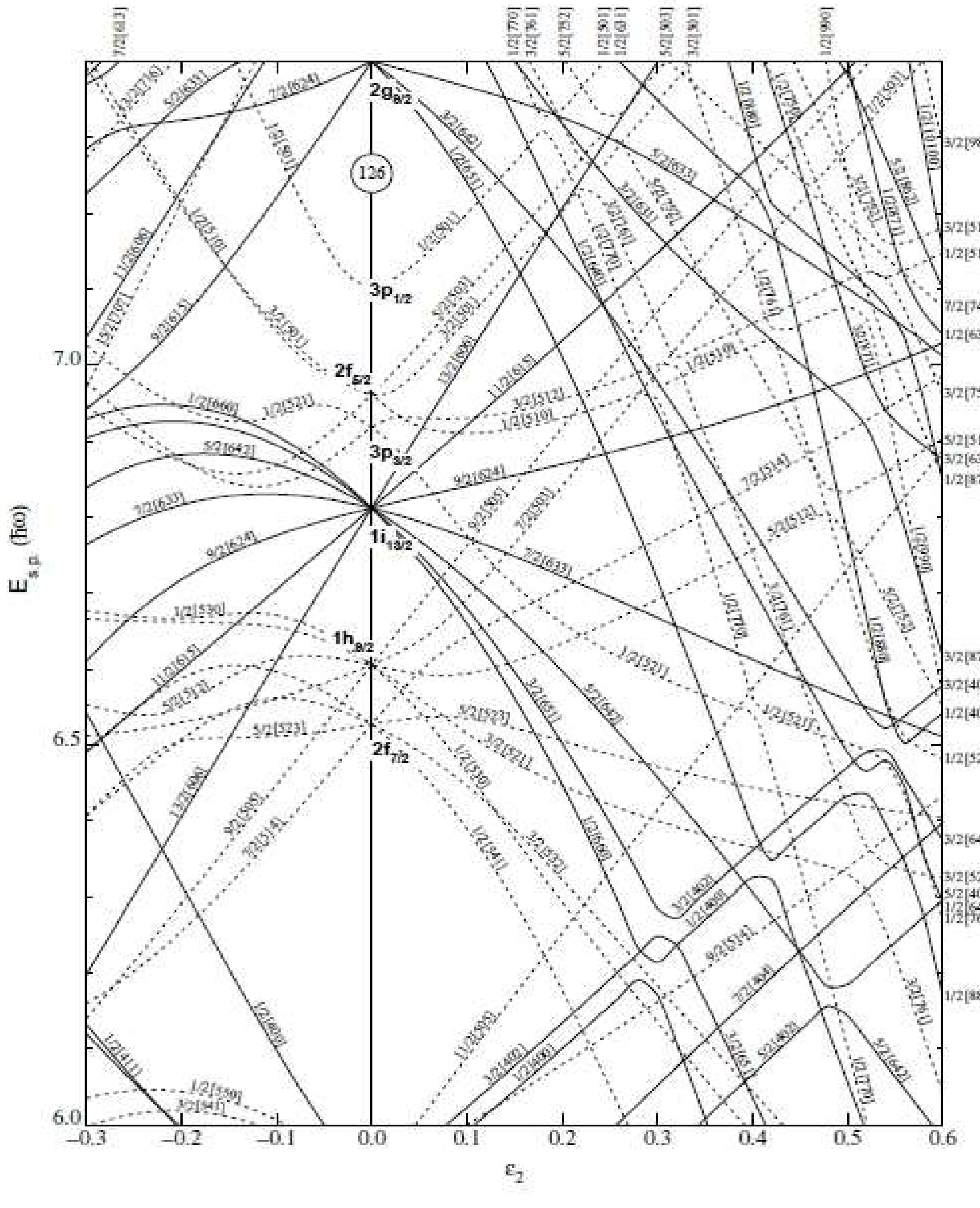

Figure 2.7: Nilsson diagram of single-neutron energies ($Z \sim 82$) as a function of the quadrupole deformation parameter ϵ_2. Solid and dashed lines correspond to positive and negative parity, respectively. Figure. taken from [7]

2.0.5 Strutinsky shell correcction

Liquid drop model successfully represents a dependence of nuclear binding energy whereas nuclear shell model considers the quantized nucleonic motion in an average potential to take care of the significance of magic number, nuclear spin etc. But this later phenomenological model fails to correctly reproduce total binding energy of nucleus, in order take of care of this Strutinski given a shell correction prescription [9, 10]. It is able to reproduce experimental ground state energies of a nucleus along with its dependence on nuclear deformation parameter. Here he considered nuclear binding energy E consisted of a smooth part E_{LDM} given by Bethe- Weizäcker mass formula (2.1) and an oscillatory part E_{OSC} defined by

$$E = E_{osc} + E_{LDM} \tag{2.32}$$

This oscillatory part of binding energy is quantum mechanical in nature due to grouping of levels into bunches- the shells. Near the magic nuclear numbers, the level density increases and if the Fermi level is situated just above a shell, nuclear binding energy increases whereas if it occupies just below a shell, binding energy becomes lesser than the average. So the binding energy corresponding to the shell distribution oscillate around an average level density. It is this average part of level density comes out wrong from the phenomenological shell model. So Strutinsky prescribed to calculate the oscillating part of E_{osc} of the total energy E in Eq.(2.32) within the shell model and rest of the energy E_{LDM} from the liquid drop model. So the shell energy is divided up into an oscillating part E_{osc}, and smoothly varying part $\widetilde{E}_{sh}$.

$$E_{sh} = \sum_{i=1}^{A} \epsilon_i = E_{osc} + \tilde{E} \tag{2.33}$$

In the shell model level density is defined as

$$g(\varepsilon) = \sum_{i=1} \delta(\epsilon - \epsilon_i) \tag{2.34}$$

and if we know the level density g(ϵ), particle number can be calculated as

$$A = \int_{-\infty}^{\lambda} g(\epsilon) d\epsilon \tag{2.35}$$

with properly chosen Fermi energy λ.

In the shell model, λ has not been defined uniquely by Eq.(2.35). It has been arbitrarily chosen to be between the last filled and the first unfilled level. For the shell model energy, we get

$$E_{sh} = \int_{-\infty}^{\lambda} \epsilon g(\epsilon) d\epsilon \tag{2.36}$$

The shell model levels are grouped into bunches with an average distance of $\hbar\omega_0 \backsimeq 41$ A$^{-1/3}$. Therefore, the level density g shows oscillations with roughly this frequency and the fluctuations in the shell model energy E$_{sh}$ are due to this oscillations can be separated by introducing a smooth part $\widetilde{E}_{sh}$ with a continuous function $\widetilde{g}(\epsilon)$, which represents the smooth part of the level density g(ϵ). With the help of this average part $\widetilde{g}(\epsilon)$ of the shell model level density g(ϵ) we can calculate the corresponding Fermi energy

$$A = \int_{-\infty}^{\tilde{\lambda}} \tilde{g}(\epsilon) d\epsilon \tag{2.37}$$

For the smooth part of the energy we finally get

$$\tilde{E_{sh}} = \int_{-\infty}^{\tilde{\lambda}} \epsilon \tilde{g}(\epsilon) d\epsilon \tag{2.38}$$

The total energy E of the system is given by

$$E = E_{osc} + E_{LDM} = E_{LDM} + E_{sh} - \tilde{E_{sh}} \tag{2.39}$$

Usually stable liquid drops are always spherical but due to the additional term E_{osc}, it can happen that in some region of periodic table the "Strutinsky averaged energy "given by Eq. (2.39) has its minimum at finite values of deformation.

2.0.6 Cranking Model

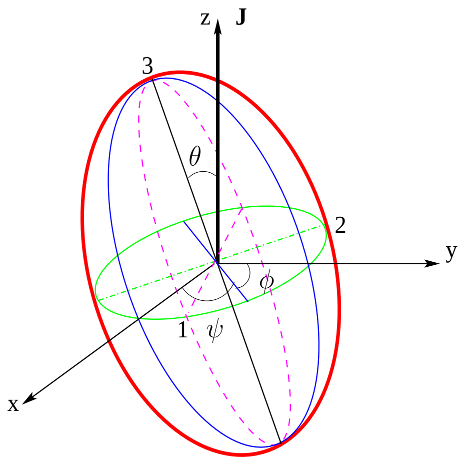

Figure 2.8: The orientation of the axis of rotation (**J**) with respect to the principal axes.

Nilsson model can describe levels for deformed nuclei, whereas rotational level structure was initially interpreted by Inglis [18,19] using semi classical cranking model. This model gives the microscopic description of the influence of rotation on single particle motion [20,21]. By introducing a suitable coordinate system which rotates with constant angular velocity ω around a fixed axis in space, the motion of the nucleons in the rotating frame becomes rather simple. Therefore, the nucleons can be considered as independent particles moving in an average potential well which is rotating with the coordinate frame as shown in Figure. (2.8). The outer shell nucleon angular momentum (j) generates rotation in the nucleus around x- axis ($\perp$ the symmetry axis z) with angular frequency ω.

Therefore, the single particle Hamiltonian in the cranking model can be given as

$$h_\lambda^\omega = h_\lambda^0 - \omega j_x \tag{2.40}$$

which ultimately gives the total many body cranking Hamiltonian of the nucleus as

$$H^\omega = H^0 - \omega J_x = \sum_{\lambda=1}^{A} h_\lambda^\omega \tag{2.41}$$

solving this Hamiltonian in terms of eigenfunction $|\lambda^\omega\rangle$ the total energy in the laboratory system can be obtained as

$$E = \sum_{\lambda=1}^{A} e_\lambda^\omega + \omega \sum_{\lambda=1}^{A} \langle\lambda^\omega|j_x|\lambda^\omega\rangle \tag{2.42}$$

This cranking model allows the calculation of various parameters like projection of total angular momentum (I_x) and aligned angular momentum (i_x) in the following manner

$$I_x = \sum_{\lambda=1}^{A} \langle \lambda^\omega | j_x | \lambda^\omega \rangle \tag{2.43}$$

$$i_x = -\frac{de_\lambda^\omega}{d\omega} \tag{2.44}$$

The coriolis term $-\omega j_x$ in the total Hamiltonian breaks the time reversal symmetry in the nucleus as a result of which Nilsson quantum number Ω is not a good quantum number any more. The signature quantum number α which describes the rotation of a symmetric rotor by 180^0 about the rotation axis along with the parity(π) act as a good quantum number to describe the individual nuclear state.

$$r = e^{-i\pi\alpha} \tag{2.45}$$

The eigen values of the signature operator are given in terms of of r and signature quantum number (α) and is related with the angular momentum (I) of a state by

$$I = \alpha \mod 2 \tag{2.46}$$

The explicit dependence of signature operator eigen value (r) with angular momentum (I) for integer spin given in Eq.(2.47) and half-integer spin values through Eqs.

$$\begin{aligned} r =& +1 \qquad \text{for I=}0, 2, 4, 6...... \\ =& -1 \qquad \text{for I=}1, 3, 5, 7...... \end{aligned} \tag{2.47}$$

$$\begin{aligned} r =& -i \qquad \text{for I=}1/2, 5/2, 9/2... \\ =& +i \qquad \text{for I=}3/2, 7/2, 11/2... \end{aligned} \tag{2.48}$$

Some of the single particle levels shows strong energy splitting with increasing ω, particularly in large j and small Ω values (e.g $1i_{13/2}$, $660\frac{1}{2}$, $651\frac{3}{2}$, $642\frac{5}{2}$). The signature of the favoured and unfavoured states is defined as

$$\alpha_f = \frac{1}{2}(-1)^{j-1/2} \qquad \alpha_u = \frac{1}{2}(-1)^{j+1/2} \tag{2.49}$$

where the angular momentum of the odd particle is expressed by j. In case of multi particle configuration the favoured signature is determined from the following Eq.

$$\alpha_f = \frac{1}{2}\sum_i (-1)^{j_i-1/2} \tag{2.50}$$

The cranking approach is successful in describing the rotation effect on single particle energy levels in deformed nucleus but can not describe the total nuclear energy.

2.0.7 Total Routhian Surface Calculation

In order to calculate the total nuclear energy the total Routhian Surface (TRS) calculation has been performed on ^{195}Bi and ^{195}Tl in this thesis work based on code developed by Nazarewicz et al. [45, 46]. In this model single particle energy levels were generated with deformed Woods- Saxon potential

$$V(r,\beta) = \frac{V_0}{1 + exp[dist_{\Sigma}(r,\beta/\mathrm{a}]} \tag{2.51}$$

where $dist_{\Sigma}(r,\beta)$ is the numerically generated distance of a point r from the nuclear surface Σ and β denotes the set of all shape parameters specifying Σ uniquely and diffuseness parameter a=0.7 fm. The total Routhian of a nucleus is calculated as a function of nuclear deformation (β, γ)

$$E^{\omega}(Z,N,\beta,\gamma) = E^{\omega}_{LD}(Z,N,\beta,\gamma) + E^{\omega}_{Shell}(Z,N,\beta,\gamma) + E^{\omega}_{Pair}(Z,N,\beta,\gamma) \tag{2.52}$$

The liquid drop model energy E^{ω}_{LD} is calculated with nuclear surface energy [E^{ω}_{Surf}], nuclear Coulomb energy [E^{ω}_{Coul}] and the nuclear rotational energy [E^{ω}_{rot}]

$$E^{\omega}_{LD}(Z,N,\beta,\gamma) = E^{\omega}_{Surf}(Z,N,\beta,\gamma) + E^{\omega}_{Coul}(Z,N,\beta,\gamma) + E^{\omega}_{rot}(Z,N,\beta,\gamma) \tag{2.53}$$

where nuclear rotational energy is calculated with rigid body moment of inertia (J_{rig}) at a given deformation of uniform density distribution at r_0=1.2 fm

$$E^{\omega}_{rot}(Z,N,\beta,\gamma) = \frac{\hbar^2 I(I+1)}{2J_{rig}} \tag{2.54}$$

The shell correction energy E^{ω}_{Shell} is calculated using Strutinsky shell correction [9, 10] approach whereas E^{ω}_{Pair} is calculated using monopole pairing in the cranking Hartee-Fock-Bogoliubov approach. The minimum in the contour plot of this energy gives the ground state deformation of the nucleus in terms of β_2 and γ. So each of this energy is minimized on β_4 in the $(\beta_2, \beta_4, \gamma)$ mesh to generate Routhian.

2.0.8 Chiral Symmetry Breaking

First time in 1997 S. Frauendorf and J. Meng [24] put forward the idea of rotation of two particle coupled to triaxial particle core in Tilted Axis Cranking (TAC) model. They showed that when the axis of rotation lies outside the principal planes of triaxial density distribution, pairs of identical $\triangle$I = 1 bands with the same parity are generated as a solution of the Hamiltonian. These two bands differ by the chirality of the principal axes with respect to the angular momentum vector as shown in Figure. (2.9). The selection rule for the electromagnetic transition probability in the chiral geometry has been proposed in Ref. [25]. Thereafter several candidates of chiral partner bands have been reported in odd-odd nuclei in mass A∼130 region with $\pi h_{11/2} \otimes \nu h_{11/2}$ configuration [25, 27–35], A∼100 with $\pi g_{9/2}^{-1} \otimes \nu h_{11/2}$ configuration [36–38] and A∼190 with $\pi h_{9/2} \otimes \nu i_{13/2}^{-1}$ configuration [3,39]. Similar bands based on 3-qp configuration have been reported in odd-A isotopes of ^{103,105}Rh with configuration $\pi g_{9/2} \otimes \nu h_{11/2}(g_{7/2}d_{5/2})$ [41–43] and in ^{135}Nd with configuration $\pi h_{11/2}^{2} \otimes \nu h_{11/2}^{-1}$ [44, 45]. There is also theoretical prediction of observing multiple chiral bands in a single nucleus [46,47] and recently similar bands has been reported in ^{133}Ce [48]. At the same time first chiral doublet bands claimed in ^{134}Pr [49] was cotradicted by the life time measurement done by the authors of Ref. [50]. Latter on C.M. Petrache et al., put forward more stringent criteria of chiral partner bands in the article [51].

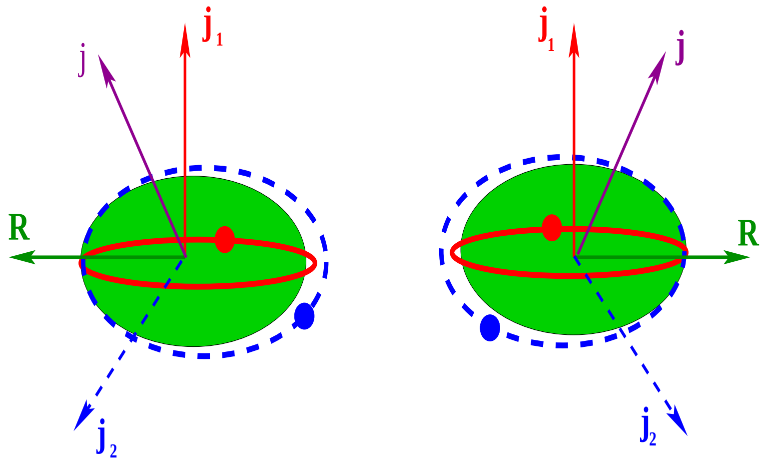

Figure 2.9: Schematic representation of orientation of the coupling of particle and hole angular momenta with that of a triaxial deformed core, forming left-handed or a right-handed coordinate system. Neutron hole angular momentum ($\mathbf{j}_1$) and proton particle angular momentum ($\mathbf{j}_2$) and core rotational angular momentum (**R**) perpendicular to each other. The relative orientation of **R** and total angular momentum (**j**) in this two systems depends on the handedness of the system, give rise to chiral geometry.

The experimental signature of these chiral partner bands are

i⟩ The existence of near degenerate doublet ($\triangle$I=1) bands of same spin and parity. They maintains constant excitation energy difference throughout the spin range, based on same configuration.

ii⟩ Both bands should show a smooth variation of S(I)(=(E(I)-E(I-1))/2I) i,e., there should be no or reduced staggering of S(I) as a function of spin(I). The staggering in the quantity S(I) represent Coriolis interactions between the particle or hole angular momenta with core rotational angular momenta. As these angular momenta are perpendicular to each other which reduces the Coriolis interaction considerably in case of chiral geometry, leads

S(I) to be independent of spin(I). Also the moment of inertia remains constant of spin throughout these bands.

iii$\rangle$ Both bands should have very similar physical properties like quasi-particle alignments (i_x), moment of inertia ($J^{(1)}$) and electromagnetic properties with similar characteristic staggering of inband B(M1)/B(E2) ratio as a function of spin(I).

iv$\rangle$ The B(M1) and B(E2) transition strengths should be similar for both of these bands which need to checked through life time measurement.

v$\rangle$ Inband and out of band $B(M1)_{in}/B(E2)_{out}$ ratio should maintain similar staggering pattern for transitions from levels in the partner band.

The chiral geometry is realized with triaxially deformed nucleus where neutron hole angular momentum ($\mathbf{j}_1$) along the short axis(s), proton particle angular momentum ($\mathbf{j}_2$) along the long axis(l) and core rotational angular momentum($\mathbf{R}$) along the intermediate axis(i). Initially the total angular momentum ($\mathbf{J}$) lies in the (l-s) plane but it comes out of the plane as nucleus starts rotating. The relative orientation of the total angular momentum ($\mathbf{j}$) depends on how the core of the nucleus is rotating whether it is following left or right handed system as shown in Figure. (2.9).

This chiral symmetry minimizes the total energy for a given spin and leads to two-fold degeneracy in the energy eigen values. These two energy eigenstates are denoted as $|L\rangle$ and $|R\rangle$ respectively. The total nuclear Hamiltonian is invariant under the chiral operator $TR_y(\pi)$ satisfying the following relation

$$[H, TR_y(\pi)] = 0 \tag{2.55}$$

where T represents time reversal and $R_y(\pi)$ a rotation about the intrinsic y axis by 180^0. However, under the $TR_y(\pi)$ operator,

$$TR_y(\pi)|L\rangle = |R\rangle \tag{2.56}$$

and

$$TR_y(\pi)|R\rangle = |L\rangle \tag{2.57}$$

Since the Chiral symmetry preserved by the Hamiltonian, which is broken for this solutions indicates the formation of chiral geometry in the intrinsic frame of rotating nuclei is an example of spontaneous symmetry breaking [52]

In the ideal case of strong symmetry breaking, i.e. $\langle L|H|R\rangle = \langle R|H|L\rangle^*$=0, any linear combination of the two is an eigen solution. However, those which can be observed in the laboratory frame are invariant under the chiral operator and given as

$$|+\rangle = \frac{1}{\sqrt{2}}(|R\rangle + |L\rangle) \tag{2.58}$$

$$|-\rangle = \frac{i}{\sqrt{2}}(|R\rangle - |L\rangle) \tag{2.59}$$

where

$$TR_y(\pi)|+\rangle = |+\rangle \tag{2.60}$$

$$TR_y(\pi)|-\rangle = |-\rangle \tag{2.61}$$

Each state with spin I in the rotational band is two-fold degenerate, and it cannot be associated with either purely left- or purely right-handed solution.

In case of weak symmetry breaking, the degeneracy is lifted via nonzero $\langle L|H|R\rangle = \langle R|H|L\rangle^*$. These off-diagonal matrix elements represent perturbations to a chiral geometry, in terms of an admixture of non-chiral planer component with pure $|L\rangle$ and $|R\rangle$ wave functions. Therefore, chiral geometry formation is a dynamical process as a function of spin(I).

Bibliography

[1] H. A. Bethe and R. F. Bacher. Rev. Mod. Phys. **8**, 82 (1936).

[2] C. F. Von Weizsčker, Z. Phys. **96**, 431 (1936).

[3] P. Ring and P. Schuck, The Nuclear Many-Body Problem Springer-Verlag Berlin Heidelberg (1980).

[4] R. D. Woods and D. S. Saxon. Phys. Rev. **95**, 577 (1954).

[5] O. Haxel, J.H.D. Jensen and H.E. Suess, Phys. Rev. **75**, 1766 (1949).

[6] M. G. Mayer, Phys. Rev. **75**, 1969 (1949).

[7] R. B. Firestone, et al., Table of Isotopes, CD ROM Edition 1996.

[8] G. Andersson, et. al., Nucl. Phys. **A 268**, 205 (1976).

[9] V. M. Strutinski Nucl. Phys. **A 95**, 420 (1967).

[10] V. M. Strutinski Nucl. Phys. **A 122**, 1 (1968).

[11] J. M. Eisenberg and W. Greiner. Nuclear Models. North Holland, Amsterdam, (1970).

[12] D. L. Hill and J. A. Wheeler Phys. Rev. **89**, 1102 (1953).

[13] S. G. Nilsson and I. Ragnarsson. Shapes and Shells in Nuclear Structure (Cambridge Univer- sity Press, UK, Cambridge, 1995).

[14] S. G. Nilsson. Mat. Fys. Medd. Dan. Vid. Selsk. **29**, 16 (1955).

[15] C. Gustafson et. al., Arkiv Ffsik **36**, 613 (1967).

[16] L. D. Landau and E. M. Lifshitz. Quantum Mechanics Non Relativistic Theory Chapter 11. Elsevier, Amsterdam, (2008) and Ref. there in.

[17] J. Rekstad and G. Løvhøiden. Nucl. Phys. **A 267**, 40 (1976).

[18] D. R. Inglis Phys. Rev **96**, 1059 (1954).

[19] D. R. Inglis Phys. Rev **103**, 1786 (1956).

[20] R. Bengston and S. Frauendrof. Nucl. Phys. **A 327**, 139 (1979).

[21] T. Bengston and I. Ragnarsson. Nucl. Phys. **A 436**, 14 (1985).

[22] W. Nazarewicz et al., Nucl. Phys. **A 435**, 397 (1985).

[23] W. Nazarewicz et al., Nucl. Phys. **A 512**, 61 (1990).

[24] S. Frauendrof and J. Meng Nucl. Phys.**617**, 131 (1997).

[25] T. Koike, K. Starosta and I. Hamamoto, Phys. Rev. Lett. **93** 172502 (2004).

[26] K. Starosta et al., Phys. Rev. Lett. **86**, 971 (2001).

[27] T. Koike et al.,, Phys. Rev. **C 63**, 061304(R) (2001).

[28] A. A. Hecht et al., Phys. Rev. **C 63**, 051302(R) (2001).

[29] D. J. Hartley et al., Phys. Rev. **C 64**, 031304(R) (2001).

[30] R. A. Bark, et al., Nucl. Phys. **A 691**, 577 (2001).

[31] X. F. Li et al., Chin. Phys. Lett.**19**, 1779 (2002).

[32] T. Koike et al., Phys. Rev. C **67**, 044319 (2003).

[33] G. Rainovski et al., Phys. Rev. **C 68**, 024318 (2003).

[34] A. J. Simons et al., J. Phys. **G 31**, 541 (2005).

[35] S. Y. Wang et al., Phys. Rev. **C 74**, 017302 (2006).

[36] C. Vaman et al., Phys. Rev. Lett. **92**, 032501 (2004).

[37] P. Joshi et al., Phys. Lett. **B 595**, 135 (2004).

[38] J. Sethi et al., Phys. Lett. **B 725**, 85 (2013).

[39] D. L. Balabanskiet al., Phys. Rev. **C 70**, 044305 (2004).

[40] E.A. Lawrie et al., Phys. Rev. C **78**, 021305 (R) (2008).

[41] J. Timer et al., Phys. Rev. C **73**, 011301 (R) (2006).

[42] T. Suzuki et al., Phys. Rev. C **78**, 031302 (R) (2008).

[43] J. Timer et al., Phys. Lett. **B 598**, 178 (2004).

[44] S. Zhu et al., Phys. Rev. Lett. **91**, 132501 (2003).

[45] S. Mukhopadhyay et al., Phys. Rev. Lett. **99**, 172501 (2007).

[46] J. Meng et al., Phys. Rev. **C 73**, 037303 (2006).

[47] J. Meng et al., Mod. Phys. Lett. **A 23**, 2560 (2008).

[48] A. D. Ayangeakaa et al., Phys. Rev. Lett. **110**, 172504 (2013).

[49] K. Starosta et al., Phys. Rev. Lett. **86**, 971 (2001).

[50] D. Tonev et al., Phys. Rev. Lett. **96**, 052501 (2006).

[51] C. M. Petrache et al., Phys. Rev. Lett. **96**, 112502 (2006).

[52] S. Frauendrof et al., Rev. Mod. Phys. **73**, 463 (2001).

Chapter 3

Experimental Techniques and Data Analysis

In order to study the nuclei in extreme condition i. e., at high excitation energy and angular momentum in neutron deficient nuclei, Fusion Evaporation reaction is the most suitable way to populate the high spin states in nuclei. Nuclear structure information is extracted in great detail by studying the various properties of the decaying discrete γ-rays. These properties include coincidence relation among various γ- transitions, intensity of the γ- transitions along with their multipolarity and polarization of the γ- rays and level life time of the states etc. The intensities of the γ- rays generally decrease as one goes up in angular momentum and excitation energy. Therefore, to study the high spin phenomena, one requires a high efficient γ- ray detection system to measure intensity and characteristics like multipolarity and polarization of the weakly populated γ- rays.

3.0.9 Generation of Angular Momentum

Although there are several methods such as fusion evaporation, β- decay, α- decay, inelastic excitation, transfer reaction, Coulomb excitation, deep inelastic excitation, nuclear fragmentation, fission etc. to populate both excitation energy as well as angular momentum in nuclei. All of these methods have their advantages as well as disadvantages. Fusion evaporation reaction is the widely used method for generating high spin states and excitation in nuclei near the yarst line.

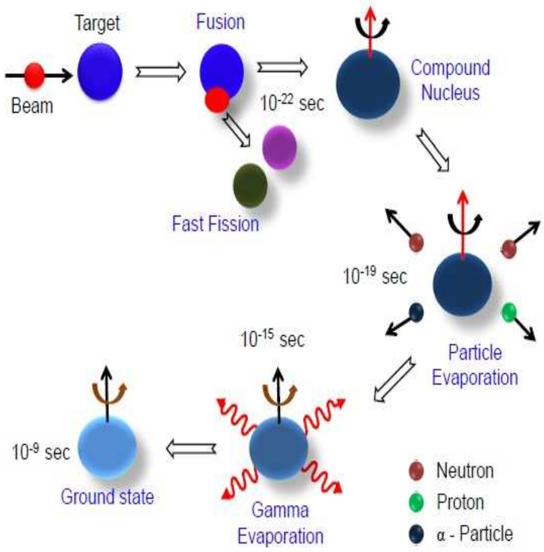

Figure 3.1: Schematic representation of various processes involved to the heavy-ion fusion-evaporation reaction.

In the schematic representation of fusion-evaporation process in Figure. (3.1) the projectile above the Coulomb barrier collide with the target nuclei and fuse together within a very short span of time (10^{-22} sec). Thereafter, the compound nucleus cools off by competition among particle evaporation (e. g., α, proton, neutron etc.) or high energy γ- ray (Giant dipole resonance) emission within the time scale of 10^{-17}-10^{-18} sec. Here the proton or α emission is considerably reduced due to Coulomb barrier offered by nucleus. Whereas the neutron evaporation is the dominant mode of nuclear de-excitation ($\sim$ 8 MeV per nucleon) but its distribution is isotropic, which leads to very small decrease of angular momentum ($\sim 1\hbar$ per particle). As the nuclei come down below the particle threshold line, it de-excites by emitting statistical (E1) γ transitions followed by E2 γ transitions along the nuclear "yarst line" as shown in Figure. (3.2) in a time period of 10^{-15}sec. The "yarst line" refers the locus of minimum excitation energy for a given value of the angular momentum.

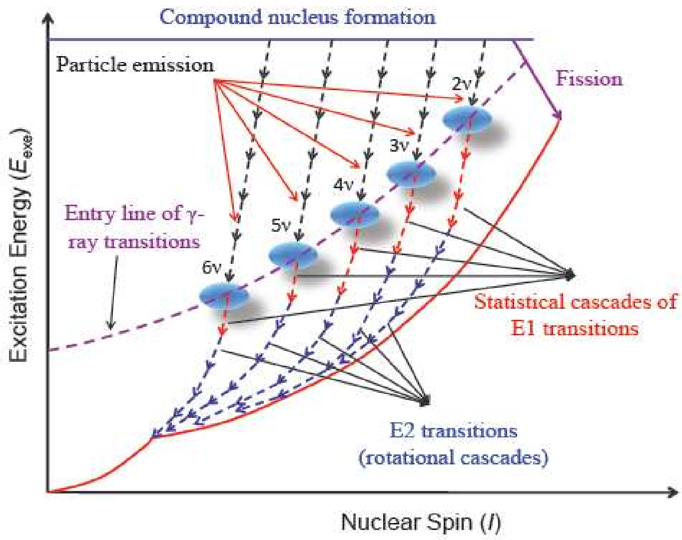

Figure 3.2: Excitation energy as a function of spin for the decay of compound nucleus in the heavy-ion induced fusion-evaporation reaction.

In a fusion-evaporation reaction, the kinetic energy of the collision in the centre of mass frame is converted into excitation energy of the compound system. The projectile having energy greater than Coulomb barrier, able to come closer to each other for fusion. The excitation energy (E_x) of the compound nucleus can be expressed as

$$E_x = Q + E_{CM} \tag{3.1}$$

where Q is the Q- value for the formation of the compound nucleus.

$$Q = M_P + M_T - M_{CN} \tag{3.2}$$

Here M_P, M_T and M_{CN} are the masses of the projectile, target and compound nuclei, respectively. The center-of-mass (E_{CM}) energy of the compound nucleus can be expressed in terms of laboratory frame energy E_b of projectile as follows

$$E_{CM} = \frac{M_T}{M_P + M_T} E_b \tag{3.3}$$

Another important parameter for nuclear reaction is the impact parameter R, which is defined as the distance between the centers of the target and projectile nuclei. Different nuclear reactions depending on the impact parameter(R) are shown in Figure. (3.3). The maximum angular momentum (λ_{max}) transferred to a compound nucleus depends on the impact parameter(R) [1], reduced mass(μ) and Coulomb barrier(V$_c$) between the target and projectile nucleus as described in the following Eqs.

$$l_{max} = \sqrt{\frac{2\mu R^2}{\hbar^2}(E_{CM} - V_c)} \tag{3.4}$$

$$\mu = \frac{M_T M_P}{M_P + M_T} \tag{3.5}$$

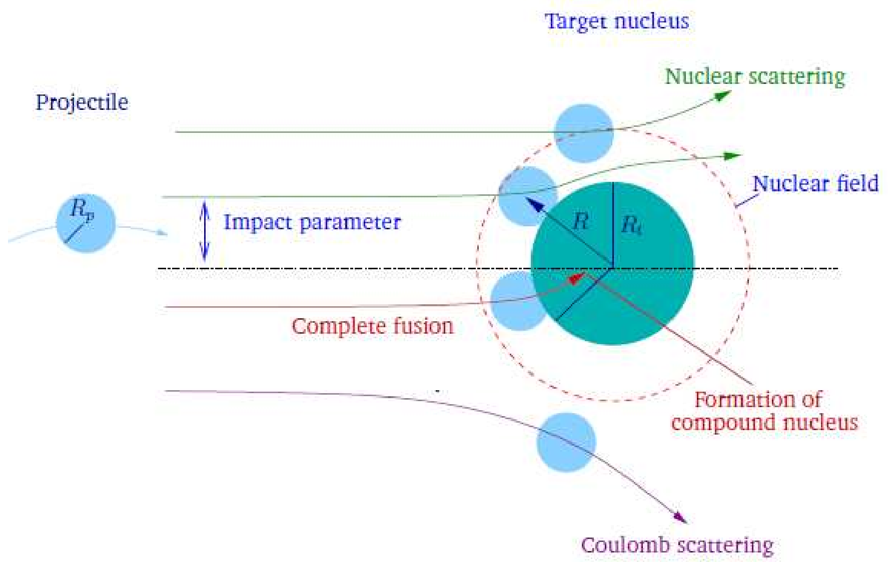

Figure 3.3: Schematic representation of various types of heavy ion collision depending on impact parameter(R).

$$R = 1.36(A_P^{\frac{1}{3}} + A_T^{\frac{1}{3}}) + 0.5 \tag{3.6}$$

where A_P and A_T are the mass numbers of the projectile and target nucleus respectively, which decides the impact parameter between the target and projectile nucleus in accordance with the Bass formula [2]. Whereas V_c is represents the Coulomb barrier between the target and the projectile nuclei which is given by the Eq.

$$V_c = 1.44\frac{Z_P Z_T}{R} \tag{3.7}$$

3.0.10 γ Ray Detection

In fusion evaporation reaction, after emission of statistical γ transitions, nucleus undergoes de-excitation by emission of E2 cascade γ transition along the nuclear yarst line. These γ -rays carry crucial information regarding the nuclear energy levels. It is very essential to have an efficient and high resolution detector system to bring out as much as nuclear structure information as possible. The incident γ- ray transfers kinetic energy to the electrons in the detector material which ultimately produces electrical signal. These electrical signals are proportional to the incident γ energy. So it is important to know the interaction procedure of the γ- ray with detector medium.

Interaction of γ Ray with Matter

There are basically three way by which incident γ -ray interact with the detector material such as <i> Photoelectric effect <ii> Compton effect <iii> Pair production.

<i>Photo electric effect:

The Photoelectric effect involves the absorption of a photon by an atomic electron with the subsequent ejection of electron from the atom with kinetic energy

$$E = h\nu - B.E \tag{3.8}$$

where hν is the incident photon energy and B.E is the binding energy of the electron. For simultaneous conservation of momentum as well as energy, the incident photon in this process transfers energy to the inner shell electrons and momentum to the nucleus. The cross-section for removing electron from the K shell of the atom is given by [3]

$$\sigma_{phK} = \frac{6.3 \times 10^{-18}}{Z^2}(\frac{\nu_k}{\nu})^{\frac{8}{3}} \tag{3.9}$$

where ν_k and ν are the frequency required for removing K orbital electron and incident photon. Whereas the total cross-section for the photoelectric effect can be given as [3]

$$\sigma_{ph} = 4\alpha^2\sqrt{2}Z^5\phi_0(\frac{m_0c^2}{\hbar\nu})^{\frac{7}{2}} \qquad \text{per atom} \tag{3.10}$$

$$\phi_0 = 8\pi r_e^2/3 = 6.651X10^{-25}cm^2 \qquad \alpha = 1/137 \tag{3.11}$$

here r_e is the classical electron radius. It can be seen from the Eq.(3.10) that the photo-electric cross-section has a large dependence on the atomic number Z of the material. A γ- ray undergoing photoelectric effect, deposits its full energy into the detector medium which leads leads into a photopeak in the spectra.

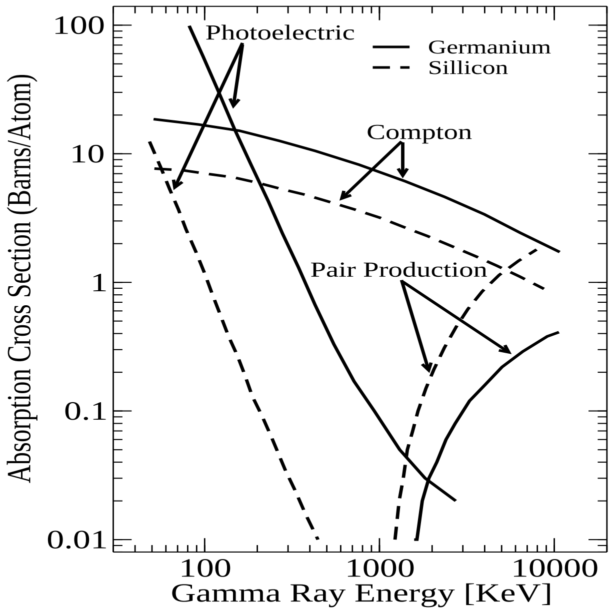

Figure 3.4: Relative probability of each type of γ- ray interaction with matter as a function of energy for Ge(Z=32) and Si(Z=14) [4].

<ii>Compton effect:

In Compton scattering an incident photon of energy E_γ scattered from a free electron with an energy $E'_\gamma < E_\gamma$, is emitted at an angle θ with respect to the incident direction. The energy of the scattered photon depends on the scattering angle as

$$E'_\gamma = \frac{E_\gamma}{1 + (E/m_e c^2)(1 - \cos\theta)} \tag{3.12}$$

where m_e ($m_e c^2 = 0.51$ MeV) is the rest mass of the electron. The energy difference $E_e = E_\gamma$ -E'_γ is transferred to the electron as it's kinetic energy. While the incident γ gets scattered at 180^0 to the incident direction, the maximum energy is transferred to the scattering electron.

$$E_e = \frac{2E_\gamma^2/m_ec^2}{1+2E_\gamma/m_ec^2} \tag{3.13}$$

When this scattered electron gets absorbed in the detector, it gives rise to Compton edge below the incident γ energy in the spectrum by

$$E_{ce} = \frac{1}{1+2E_\gamma/m_ec^2} \tag{3.14}$$

where E_{ce} is the Compton edge energy. In the Compton effect the γ- ray deposits partial energy into the detector medium. Therefore the Compton scattered events normally contributes to the background in the spectra. However it can undergo multiple Compton scattering and totally absorbed inside the detector. As a result of which we usually see the photopeak of the incident γ- ray lies above the continuous Compton background.

<iii> Pair-production:

This process dominates at higher energies (E_γ> 1 MeV). If the incident γ has an energy E_γ $\geq$ 2m_ec^2 = 1.022 MeV, a part of the incident energy goes into the production of electron-positron pair and rest of the energy goes into the kinetic energy of the pair. The electrons produce the electrical signal whereas the positrons gets annihilated by interacting with the electrons inside the detector material. The pair of γ- rays each of energy 511 keV produced in the annihilation process gets absorbed inside the detector. However if one of these γ- rays escapes the detector one gets the first escape peak at an energy 511 keV below the incident γ- energy. On the other hand if both the γ- rays escape the detector then one gets a peak at 1.022 MeV below the incident γ- energy.

A comparative representation of variation of absorption cross-section for photo-electric, Compton and pair-production with incident gamma ray energy for Ge(Z=32) and Si(Z=14) materials is shown in Figure. (3.4).

3.0.11 Detectors

The combination of all these effects ultimately gives rise the electrical signal proportional to the incident γ ray energy. But in order to extract maximum nuclear structure information through γ- ray spectroscopy one requires high energy resolution and efficient (maximum solid angle coverage) spectrometer. The scintillator detector like Sodium Iodide (NaI) or Bismuth Germanate ($Bi_4Ge_3O_{12}$) (BGO) have high efficiency but very poor energy resolution whereas the semi-conductor detectors made up of High-Purity Germanium (HPGe) crystals have excellent energy resolution ($\sim$ 2 keV at 1332 keV of ^{60}Co peak) but poor energy efficiency. In a spectra of HPGe detector, large unwanted background comes due to Compton effect. In order to minimize this background an anti- Compton shield made up of BGO detector along with HPGe detector, are used in making large detector array for gamma- ray spectroscopy.

3.0.12 Clover Detector

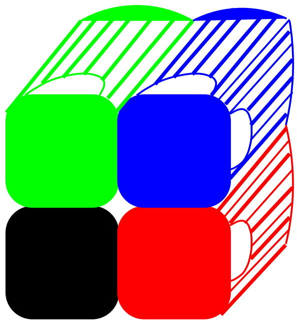

Figure 3.5: Schematic representation of four crystals of a HPGe clover detector.

A clover HPGe detector consists of four crystals like clover leafs [5] (see Figure. (3.5)) arranged at the front side of a cryostat as shown in Figure. (3.6). Each crystal is of 50 mm in diameter and 70 mm in length. Usually, the crystals are at $\sim$ 20 mm away from the outer face of the detector aluminium cage (including 1.5 mm cap thickness). The crystal front face is designed to be tapered to accommodate close packing inside the aluminium cage. These crystals are connected with liquid nitrogen dewar with cold finger. In order to reduce the Compton background, the clover detector is surrounded by anti-Compton shield of scintillator detector made up of Bismuth Germanate (BGO). As the incident γ-ray gets scattered from any of the crystals and hits the anti-Compton shield are rejected as valid events which considerably improves the quality of the γ- energy spectrum.

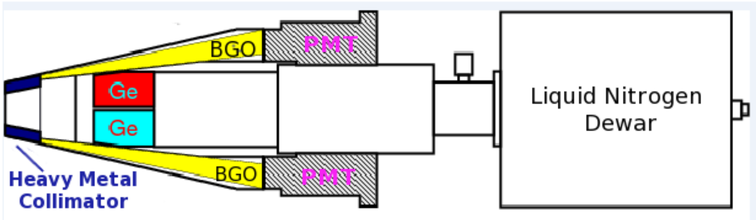

Figure 3.6: Schematic diagram of a clover detector capsulated by BGO anti-Compton shield.

The biggest advantages of these four crystal arrangement in clover detector are it can be used in add-back mode to increase the photopeak efficiency and Compton polarimeter for γ- ray polarization measurement.

These four crystal arrangement in a clover detector have many salient features over large single crystal germanium detector of equivalent volume. The individual clover crystals work as an independent detector of smaller granularity, which considerably reduces the Doppler broadening on the resulting spectrum. As the individual crystal size is smaller, the timing response considerably improves over a same volume single crystal HPGe detector.

It is clear from Figure. (3.5), when high energy γ- ray falls on a crystal, it gets Compton scattered to its neighbouring crystals. Thus, it is possible to register events in time correlated "add-back" mode in two clover crystals where Compton background adds up to give photopeak. Therefore in the add-back spectrum the peak-to-total ratio improves considerably.

The clover detector can also be used as a polarimeter, where the incident γ- ray gets Compton scattered to two neighbouring crystals, acts as both scatterer and absorber. As the Compton scattered events are preferentially restricted to horizontal and vertical axis with respect to the detector surface depending on the magnetic or electric nature of the γ- transition, can be used to determine the polarity of the γ- transition by comparing the efficiency corrected spectrum in the vertical and horizontal crystals.

In recent time nuclear structure properties are investigated world wide with the use of these type of BGO encapsulated (anti-Compton shield) HPGe detector array for both prompt and delayed spectroscopy.

3.0.13 Indian National Gamma Array

The use of large detector array (Gammasphere, Euroball, Jurogam, Afrodite etc.) in γ-ray spectroscopy has opened up new era in nuclear structure physics. These high efficient γ detector arrays allowed us to observe very weak γ transitions in prompt gamma ray spectroscopy which produce crucial information regarding nuclear levels and many new exotic phenomena like Magnetic Rotation, Anti-Magnetic Rotation, Chirality, Superdeformation, Wobbling phenomena etc.

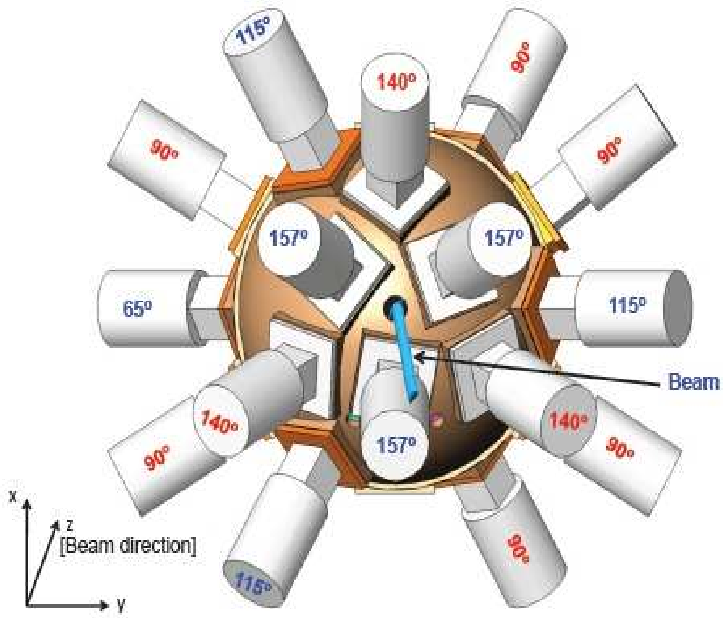

Figure 3.7: Schematic representation of Compton-suppressed clover detectors of Indian National Gamma Array at TIFR with the detectors angular arrangements with respect to beam axis(z) [6].

The Indian National Gamma Array (INGA) is a multi-detector array in India. It is a collaborative effort of various research institutes and various Universities in India. INGA moves between three major accelerator facility in India *i.* e., Tata Institute of Fundamental Research (TIFR)- Mumbai, Inter University Accelerator Centre (IUAC)- New Delhi and Variable Energy Cyclotron Centre (VECC)- Kolkata. During the present work, INGA was installed at TIFR- Mumbai. This array was designed to consist of 24 clover detectors with anti-Compton shield arranged in six different azimuthal angles. Among which four detectors each at 90^0 and three detectors each at 23^0, 40^0, 65^0, 115^0, 140^0 and 157^0 with respect to the beam direction are arranged as shown in Figure. (3.7). These detectors are placed $\sim$ 25 cm from the target position. In the add-back mode the overall photo-peak efficiency of the array is ~ 5 % for $E_\gamma \sim 1$ MeV and energy resolution of the detectors are ~ 2 keV at 1.33 MeV γ- ray of ^{60}Co.

A digital data acquisition (DDAQ) system, based on Pixie-16 modules developed by XIA LLC [7] with 112 channels has been used for the present experiment. This system has the capability of digitization of 96 channels of 24 clover detectors with 100 MHz sampling rate which can operate both in trigger-less as well as multi-fold coincidence mode which is shown in the block diagram in Figure. (3.8) .

Time stamped coincidence data were collected when at least two clover detectors were fired in a time window of 150 ns between the first triggers of individual channels, opened for 1.5 μs. The BGO signal from the anti-Compton shield of the respective clovers were used for vetoing the individual channels. The detailed description of the DDAQ can be obtained from Ref. [8].

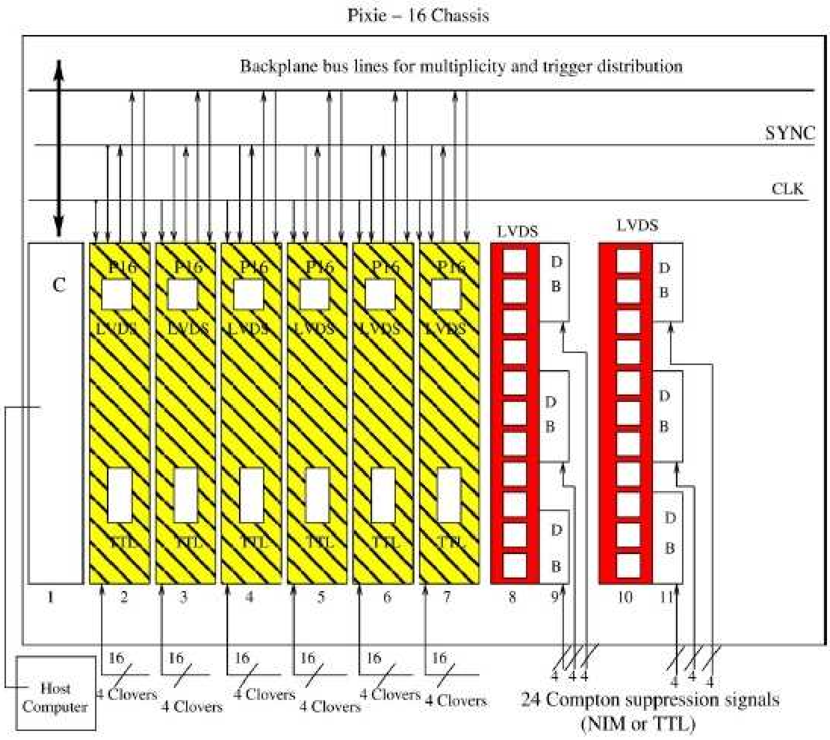

Figure 3.8: Block diagram for the digital DAQ for 24 Compton suppressed clover detectors. It consists of six Pixie-16 modules; two LVDS level translator modules and one controller arranged in a single compact PCI/PXI crate [8].

The time stamped data were sorted using "**M**ulti p**AR**ameter time stamped based **CO**incidence Search program **(MARCOS)** " developed at TIFR [8] for generating $E_\gamma - E_\gamma$ matrix and $E_\gamma - E_\gamma - E_\gamma$ cube in Radware compatible format.

On the other hand for delayed gamma ray spectroscopy like in long lived isomer decay study or nuclear structure study above those isomers are carried out using mass spectrometers as an auxiliary device along with clover detector. The fusion evaporation reaction for the production of nuclei A $\sim 190 - 200$ region considerable amount of fission product obscures the gamma- ray spectrum of the nucleus of interest. Therefore to reduce fission background, mass spectrometers are used to select the evaporation residue (ER) and study their decay properties at a focal plane away from the target site.

3.0.14 HYbrid Recoil mass Analyzer(HYRA)

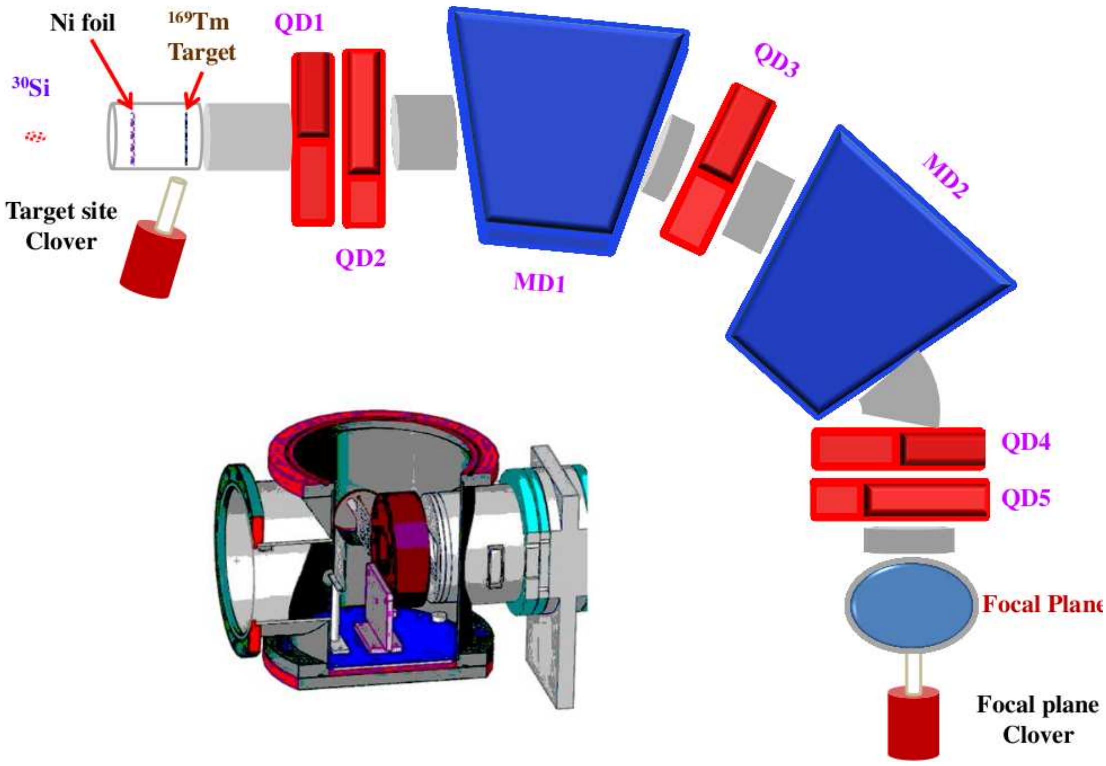

Figure 3.9: Schematic representation of HYbrid Recoil mass Analyzer (HYRA) and its focal plane flange.

The HYbrid Recoil Mass Analyzer (HYRA) is a dual mode spectrometer come separator, capable of operating in both gas filled (in normal kinematics to access heavy nuclei around $\sim$ 200 amu) as well as in vacuum mode (in inverse kinematics to access nuclei around N$\sim$Z upto 100 amu) is shown in Figure. (3.9). In fusion-evaporation reaction, typical beam current is of the order of $10^{10}...10^{13}$ particles/sec, which leads to unattenuated passage of beam current through the target along with a considerable contribution of fission fragments.

Mass separator, like this, separates the forward focused (around 0^0 with respect to the beam direction) primary beam, target like contamination and fission products from the evaporation residues (ERs) and ERs to pass through the spectrometer focal plane for isomeric decay measurement and spectroscopy of weakly populated nuclei more precisely. The basic principle for separation of different reaction product from evaporation residues depends on different magnetic rigidity Bρ for the beam and residues given by

$$B\rho = \frac{\sqrt{2Em}}{q_{av}} = \frac{\sqrt{2Em}}{(\frac{V}{V_0})Z^{\frac{1}{3}}} = 0.0227\frac{A}{Z^{\frac{1}{3}}} \tag{3.15}$$

where E, m, q_{av}, A and Z represents the energy, mass, average charge, mass number and atomic number of the ions respectively. Whereas B and ρ represents the magnetic field strength and radius of curvature of the dipole magnet. V_0(=2.19×10^6 m/s) is the Bohr velocity, determines how the charge state is going to be equilibrated when it passes thorough a gaseous medium [10, 11].

At the focal plane chamber one multiware proportional counter (MWPC) and three Si-pad detectors were placed along with a clover detector through a re-entrant cup as shown in Figure. (3.10). Further details about HYRA and its detector specifications can be found in chapter-4 and Ref. [12].

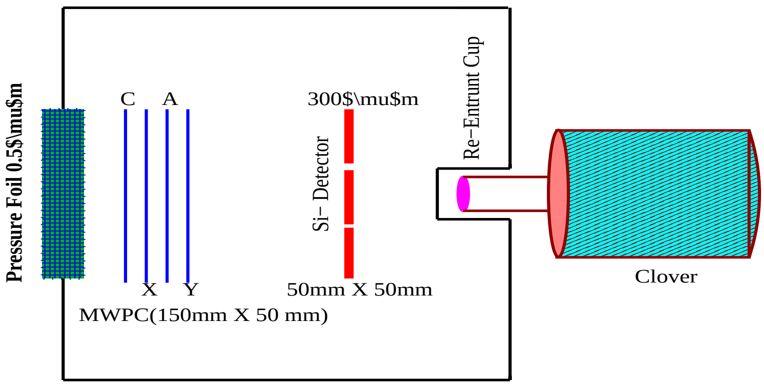

Figure 3.10: Detector setup at the focal plane of HYRA. It consist of one MWPC followed by three si-pad detectors and outside the flange a clover detector placed through a re-entrant cup.

This type of set up is ideal for isomeric decay study whose life-time is of the order of time of flight path of evaporation residues (ER) reaching to the focal plane and undergoes subsequent γ- decay there.

3.0.15 Target Fabrication

In order do isomeric decay study at the focal plane of HYRA, thin target was needed so that ER's reaches to the focal plane without depositing much of its kinetic energy inside it. At the same time ^{169}Tm is a malleable material and rolling was a quite efficient in terms of less loss of the expensive target material. Therefore, target for ^{195}Bi study was prepared with the rolling method at IUAC- New Delhi. A small slice of (^{169}Tm) was taken from a 25 mg/cm^2 thick sample which was placed between two mirror polished stainless steel plates and rolled through specially hardened rollers. The gap between the rollers is reduced gradually to achieve thinner foils. The rolling machine used for target preparation is shown in Figure. (3.11)

Figure 3.11: Rolling machine used for target fabrication at IUAC- New Delhi.

During rolling the sample got wrinkles at edges so it had to be trimmed from that side, to stop it spreading over the target area. Also repeated rolling of the stainless steel plate causes it to bend sideways, therefore extra care had to be taken of target sample while changing one plate to other. At the same time friction between the target material and stainless steel plate causes enough static electrical charge which can oxidize the target material, therefore insulating wrist band need to be worn while rolling. Ultimately two thin targets of 0.80 and 0.86 mg/cm^2 were made by this method. Their masses were measured in air tight weight machine and their area were measured using graph paper in order to determine their thickness.

Data Analysis Technique

3.0.16 Energy and Efficiency Calibration

The pulse height proportional to the energy of the incident γ rays are digitized using Analog to Digital Converter (ADC) and plotted as a γ- ray spectrum for each clover detector where the channel number of the spectrum is proportional to the energy of the incident γ-ray baring there is no offset. Usually there might be gain difference among the various detectors, so it is essential to establish the correlation between channel and energy using standard radioactive γ- sources ^{152}Eu and ^{133}Ba for calibration. The known γ lines of these sources are identified and their respective channel numbers are calibrated using the polynomial fit of the form

$$E = \sum_{n=1}^{k}(a + b_n x^n) \tag{3.16}$$

where E is the energy of the incident γ ray in keV and x is the channel number, usually upto quadratic fit is sufficient but below 200 keV gamma- ray energy a factor $\sqrt{x}$ has been included in the above Eq. (3.16).

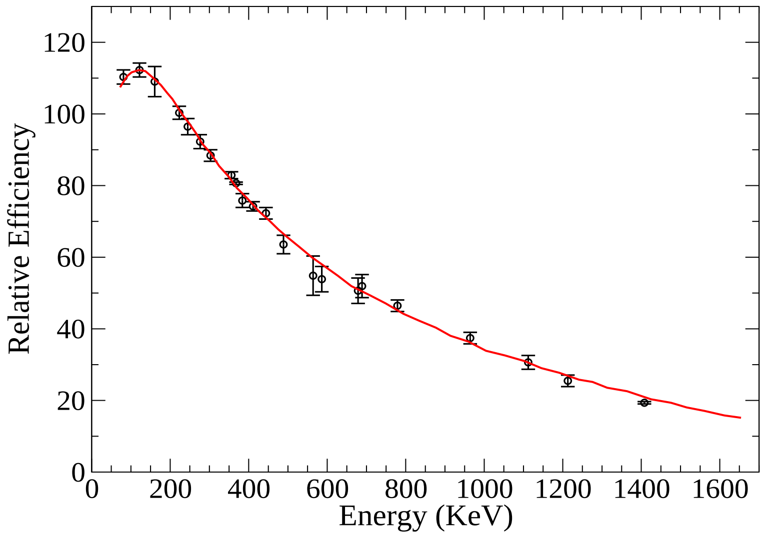

Figure 3.12: Relative efficiency curve for fifteen clover detectors of INGA using ^{152}Eu and ^{133}Ba source. Solid line obtained by fitting the data points using Eq. (3.18)

.

Therefore in this thesis work the following Eq. was used for calibration

$$E = a + bx + cx^2 + d\sqrt{x} \tag{3.17}$$

The coefficients a, b, c, d were obtained by fitting the channel number vs energy curve for ^{152}Eu and ^{133}Ba source.

In γ- ray spectroscopy only relative intensities of the detected γ- rays are important, so relative efficiency of the detector array need to be determined. This photopeak efficiency of the detector varies with γ- ray energy. The relative efficiency of the detectors are measured by determining the area under the known γ- lines from the radioactive sources ^{152}Eu and ^{133}Ba and dividing by their standard intensities. These data points which are shown as open circle in Figure. (3.12) are fitted with the EFFIT program of RADWARE package [22]. In this program the following Eq. was used to fit the relative efficiency

$$ln(\epsilon) = [(A + Bx + Cx^2)^{-G} + (D + Ey + Fy^2)^{-G}]^{-1/G} \tag{3.18}$$

where ϵ is the efficiency, x = ln(E_γ/100) and y = ln(E_γ/1000). A, B, and C parameters are used to fit for low energy while D, E, and F are used to fit for higher energy region with E_γ in keV [22]. The parameter G determines the shape of the turn-over region between the high energy and low energy part of the efficiency curve. The fitted curve is shown by the solid line in Figure. (3.12). In order to get good efficiency and energy calibration the radioactive sources (^{152}Eu and ^{133}Ba) are mounted at the target site with same detector configuration both before and after the experiment.

Add Back Mode in Clover Detector

A great advantage of composite detector like clover is that the high energy γ-ray after Compton scattering goes to its neighbouring crystals, which can be added to get full photopeak energy. At the same time it also improves the over all peak-to-total ratio (P/T) [5]. To get the add-back spectrum the time correlated signals from all four crystals in an event of a detector are added after proper gain matching of the individual crystal data.

Coincidence Relation between γ rays

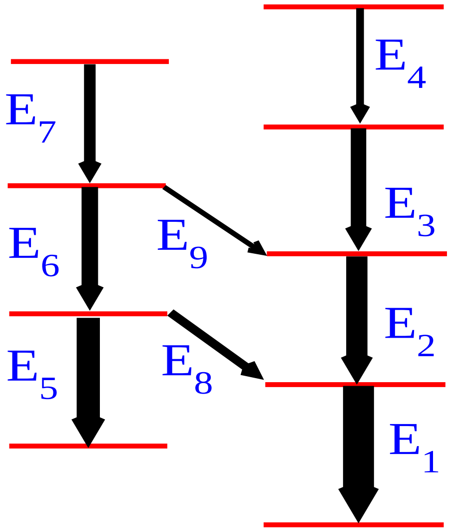

Figure 3.13: Example of level scheme demonstrates the gamma- ray coincidence relation (see text below).

A level scheme of a nucleus is a pictorial representation of its excited states which carries the information regarding the decaying γ transition intensity, multipolarity and type [Electric(**E**) or Magnetic(**M**)]. In Figure. (3.13) there is a representation of nuclear level scheme which is constructed from the coincidence among different γ- rays. From E_γ-E_γ matrix one will see E_1 γ is in coincidence with all transitions except E_5, whereas E_5 is in coincidence with only E_6 and E_7 γ-rays only. In E_γ-E_γ-E_γ cube, if someone puts double gate on E_1 and E_2 γ-rays one can see E_3, E_4, E_7 and E_9 γ- transitions. At the same time putting gate on E_5 and E_6 transitions one can only see E_7 γ- transition.

In the fusion evaporation reaction the intensity of the γ rays decreases as one moves up in angular momentum as well as in excitation energy. Therefore, during building level scheme, the intensity balance at each energy level is needed to be looked very carefully.

The total intensity of the lower transitions will always be higher than that of the upper one. In order to calculate the total intensity one needs to know the conversion coefficient for each γ- transition. Again conversion coefficient is highly dependent on multipolarity, type (E/M) and the energy of the γ- transition.

Spin and Parity assignment of the Excited States

After the construction of the level scheme from the coincidence relation and intensity information, the next step is to assign spin and parity of the individual levels. This can be done by determining the multipolarity and type of the decaying γ- transitions through angular distribution, angular correlation and linear polarization measurement.

3.0.17 Gamma ray selection rule

These electromagnetic radiation happens through γ- ray emission which are strongly spin and parity dependent. The selection rule, which dictates the allowed multipoles λ are:

$$I_i - I_f \leq \lambda \leq I_i + I_f \tag{3.19}$$

$$\begin{aligned} \pi_i\pi_f &= (-1)^{\lambda} \qquad \text{for electric} \\ \pi_i\pi_f &= (-1)^{\lambda+1} \quad \text{for magnetic} \end{aligned} \tag{3.20}$$

.

From the experimental point of view, the $\lambda = 1$ dipole and $\lambda = 2$ quadrupole are the most frequently occurring multipoles of the γ-ray transitions.

3.0.18 Angular Distribution

In heavy-ion fusion evaporation reaction the spins of the nuclear excited states are aligned perpendicular to the reaction plane [14, 15]. If the spin (I) of the nuclear state and its component along the symmetry axis (m), [i. e., along the beam axis] the relative population of the m th substate $P_m(I)$ [16] is given by the following Eq.

$$P_m(I) = \frac{exp(-\frac{m^2}{2\sigma^2})}{\sum_{m'=-I}^{I} exp(-\frac{m'^2}{2\sigma^2})} \tag{3.21}$$

where σ is the measure of the alignment and is usually given in terms of σ/I. If the nuclear state satisfies $P_m(I) = P_{-m}(I)$ condition then that state is considered aligned. In case of $\sigma \rightarrow 0$, it corresponds to complete alignment. The gamma- rays emitted from the aligned states show characteristic angular distributions depending on their multipolarities and the spins of the involved states [15]. The angular distribution of a γ- ray of multipole order λ can be expressed as follows

$$W_l(\theta) = \sum_{k=0}^{l} a_{2k} P_{2k}(\cos\theta) = a_0 + a_2 P_2(cos\theta) + a_4 P_4(cos\theta) + ... + a_{2l} P_{2l} cos(\theta) \tag{3.22}$$

where a_{2k}'s are the angular distribution coefficients and P_{2k}'s are the Legendre polynomials. In experiments mostly dipole ($\lambda = 1$), mixed (dipole + quadrupole) and quadrupole ($\lambda = 2$) transitions are observed which are shown in Figure. (3.14). Here 552.8 keV is a mixed (dipole + quadrupole) transition whereas 821.6 keV is a stretched quadrupole transition (belonging to ^{195}Tl) based on their angular distribution coefficients A_2^{exp} and A_4^{exp}, determined by fitting the angular distribution yeild for the respective γ-rays with the following Eq. (3.25).

$$W(\theta) = 1 + A_2^{exp} P_2(\cos\theta) + A_4^{exp} P_4(\cos\theta) \tag{3.23}$$

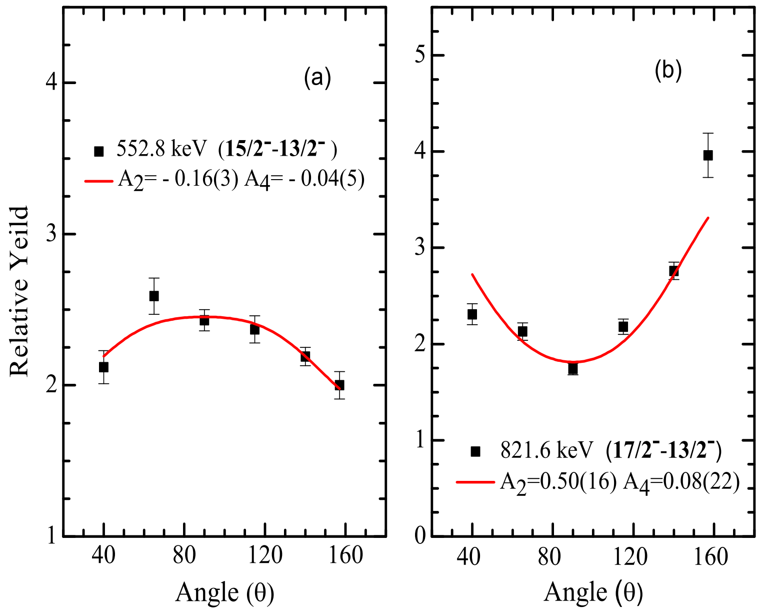

Figure 3.14: Typical gated angular distribution obtained in the present work for (left panel: 552.8 keV mixed dipole+quadrupole and right panel: 821.6 keV stretched quadrupole) γ- transitions belonging to ^{195}Tl.

In case of maximum alignment the angular distribution coefficients can be expressed as

$$A_k^{max}(I_i L_1 \lambda_2 I_f) = \frac{1}{1+\delta^2}[f_k(I_f \lambda_1 \lambda_1 I_i) + 2\delta f_k(I_f \lambda_1 \lambda_2 I_i) + \delta^2 f_k(I_f \lambda_2 \lambda_2 I_i)] \tag{3.24}$$

While f$_k$ (I$_f\lambda_1\lambda_2 I_i$) is Tabulated in Ref. [16] in terms of

$$f_k(I_f \lambda_1 \lambda_2 I_i) = B_k(I_i) F_k(I_f \lambda_1 \lambda_2 I_i) \tag{3.25}$$

where

$$F_k(I_f\lambda_1\lambda_2I_i) = (-)^{I_f-I_i-1}[(2\lambda_1+1)(2\lambda_2+1)(2I_i+1)]^{1/2}$$
$$X < \lambda_1 1\lambda_2 - 1|k0 > W < I_iI_i\lambda_1\lambda_2; kI_f > \tag{3.26}$$

and B_k is the statistical tensor for the complete alignment given by Eq.

$$\begin{aligned} B_k(I) &= (2I+1)^{1/2}(-)^I < I0I0|k0 > \qquad \text{for integral spin} \\ &=(2I+1)^{1/2}(-)^{I-\frac{1}{2}} < I\frac{1}{2}I\frac{-1}{2}|k0 > \quad \text{for half-integral spin} \end{aligned} \tag{3.27}$$

here $< \lambda_1 1\lambda_2 - 1|k0 >$ and $< I0I0|k0 >$ are the Clebsch-Gorden coefficients and W is Racah coefficient.

Whereas δ is the mixing ratio defined in the following manner

$$\delta = \frac{< I_f||\lambda_2||I_i >}{< I_f||\lambda_1||I_i >} \tag{3.28}$$

usually in partial alignment maximum angular distribution (A_k^{max}) coefficient has to be modified with the attenuation coefficient $[\alpha_k(I_i)]$ [17] to get the experimental angular distribution as follows

$$A_k(I_f\lambda_1\lambda_2I_i) = \alpha_k(I_i)A_k^{max}(I_f\lambda_1\lambda_2I_i) \tag{3.29}$$

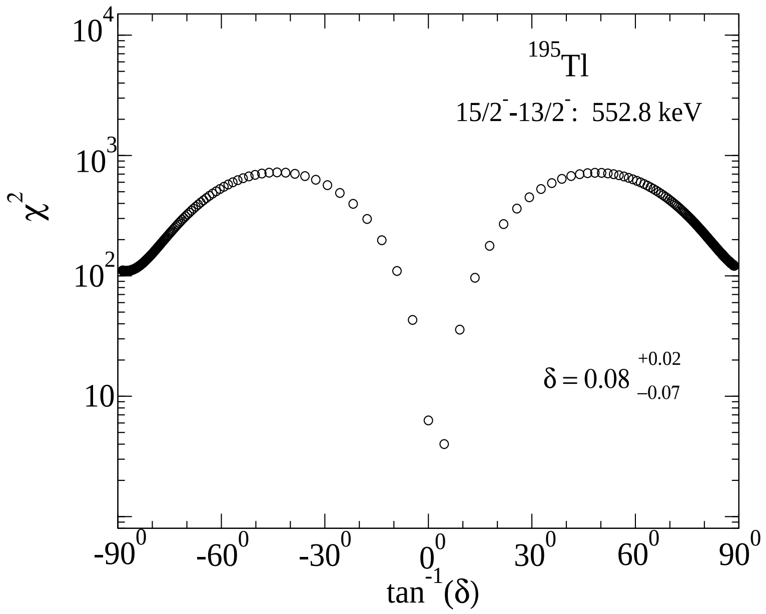

Figure 3.15: The χ^2 fit of 552.8 keV γ- ray for the mixed dipole-quadrupole multipolarity are plotted as a function of mixing ratio (δ).

$$\chi^2 = \sum_{k=2,4} (\frac{A_k^{exp} - A_k}{\Delta A_k^{exp}})^2 \tag{3.30}$$

Since A_k is a function of δ as specified in Eq. [3.24-3.29], the variation of χ^2 of the mixed (dipole + quadrupole) 552.8 keV gamma- transition has been plotted in Figure. (3.15) as a function of mixing ratio (δ) using Eq. (5.4). Here ΔA_k^{exp} is the uncertainty in the experimental angular distribution coefficient A_k^{exp}. Experimentally δ of a mixed transition is determined for that value of δ for which χ^2 is minimum. In case of 552.8 keV gamma-ray δ comes out to be $0.08^{+0.02}_{-0.07}$ in the present study.

3.0.19 Directional Correlation Ratio (DCO)

The angular distribution of a γ- ray transition is obtained for singles spectra without any coincidence at different detector angles. But in heavy ion fusion-evaporation reaction many nuclei are populated simultaneously which makes it very difficult to measure angular distribution of each γ- transitions without contamination from nearby γ- rays. Also limited number of angular combination in modern day γ detector arrays constrains full angular distribution. So multipolarity of the γ- transitions are measured by Directional Correlation Ratio ($\mathbf{R_{DCO}}$), following the prescription of Krämer- Flecken et. al., [18].

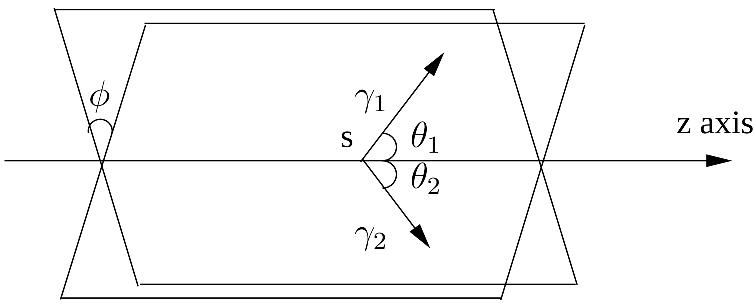

Figure 3.16: The angles between the planes (ϕ) in a directional correlation of two successive gamma transitions γ_1 and γ_2 emitted from a source(S) nucleus.

Two successive gamma- rays γ_1 and γ_2 emitted from an aligned state observed at angles θ_1 and θ_2 with respect to the beam axis as shown in Figure. (3.16) with angle ϕ, where ϕ is the angle between the two planes defined by the direction of the emitted γ- rays and the z axis. The correlation intensity W (θ_1, θ_2, ϕ) can be defined as [19]

$$W(\theta_1, \theta_2, \phi) = \sum_{\lambda_1 \lambda \lambda_2} B_{\lambda_1}(I_1) A_{\lambda}^{\lambda_2 \lambda_1}(\gamma_1) A_{\lambda_2}(\gamma_2) H_{\lambda_1 \lambda \lambda_2}(\theta_1 \theta_2 \phi) \tag{3.31}$$

where B_λ describes the alignment of the state with respect to the beam axis (i, e., z axis), the coefficient A contains the physical parameters like spins of the states, multipolarities and mixing ratio of the transitions. $H_{\lambda_1\lambda\lambda_2}(\theta_1\theta_2\phi)$ contains the angular information of the transitions and the index λ refers to the tensor rank of the radiation field with $\lambda = 0$ corresponds to the non observation of radiation field in a particular direction. The DCO ratio is given as

$$R_{DCO} = \frac{W(\theta_2, \theta_1, \phi)}{W(\theta_1, \theta_2, \phi)} \tag{3.32}$$

An asymmetric $\gamma-\gamma$ matrix is sorted with one axis containing forward or backward detector data with the other axis containing data of 90^0 detector to measure the experimental R_{DCO} ratio as given by

$$R_{DCO} = \frac{I_{\gamma_1}(\theta_1)(Measured\ at\ \theta_1;\ Gated\ by\ \gamma_2\ at\ \theta_2)}{I_{\gamma_1}(\theta_2)(Measured\ at\ \theta_2;\ Gated\ by\ \gamma_2\ at\ \theta_1)} \tag{3.33}$$

If a gate is made on stretched quadrupole γ- transition then the R_{DCO} ratio comes out to be $\sim$ 1.0 for stretched quadrupole transition and 0.5 or 2.0 for stretched dipole transition. The theoretical R_{DCO} ratios are calculated using the software code ANGCOR [23]. For mixed γ- transitions the R_{DCO} value has large dependence on the mixing ratio(δ). In the present analysis the R_{DCO} values are obtained for $\theta_1 = 90^0$ and $\theta_2 = 157^0$.

3.0.20 Linear Polarization of γ transitions

The DCO ratio measurement allows us to measure the multipolarity of the γ- transition but it doesn't provide any information regarding the nature of the γ- transition i,e., whether it is electric(E) or magnetic(M) type. So this information can be obtained from the gamma- ray linear polarization measurement. The close arrangement of crystals in a clover detector allows the Compton scattered events to scatter from one crystal to the neighbouring crystals. Therefore, Compton scattering technique has become an efficient method of measuring the linear polarization of the γ- transitions decaying from the excited nuclear state. The differential cross-section of the γ- ray of energy E_γ, Compton scattered into γ' with energy E'_γ can be obtained by the Klein-Nishina formula [21].

$$\frac{d\sigma}{d\Omega} = (\frac{r_0^2}{2})(\frac{E'_\gamma}{E_\gamma})^2[\frac{E'_\gamma}{E_\gamma} + \frac{E_\gamma}{E'_\gamma} - 2\sin^2\theta\cos^2\phi] \tag{3.34}$$

where θ is the Compton scattering angle with respect to the incident γ- ray direction and ϕ is the azimuthal angle between the Compton scattering plane and polarization plane of the incoming γ- transition as shown in Figure. (3.17).

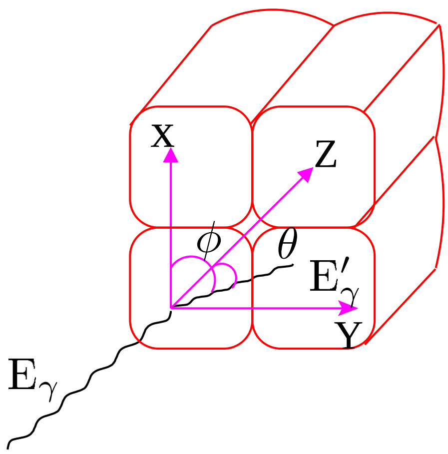

Figure 3.17: A schematic representation of a typical event of polarization measurement of a γ transition of energy E_γ in a clover detector as a Compton polarimeter. The Compton scattered energy E'_γ and the scattering angles θ and ϕ are shown as used in Eq. (3.34).

Here r_0 is the classical electron radius e^2/m_ec^2, where m_e and c is the rest mass of the electron and c is the velocity of light. It is quite clear from Eq. (3.34) that the Compton scattering cross-section is maximum at $\phi = 90^0$ i,e., perpendicular to the electric field vector ($\overrightarrow{\mathbf{E}}$) of the incident γ transitions. The HPGe clover detector have added advantage of measuring plane polarized γ transitions in the adjacent crystals to measure the polarity of the decaying γ- transitions according to below stated Eq.

$$P(\theta) = \frac{W(\theta, \phi = 0^0) - W(\theta, \phi = 90^0)}{W(\theta, \phi = 0^0) + W(\theta, \phi = 90^0)} \tag{3.35}$$

and the normalization is such that $P(\theta)$ lies between $-1 \leq P(\theta) \leq +1$. $P(\theta) = \pm 1$ correspond to complete polarization and $P(\theta) = 0$ for totally unpolarized γ-rays. Again $P(\theta) \geq 0$ correspond to electric ($P(\theta) \leq 0$, magnetic) type γ- transition. If the angular distribution coefficients A_2^{exp} and A_4^{exp} of the decaying γ- transitions are measured then the linear polarization of those transitions [22,23] can be measured with the help of following the Eqs.

$$P(90^0)_{cal} = \pm \frac{3A_2^{exp}H_2 - 7.5A_4^{exp}H_4}{2 - A_2^{exp} + 0.75A_4^{exp}} \tag{3.36}$$

where H_4= -1/6 and H_2 can be expressed in the following way

$$H_2(\lambda = 1, \lambda' = 2) = \frac{F_2(11) - 0.667\delta F_2(12) + \delta^2 F_2(22)}{F_2(11) + 2\delta F_2(12) + \delta^2 F_2(22)} \tag{3.37}$$

where +(-) is taken for transition without (with) a parity change and $F_2(\lambda, \lambda')$ coefficients can be taken from Ref. [16].

Following the prescription of Fagg and Hanna [24] the polarization for stretched E1, M1 (see Eq. [3.38]) and stretched E2, M2 transitions can be calculated using Eq. (3.39) for the arbitrary angle of the detector with respect to the incident beam direction.

$$P(\theta)_{E1,M1} = \pm\frac{3A_2^{exp}\sin^2\theta}{2 - A_2^{exp} + 3A_2^{exp}\cos^2\theta} \tag{3.38}$$

$$P(\theta)_{E2,M2} = \pm\frac{3A_2^{exp}\sin^2\theta + A_4^{exp}[\frac{35}{4}\cos^4\theta - 10\cos^4\theta + \frac{5}{4}]}{2 - A_2^{exp} + 3A_2^{exp}\cos^2\theta + A_4^{exp}[\frac{35}{4}\cos^4\theta - \frac{30}{4}\cos^2\theta + \frac{3}{4}]} \tag{3.39}$$

Here A_2^{exp} and A_4^{exp} are the angular distribution coefficients of the respective γ- rays and positive (or, negative) sign in the polarization [P(θ)] correspond to the electric (or, magnetic) type of the γ- transition.

In an array, decaying γ-ray's polarization is measured at a detector perpendicular to the beam direction to reduce the Doppler broadening effect. The polarization for the stretched E1, M1 (γ) or E2, M2 (γ) transition can be determined using following Eqs.

$$P(90^0)_{E1,M1} = \pm\frac{3A_2^{exp}}{2 - A_2^{exp}} \tag{3.40}$$

$$P(90^0)_{E2,M2} = \pm\frac{12A_2^{exp} + 5A_4^{exp}}{8 - 4A_2^{exp} + 3A_4^{exp}} \tag{3.41}$$

Integrated Polarization Measurement (IPDCO)

Experimentally the parity of a nuclear state is determined by Integrated Polarization Directional Correlation Ratio (IPDCO), following the prescription in Ref. [25, 26]. The

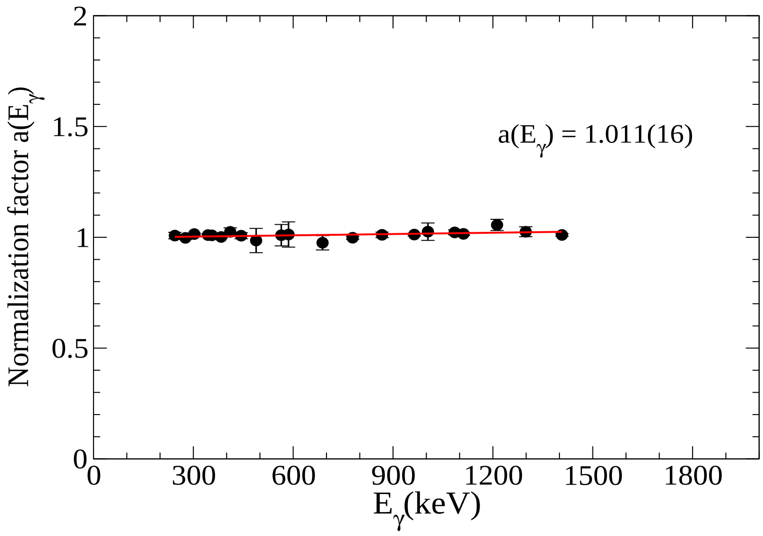

Figure 3.18: The asymmetry correction factor a(E_γ) at different γ energies from ^{133}Ba and ^{152}Eu sources. The solid line corresponding to the linear fit of the data.

data are sorted in two matrices, the first one contains data of horizontally ($N_{\parallel}$) Compton scattered events in the adjacent crystals of 90^0 detector on Y- axis whereas all γ events of all detectors except 90^0 on the X- axis. Similarly the other matrix contains vertically ($N_{\perp}$) Compton scattered events in the adjacent crystals of 90^0 detector on Y- axis and all γ events in all detectors except 90^0 on the X- axis. The asymmetry correction factor $a(E_\gamma)$ which describes the geometrical asymmetry of a detector (see Eq. (3.42)) is plotted as a function of energy (E_γ) in Figure. (3.42) using γ- transitions coming from the unpolarized radioactive sources ^{152}Eu and ^{133}Ba. The average value of this data points is 1.011(16) which is taken as asymmetry correction factor ($a(E_\gamma)$) for ^{195}Tl data as discussed in chapter-5.

$$a(E_\gamma) = \frac{N_{\perp}}{N_{\parallel}} \tag{3.42}$$

The IPDCO ratio is defined in the following way

$$\Delta_{IPDCO} = \frac{a(E_\gamma)N_\perp - N_\parallel}{a(E_\gamma)N_\perp + N_\parallel}, \tag{3.43}$$

Depending on this ratio ($\Delta_{IPDCO} = \pm 1$), the polarity of the γ- transitions are assigned as either electric (**E**) or magnetic (**M**) type. It is quite clear from Figure. (3.19) parallel ($N_\parallel$) counts are higher than perpendicular ($a(E_\gamma)*N_\perp$) counts for 458- keV γ- ray and opposite in case of 707- keV γ- ray of ^{195}Tl which makes them dominantly magnetic(**M**) and electric(**E**) in nature (details can be found in chapter-5)

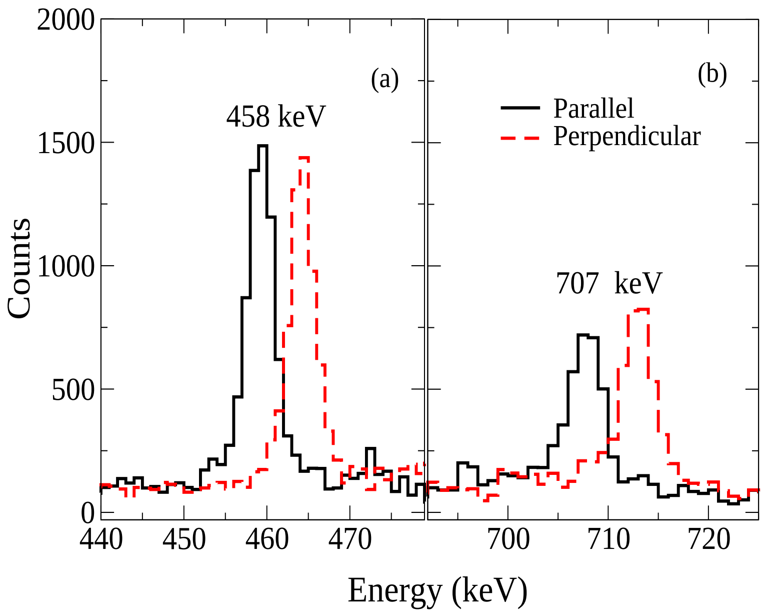

Figure 3.19: The perpendicular (dashed red) components (multiplied by a(E_γ)) and the parallel (solid black) scattered components of 458- and 707- keV gamma- rays are plotted here. For clarity perpendicular components are shifted with respect to parallel components here. The Δ_{IPDCO} for 458- and 707-keV gamma- rays of ^{195}Tl (discussed in the chapter-5) comes out to be negative and positive, respectively, representing them to be magnetic and electric in nature.

The polarity of the decaying γ- transitions are determined as

$$Q = \frac{\Delta_{IPDCO}}{P} \tag{3.44}$$

where the polarization sensitivity Q of a detector is dependent on energy of the incident γ- ray and geometry of the detector array which can be defined as

$$Q = \frac{\frac{d\sigma}{d\Omega}(\xi = 90^0, \phi = 90^0) - \frac{d\sigma}{d\Omega}(\xi = 90^0, \phi = 0^0)}{\frac{d\sigma}{d\Omega}(\xi = 90^0, \phi = 90^0) + \frac{d\sigma}{d\Omega}(\xi = 90^0, \phi = 0^0)} \tag{3.45}$$

here ξ is the angle between the beam direction and emitted γ-ray direction. Once the gated angular distribution coefficients A_2^{exp} and A_4^{exp} are determined one can deduce the polarization of the decaying stretched E2 gamma- transitions from Eq. (3.41). The corresponding Δ_{IPDCO} ratio for these gamma- transitions, helps to find out sensitivity (Q) of the array using Eq. (5.8) over a long energy range (see Table. 5.1).

Table 3.1: Energies (E_γ), gated angular distribution coefficients A_2^{exp} and A_4^{exp}, Polarization(P), IPDCO ratios (Δ_{IPDCO}) and sensitivity(Q) for gamma- rays populated in the experiment of ^{195}Tl discussed in chapter-5.

Energy(E_γ) (in keV)	A_2^{exp} (Err)	A_4^{exp} (Err)	$Polarization(P)$ (Err)	Δ_{IPDCO} (Err)	Sensitivity(Q) (Err)
492.8	0.20(13)	-0.11(19)	0.27(27)	0.19(5)	0.04(1)
575.7	0.19(8)	-0.05(12)	0.29(16)	0.14(6)	0.49(29)
672.2	0.30(4)	-0.08(6)	0.49(9)	0.10(5)	0.20(4)
707.5	0.29(2)	-0.07(3)	0.47(9)	0.16(3)	0.34(7)
734.5	0.26(4)	-0.09(6)	0.40(4)	0.11(7)	0.28(6)
821.6	0.32(3)	-0.07(5)	0.54(7)	0.10(3)	0.19(3)
852.3	0.42(2)	-0.48(3)	0.54(7)	0.11(5)	0.20(3)

The resulting polarization sensitivities are fitted using the function,

$$Q = (C + DE_\gamma)Q_0 \tag{3.46}$$

where Q_0 is called the polarization sensitivity for the ideal Compton polarimeter defined as,

$$Q_0 = \frac{1+\alpha}{1+\alpha+\alpha^2} \tag{3.47}$$

here $\alpha = E_\gamma/m_e c^2$, E_γ being the incident γ- ray energy and $m_e c^2$ is the electron rest mass energy.

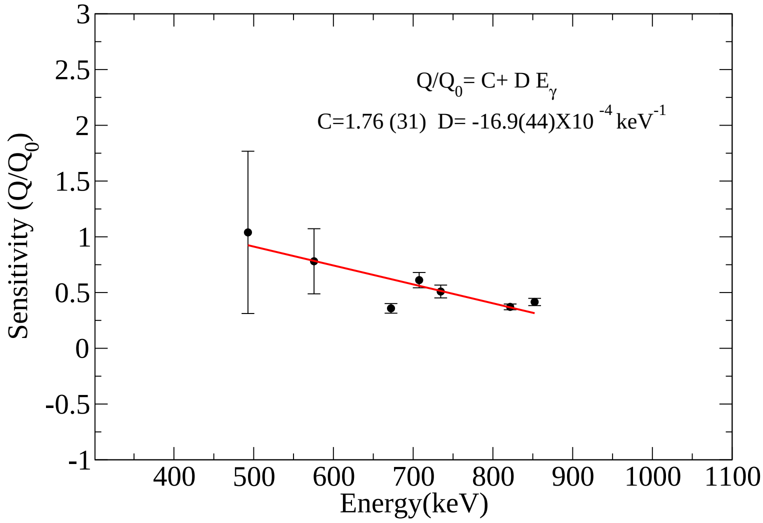

Figure 3.20: The measured polarization sensitivity for the clover detectors in the present experiment. The solid line is the fitted curve for the experimental data points.

The least-squares fitting of experimental polarization sensitivity $Q(E_\gamma)$ (see Figure. (3.20)) gave C = 1.76(31) and D = $-16.9(44)\times10^{-4}$ in keV^{-1}. The linear polarization (P) of several new γ- transitions can be determined from the measured Δ_{IPDCO} ratio with the help of the polarization sensitivity $Q(E_\gamma)$ of the INGA [23,26,27]. Thus, an unambiguous assignment of the electromagnetic character has been established for the γ- ray transitions of nuclei populated in the present reaction, will be discussed in the subsequent chapters.

3.0.21 Internal Conversion Coefficient

When the excited nucleus emits gamma rays, some of them knocks out the atomic shell electrons along with the emission of the characteristic X-ray of that atom. As a result of which the gamma- ray intensity appears to be some what smaller than what it should be. This process is quantified by internal conversion coefficient as

$$\alpha = \frac{I_e}{I_\gamma} = \frac{I_{\gamma tot} - I_\gamma}{I_\gamma} \tag{3.48}$$

where $I_{\gamma tot}$ and I_γ are the total and measured gamma ray intensity and α is the conversion coefficient.

$$\alpha = \alpha_K + \alpha_L + \alpha_M \tag{3.49}$$

For a γ- transition of energy E_γ(MeV), the internal conversion coefficient α_K for electric(E) and magnetic(M) type of transitions depends on the multipolarity(λ) and the element (Z) [19, 28] in the following way

$$\alpha_K(E\lambda) \propto Z^3 \frac{\lambda}{\lambda+1}[\frac{e^2}{4\pi\epsilon_0\hbar c}][\frac{2m_ec^2}{E_\gamma}]^{\lambda+5/2} \tag{3.50}$$

$$\alpha_K(M\lambda) \propto Z^3 [\frac{e^2}{4\pi\epsilon_0\hbar c}][\frac{2m_ec^2}{E_\gamma}]^{\lambda+3/2} \tag{3.51}$$

For mixed $(\pi\lambda + \pi'\lambda')$ multiploarity transitions the conversion coefficients can be deduced from the following Eq.

$$\alpha = \frac{\alpha(\pi\lambda) + \delta^2\alpha(\pi'\lambda')}{1+\delta^2} \tag{3.52}$$

where δ is the multipole mixing ratio of $\pi'\lambda'$ and $\pi\lambda$ gamma- transitions as specified in Eq. [3.28].

Therefore in order to build a level scheme, it is important to consider intensity balance of gamma- ray transitions at each energy level specially for higher multipolarity and low energy gamma- transitions in high Z material. The total intensity of a γ- transition in Eq. (3.48) can be rearranged in the following way

$$I_{\gamma tot} = I_{\gamma}(1 + \alpha) \tag{3.53}$$

3.0.22 Decay of an isomeric state

The decay of an isomeric state of a nucleus by γ- ray is a statistical phenomenon. It is governed by Batemen [30] Eq. If N is number of nuclei present in a isomeric state at time T, the number of nuclei dN decayed in time interval dT is proportional to the total number of nuclei N, therefore

$$dN = -\lambda N dT \tag{3.54}$$

where λ is the decay constant. By integrating the previous Eq. over observation time T we get the exponential law of radioactive decay in a form

$$N(T) = N_0 e^{-\lambda T} \tag{3.55}$$

where N_0 is the number of nuclei at time zero. The inverse of the decay constant is the mean lifetime

$$\tau = 1/\lambda \tag{3.56}$$

The half-life $T_{1/2}$ determines the time interval needed for the half of the nuclei to decay, and can be expressed in a form

$$T_{1/2} = \tau ln2 = 0.693\tau \tag{3.57}$$

The electromagnetic transition probability from initial state of spin I_i to a final state I_f by emitting γ- ray of multipolarity l carrying angular momentum L is given by

$$T_{fi}(lL) = \frac{ln2}{T^{\gamma L}_{1/2}} = \frac{8\pi(L+1)}{\hbar L[(2L+1)!!]^2}[\frac{E_\gamma}{\hbar c}]^{2L+1}B(lL; I_i \rightarrow I_f) \tag{3.58}$$

where, B(lL) is the reduced transition probability of a γ- ray of branching ratio (BR) can be expressed in terms of Weisskopf unit [13] as follows

$$B(EL) = \frac{(ln2)L[(2L+1)!!]^2\hbar \times BR}{1.2^{2L}(L+1)A^{2L/3}T^{\gamma L}_{1/2}(1+\alpha)[e^2(fm)^2]}(\frac{L+3}{3})^2[\frac{\hbar c}{E_\gamma}]^{2L+1}[W.u] \tag{3.59}$$

$$B(ML) = \frac{(ln2)L[(2L+1)!!]^2\hbar \times BR}{80(1.2)^{2L}(L+1)A^{(2L-2)/3}T^{\gamma L}_{1/2}(1+\alpha)[\mu_N^2(fm)^{(2L-2)}]}(\frac{L+3}{3})^2[\frac{\hbar c}{E_\gamma}]^{2L+1}[W.u] \tag{3.60}$$

The measured transition strengths for the single particle states $\sim$ 1 W.u. whereas a significant departures from these values are observed, compared to the Weisskopf estimate, when the nucleus exhibits collective behaviour.

Table 3.2: Transition probabilities T ($\sec^{-1}$) expressed B(EL) [$e^2(fm)^{2l}$] and B(ML) [$\mu_N^2(\mathrm{fm})^{2l-2}$] and Weisskopf units $B_{sp}(Ml)$ expressed in [$e^2(fm)^{2l}$] and [$\mu_N^2(\mathrm{fm})^{2l-2}$]. The energies E_γ are measured in MeV.

lL	T(lL) $\sec^{-1}$	$B_{sp}(lL)$
E1	T(E1)=1.587 X $10^{15}E^3$B(E1)	B_{sp}(E1)=6.446 X 10^{-2} $A^{2/3}$
M1	T(M1)=1.779 X $10^{13}E^3$B(M1)	B_{sp}(M1)=1.790
E2	T(E2)=1.223 X $10^{9}E^5$B(E2)	B_{sp}(E2)=5.940 X 10^{-2} $A^{4/3}$
M2	T(M2)=1.371 X $10^{7}E^5$B(M2)	B_{sp}(M2)=1.650 $A^{2/3}$
E3	T(E3)=5.698 X $10^{2}E^7$B(E3)	B_{sp}(E3)=5.940 X 10^{-2} A^2
M3	T(M3)=6.387 E^7B(M3)	B_{sp}(M3)=1.650 $A^{4/3}$

In Table. 3.2 Weisskopf single-particle estimates [13] for transition probabilities T_{fi} together with the reduced transition probabilities BW are listed for $l \leq 3$ γ-ray transitions.

Quantities Required for Experimental Data Interpretation

There are various quantities like rotational frequency (ω), moment of inertia (I), kinetic angular momentum (j^1), dynamic angular momentum (j^2), aligned angular momentum (i_x), energy staggering [S(I)], Routhian energy etc. required for the interpretation of experimental data which are deduced from the level scheme.

I. The information about the contribution of single particle excited state of a nucleus is extracted by subtracting the rigid rotation reference (E_{RLD}) from the experimentally observed energy (E_x) as a function of spin (I). This reference energy is determined, considering the nucleus as a spherical liquid drop [31] of radius (r_0=1.2$A^{1/3}$ fm) as follows

$$E_{RLD} = \frac{I(I+1)}{2\jmath_{rig}}, \text{ where } \frac{1}{2\jmath_{rig}} = 32.32A^{-5/3}MeV/\hbar^2 \tag{3.61}$$

II. If an axially deformed nucleus rotates about an axis (x-axis) perpendicular to its symmetry axis (z-axis) then the projection of the total angular momentum on the rotation axis (x-) can be expressed as

$$I_x = \sqrt{I(I+1) - K^2} = \sqrt{(I+\frac{1}{2})^2 - K^2} \tag{3.62}$$

where I_x and K are the projection of the total angular momentum about the rotation axis and symmetry axis of the nucleus respectively. The rotational frequency of a particular nuclear state [32] can be expressed in terms of the following canonical equation

$$\omega(I) = \frac{dE(I)}{dI_x} = \frac{E(I+1) - E(I-1)}{I_x(I+1) - I_x(I-1)} = \frac{E_\gamma}{2} \text{ for } I >> K \tag{3.63}$$

and the crucial information regarding single particle contribution of alignment angular momentum i_x (see Eq. [3.64]) and Routhian from Eq. [3.65]

$$i_x = I_x - I_{REF} = I_x - (\Im_0 + \omega^2\Im_1)\omega \tag{3.64}$$

$$e' = E'(\omega) - E'_{REF}(\omega) \tag{3.65}$$

where

$$E'(\omega) = (1/2)[E(I+1) + E(I-1)] - \omega(I)I_x(I) \tag{3.66}$$

$$E'_{REF} = -\int I_{REF} d\omega = -\frac{1}{2}\omega^2\Im_0 - \frac{1}{4}\omega^4\Im_1 + \frac{1}{8}\hbar^2/\Im_0 \tag{3.67}$$

here $\Im_0$ and $\Im_1$ are the Harris parameter [33]. This experimentally determined single particle Routhian can be directly compared with the values obtained from the theoretical calculation.

III. The two moments of inertia i. e., kinetic moment of inertia (j^1) and dynamic moment of inertia (j^2) gives the information on whether any structural change in a nucleus happens at a particular spin or frequency. The kinetic moment of inertia (j^1) and dynamic moment of inertia (j^2) of a nucleus can be defined as follows

$$j^1(\omega) = \frac{I_x}{\omega} \tag{3.68}$$

$$j^2(\omega) = \frac{dI_x}{d\omega} = \Im_0 + 3\Im_1\omega^2 \tag{3.69}$$

$$j^2(I+1) = \frac{I_x(I+2) - I_x(I)}{\omega(I+2) - \omega(I)} \approx \frac{4}{\Delta E_\gamma}\hbar^2 MeV^{-1} \text{ for } \Delta\text{I=2 band and I >> K} \tag{3.70}$$

IV. The B(M1)/B(E2) ratio is extremely sensitive to the quasi-particle configuration involved as it conveys the message of relative γ transition probability from one nuclear state to another [34] and is expressed as.

$$B(M1)/B(E2) = 0.697\frac{E_{2\gamma}^5}{E_{1\gamma}^3}\frac{1}{1+\delta^2}\frac{I_{\gamma_1}(\Delta I = 1)}{I_{\gamma_2}(\Delta I = 2)} \tag{3.71}$$

where δ is the mixing ratio for M1+E2 (ΔI=1) γ transition, $E_{2\gamma}$ and $E_{1\gamma}$ are the energy of the E2 (ΔI=2) and M1 (ΔI=1) γ transitions respectively. Whereas I_{γ_1} and I_{γ_2} are intensity of M1 and E2 γ- transitions respectively.

Bibliography

[1] P. Regan Post Graduate Nuclear Experimental Techniques (4NET) Course Notes, University of Surrey (2003).

[2] R. Bass et al., Nucl. Inst. Meth. **A 231**, 45 (1974).

[3] W.R. Leo Techniques for Nuclear and Particle Physics Experiment, Springer Verlag Berlin Heidelberg (1987).

[4] Experiments in Nuclear Science, High-Resolution Gamma-Ray Spectroscopy published by EG and G ORTEC.

[5] G. Duchene et al., Nucl. Inst. Meth. Phys. Res. **A 432**, 90 (1999).

[6] S. Rajbanshi Ph.D. thesis, University of Calcutta, (2016).

[7] H. Tan et al., in Nuclear Science Symposium Conference Record 2008 (IEEE, Washington,DC, 2008),**p. 3196**.

[8] R. Palit et al., Nucl. Inst. Meth. **A 680**, 90 (2012).

[9] D.C. Radford., Nucl. Inst. Meth. Phys. Res., Sect. **A 361**, 297 (1995).

[10] M. Leino et al., Nucl. Inst. Meth. **B 99**, 653 (1995).

[11] A. Ghiorso et al., Nucl. Inst. Meth. **A 269**, 192 (1988).

[12] N. Madhavan et al., Pramana **57**, 317 (2010).

[13] J.M. Blatt and V.F. Weisskopf. Theoretical Nuclear Physics. Wiley, New York 1952.

[14] R.M. Diamond et al., Phys. Rev. Lett. **16**, 1205 (1966).

[15] J.O. Newton et al., Nucl. Phys. **A 95**, 357 (1967).

[16] T. Yamazaki: "Tables of Coefficients for Angular Distribution of Gamma Rays from Alingned Nuclei", Nucl. Data. **3**, 1 (1967).

[17] E.D. Mateosian et. al., Atomic Data and Nucl. Data. Tables **13**, 391 (1974).

[18] A. Krämer-Flecken et al., Nucl. Inst. Meth. Phys. Res. **A 275**, 333 (1989).

[19] K.S. Krane et al., Nucl. Data Tables **11**, 351 (1973).

[20] E.S. Macias et al., Computer Physics Communications **11**, 7593 (1976).

[21] O. Klein and Y. Nishina. Z. Physik **52**, 853 (1929).

[22] J.K. Deng et al., Nucl. Inst. Meth. Phys. Res. **A 317**, 242 (1992).

[23] R. Palit et al., Pramana **54**, 347 (2000).

[24] L.W. Fagg and S. S. Hanna. Rev. Mod. Phys. **31**, 711 (1959).

[25] K. Starosta et al., Nucl. Inst. Meth. Phys. Res. **A 423**, 16 (1999).

[26] Ch. Droste et al., Nucl. Inst. Meth. Phys. Res. **A 378**, 518 (1996).

[27] J.S. Kim et al., Phys. Rev. **C 12**, 499 (1975).

[28] T. Kibdi et al.,Nucl. Phys. **A 589**, 202 (2008).

[29] T. Kibdi et. al., Nucl. Instr. and Meth. **A 589**, 202 (2008); http://bricc.anu.edu.au/index.php.

[30] H. Bateman. Proc. Cambridge Philos. Soc, vol. **15**, 423 (1910).

[31] A.A. Afanasjev et al., Physics Reports **322**, 1 (1999).

[32] R. Bengtsson and S. Frauendorf, Nucl. Phys. **A 327**, 139 (1979).

[33] S.M. Harris Physics Rev. **138**, B509 (1965).

[34] Amita and A.K. Jain, Atomic Data and Nucl. Data. Tables **74**, 283 (2000).

Chapter 4

Study of High Spin Isomer in Bi Isotopes

4.1 Introduction

Investigation of high spin isomers and their decay is one of the most interesting aspects of nuclear structure study. For Bismuth nuclei ($Z = 83$) in the A $\sim$ 190 region, the proton Fermi level lies just above the $Z = 82$ shell closure and the neutron Fermi level lies below the $N = 126$ shell closure. Due to this, the heavier isotopes of Bismuth, having neutron number close to 126, are near-spherical and the low-lying excited states in odd-A isotopes are well understood with the odd-proton in the shell-model states above $Z = 82$ [1]. However, as the neutron number decreases, deformation sets-in for the lighter Bismuth isotopes with the onset of deformation at $N = 112$ isotope ^{195}Bi in which a rotational band based on the proton $i_{13/2}$ orbital has been observed [2], similar to those observed in ^{191,193}Bi [3].

Several high-spin isomeric states have been reported in the Bismuth nuclei in $A = 190$ region which occur due to the presence of high-j proton and neutron orbitals near the Fermi level for these nuclei [3–8]. The ground state of all the Bi isotopes is built on odd-proton in the $h_{9/2}$ orbital. A $13/2^+$ isomeric state, corresponding to the odd-proton in the $i_{13/2}$ orbital, has also been observed in all Bismuth isotopes and its excitation energy varies from about 250 keV in ^{187}Bi to about 1.6 MeV in ^{209}Bi. The high-spin isomers are interpreted as 3 quasi-particle states arising from the coupling of the odd-proton in either $h_{9/2}$ or $i_{13/2}$ orbital with the two-neutron states in the neighbouring even-even Pb core. The coupling of $h_{9/2}$ with the 7^- and 9^- states in Pb nuclei gives rise to $21/2^+$ to $27/2^+$ states in odd-A Bi isotopes [5,6], and in some cases, they are the isomeric states. Coupling of the 12^+ state, arising from the $\nu i_{13/2}^{-2}$ configuration, with the $h_{9/2}$ proton orbital leads to an isomeric $29/2^-$ state in odd-A Bi isotopes, the half-life of which varies from 3 μs in ^{193}Bi [3] to 124 ns in ^{201}Bi [6]. The $31/2^-$ three-quasi-particle states, observed only in the heavier isotopes ($A > 195$), were interpreted as the multiplet of the same configuration. A second $31/2^-$ state in ^{197}Bi has been interpreted as the coupling of the $\pi i_{13/2}$ orbital with the $\nu[(f_{5/2}^{-1} f_{7/2}^{-1}) i_{13/2}^{-1}]_{9^-}$ configuration [5].

In ^{195}Bi, the spin and parity of the highest known isomer is $29/2^-$ having a half-life of 750(50) ns [4]. The excitation energy of this isomer is tentatively assigned as 2396 keV [2]. The highest known excited state in this nucleus is a $(23/2^+)$ state at 2.9 MeV, which was assigned as belonging to the band built on the $13/2^+$ isomer [2]. The level scheme of ^{195}Bi is quite simple compared to its immediate neighbours ^{193,197}Bi [3,5,8,9]. Two other three-quasi particle states, $23/2^+$ and $25/2^{(-)}$ are also known in this nucleus at the excitation energies of 2195 keV and 2310 keV, respectively. No other high-spin states are known in

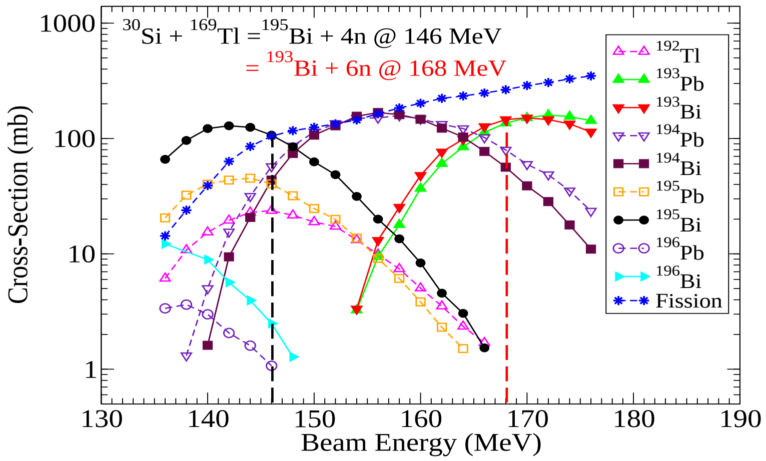

Figure 4.1: Excitation function drawn using PACE-IV based on monte carlo calculation. The cross-section for ^{193}Bi and ^{195}Bi maximizes for the fusion evaporation reaction with ^{30}Si beam on ^{169}Tl target at 168 and 146 MeV respectively.

this nucleus. The $27/2^+$ and the $31/2^-$ isomers have not been found in Bi isotopes lighter than $A = 197$. Recently, a $29/2^+$ isomer has been reported in ^{193}Bi at an excitation energy of 2350 keV [1] with a half-life of 84.4(6) μs. Therefore, it is interesting to look for other high-spin isomer(s) in the neighbouring isotope ^{195}Bi.

4.2 Experimental Setup

The experiment was performed at the 15-UD Pelletron-superconducting-LINAC facility at IUAC, New Delhi using the gas-filled mode of Hybrid Recoil mass Analyzer (HYRA). The excited states were populated using the fusion-evaporation reaction ^{169}Tm(^{30}Si, 4n)^{195}Bi with an average beam current $\sim$ 0.5 pna.

The beam was selected for the present experiments based on the excitation function (see Figure. (4.1)) based on PACE-IV calculation where the yield for ^{195}Bi and ^{193}Bi maximizes. For ^{195}Bi the beam energy was selected to be 146 MeV over a period of 43 hour. In the beginning a short run of 13 hour was taken with 168 MeV of beam energy at the target to produce ^{193}Bi. This run was mainly to optimize the setup and to ensure that the method works in the new HYRA setup by reproducing the half-life of a known 3-μs isomer in ^{193}Bi and identifying its known decay γ-rays. A self supporting (mono-isotopic) target of ^{169}Tm (0.8 mg/cm^2) was used for the reaction. The gas-filled (He gas at 0.15 Torr) HYRA [11] was used to separate the evaporation residues (ER) from the beam-like particles and fission products, and the ERs were carried to the focal plane. The time of flight for the ERs was estimated to be 1.6 μs. There was no foil between the target and the entrance of HYRA; instead a Ni foil of thickness 1.3 mg/cm^2 was used up-stream of the target position which separated the He gas from the beam-line vacuum. The beam energy degrades by $\sim$ 10 MeV in this foil before interacting with the target, which was taken into account in choosing the beam energy.

The focal plane chamber consists of a Multi-wire proportional counter (MWPC) (about 150 mm in X and 50 mm in Y) and three Si-pad detectors (each of size 50 mm x 50 mm) for the identification of ERs. The ERs were implanted in the Si-pad detectors. One clover HPGe detector was placed at the end of the focal plane chamber using a re-entrant cup for the detection of the decay γ-rays. The distance between the clover detector and the Si-pad was about 5.5 cm. The re-entrant cup (diameter 8 inch) had a thin ($\sim$ 1.5 mm) stainless-steel window to reduce the attenuation of the low-energy γ-rays and X-rays. To detect the prompt γ-rays, another clover HPGe detector was placed about 27 cm away from the target at an angle of $\sim 135^o$ with respect to the beam direction. However, this target-site clover was used only for a part of the experiment towards the end of the run.

Time and pulse height information of each γ- ray detected in the four crystals of the focal plane clover detector and the pulse height information of the γ- rays detected in the target-clover detector were stored event-by-event using a CAMAC-based data acquisition system, "*CANDLE*" [12]. The "master" trigger, 10 μs wide, was generated using coincidence between the MWPC and either of the Si-pad detector signals. Three time-differences were also recorded using time-to-amplitude converters (TAC). These are (i) between the target-clover detector and the Si-pad detector (ΔT_1) which gives the time-of-flight of the recoils from the target position to the focal plane; here the TAC "start" signal was given from the Si-pad detector and the "stop" signal was obtained from the 'OR' of all four crystals of the target-clover delayed by 2.5 μs, (ii) between the MWPC and the focal-plane clover ('OR' of all four crystals) detector (ΔT_2) which is used to obtain the half-life of the isomers and (iii) between the "master" and the individual crystals of the focal-plane clover (ΔT_3^i, $i = 1 - 4$, for the 4 crystals of the clover) detector which are used to put 'prompt' time gate between the γ-rays for $\gamma - \gamma$ correlation between the crystals of the focal-plane clover detector. The clover detectors were calibrated for γ-ray energies and relative efficiencies by using ^{133}Ba and ^{152}Eu radioactive sources. The TACs were also time-calibrated using fixed delay.

4.3 Data Analysis and Results

The data were analysed using the "offline" version of the "*CANDLE*" software. The focal plane clover detector [13] add-back spectrum as shown in Figure. (4.2) were mostly dominated by background γ- lines. The gamma- rays belonging to ^{193}Bi and ^{195}Bi isotopes are mostly buried inside this huge background. To identify the gamma- rays belonging

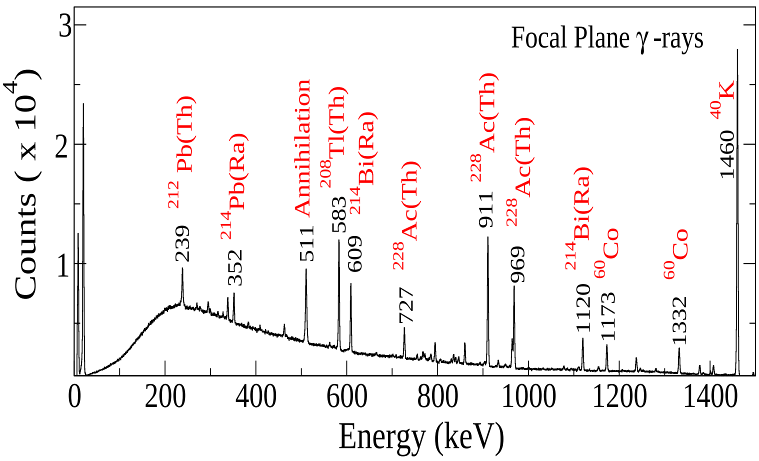

Figure 4.2: Raw gamma-ray spectrum dominated by background line observed at the focal plane clover detector.

to these nuclei, the add-back spectrum of the focal plane clover detector was gated by the evaporation residues reaching the focal plane of HYRA. The evaporation residues were identified from a two-dimensional plot of the energy signal from the central Si-pad detector (Si_Mid), which has almost all the counts out of the three Si-pad detectors, and MWPC_Cathode, the cathode signal of the MWPC. The evaporation residue for ^{193}Bi and ^{195}Bi were identified as the events inside the rectangular box in Figure. (4.3) and Figure. (4.4) at the focal plane.

The time difference spectrum ΔT_1 is shown in Figure. (4.5) which gives the measured time-of-flight of the recoils from the target to the focal plane. Because of the delayed (by 2.5 μs) stop, the real time-of-flight is from right to left on the X-axis in this spectrum and the same are labelled at the top. From the peak position in this spectrum, we obtain an average time-of-flight of 1.53(9) μs. The uncertainty is obtained from the fitted FWHM of the peak. This measured value of time-of-flight matches well with the estimated time-of-flight of $\sim$ 1.6 μs obtained from the calculated kinetic energy of the recoils and the flight

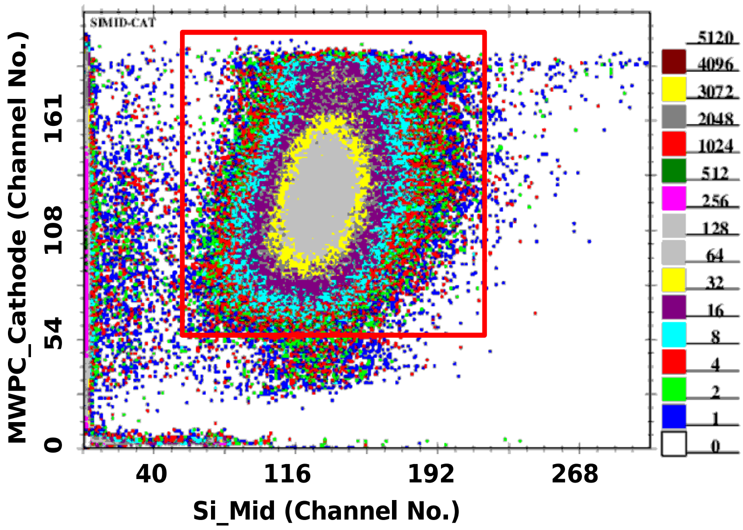

Figure 4.3: Two-dimensional plot of middle Si-pad detector (Si_Mid) and the cathode signal of the MWPC (MWPC_Cathode) at the focal plane of HYRA for ^{193}Bi. The evaporation residues are identified inside the rectangular area.

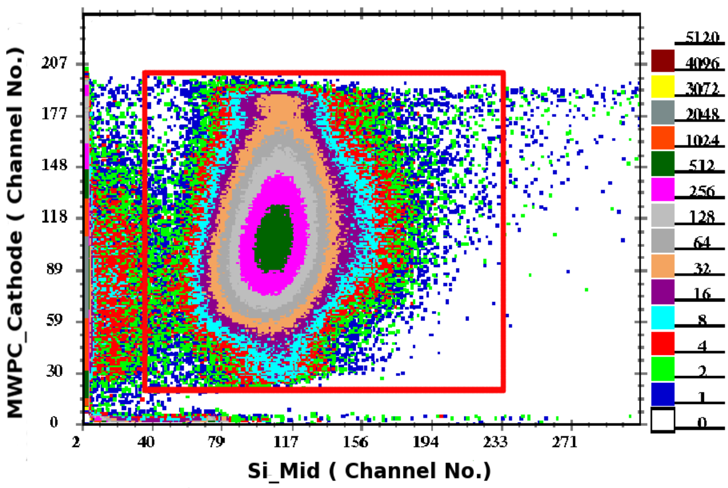

Figure 4.4: Two-dimensional plot of middle Si-pad detector (Si_Mid) and the cathode signal of the MWPC (MWPC_Cathode) at the focal plane of HYRA. The evaporation residues are identified inside the rectangular area for ^{195}Bi.

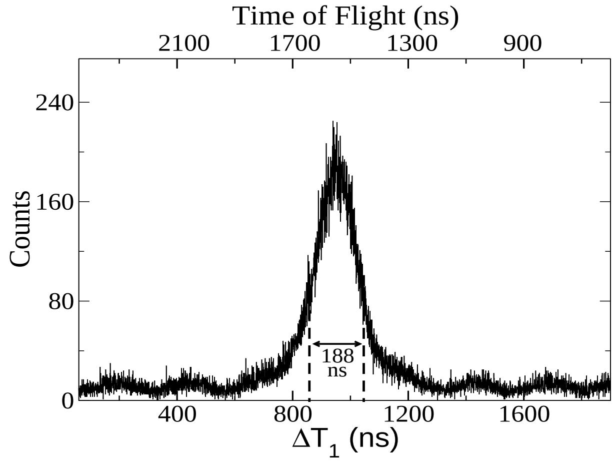

Figure 4.5: TAC spectrum showing the time difference between the signal from the ER detected in the Si-pad detector and the delayed (by 2.5 μs) signal from the target-clover. The real time of flight of the ER is labelled at the top. The FWHM of the peak is shown between the dotted lines.

path. The time-of-flight of the recoils indicates that isomers with half-lives shorter than about a μs will mostly decay before reaching the focal plane. Therefore, the ER gated γ-rays observed in Figure. (4.10)(a,b) are following the decay of isomers on the order of a μs or higher.

The γ-ray energy gated time difference spectrum $\Delta T_2 = 10\mu$s was used to obtain the half-life of an isomer. For this, a two-dimensional matrix between E_γ and ΔT_2 is created, where E_γ is the "addback" energy of the γ- ray detected at the focal-plane clover detector. The energy-gated time spectra are obtained by projecting on the ΔT_2 axis with a gate on a known γ- ray of a nucleus on the E_γ axis in this matrix. The fitted slope of the projected time spectrum gives the lifetime of the isomer corresponding to the gating transition. To increase the statistics, the sum spectrum with gate put on several transitions decaying from the same isomer have been used.

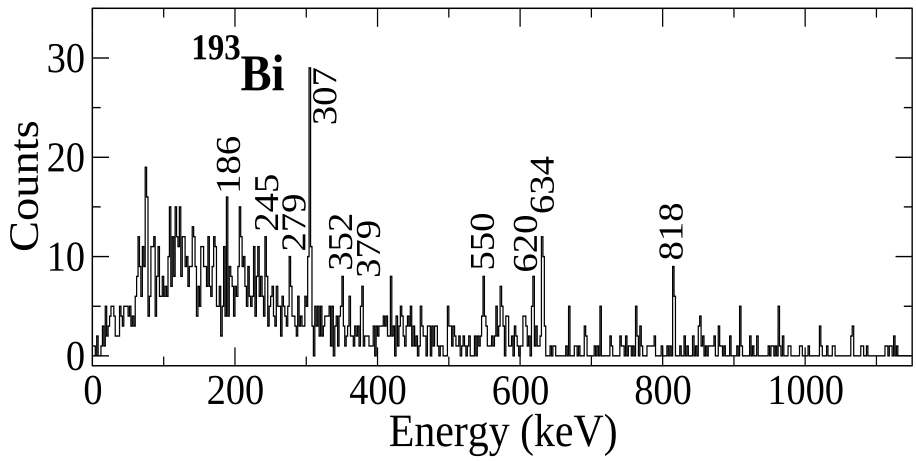

Figure 4.6: ER-gated "addback" γ-ray spectrum from the focal-plane clover detector for ^{193}Bi using a time window of 10 μs after the implantation of the recoils in the focal plane.

To check for the coincidence relation between the decay γ-rays, a coincidence $E_\gamma - E_\gamma$ matrix was also created from the focal plane clover detector by treating the four crystals of the clover as four different detectors. A coincidence time window of 200 ns was put using the ΔT_3^i $(i = 1 - 4)$ time spectra. The number of counts in the gated spectra obtained from this matrix was very limited but it gives important information as discussed later.

4.3.1 ^{193}Bi

The raw add-back spectrum as shown in Figure. (4.2) mostly dominated by back ground lines which gets much cleaner when we put a gate on evaporation residues with a time window of $\Delta T_2 = 10\,\mu$s, after the implantation of the recoils in the focal plane. In the ER-gated γ-ray spectrum shown in Figure. (4.6) consist of 186-, 245-, 279-, 352-, 379-, 620-, 634-and 818- keV gamma- rays belonging to ^{193}Bi (see partial level scheme in Figure.(4.7)). Among these 186- and 279- keV gamma- rays have been identified for the first time in the present study which is also later confirmed by the authors [10].

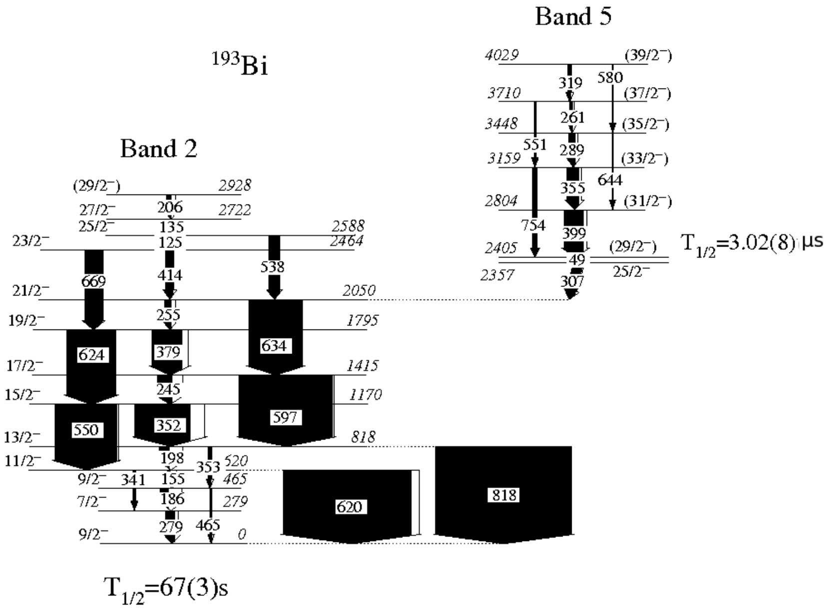

Figure 4.7: Partial level scheme of ^{193}Bi with 3.02(8) μs isomer (J^{π}=(29/2^{-})) predominantly decaying through 307 keV γ- ray to the lower lying levels taken from the article [10].

As mentioned earlier, in order to validate this well known isomer decay tagging method using our set up which is used for the first time in such studies, we have verified the 3.02(8) μs known isomer at 2405 keV excitation energy in ^{193}Bi. For this, a two-dimensional matrix between E_{γ} and ΔT_2 was created for ^{193}Bi (see Figure. (4.8)), where E_{γ} is the "addback" energy of the γ- ray detected at the focal-plane clover detector. The energy-gated time spectra are obtained by projecting on the ΔT_2 axis with a gate on a known γ- ray of a nucleus on the E_{γ} axis in this matrix. The above mentioned isomer in ^{193}Bi is de-excited via 49 keV followed by 307 keV γ- rays as shown in Figure. (4.7). The time spectrum, projected from the E_{γ} Vs. ΔT_2 matrix with gate on 307-keV transition in ^{193}Bi and its fit is shown in Figure. (4.9). From the fitting, we obtain $T_{1/2}$ = 3.0(6) μs as the half-life of the isomer, which is in very good agreement with the reported value [3].

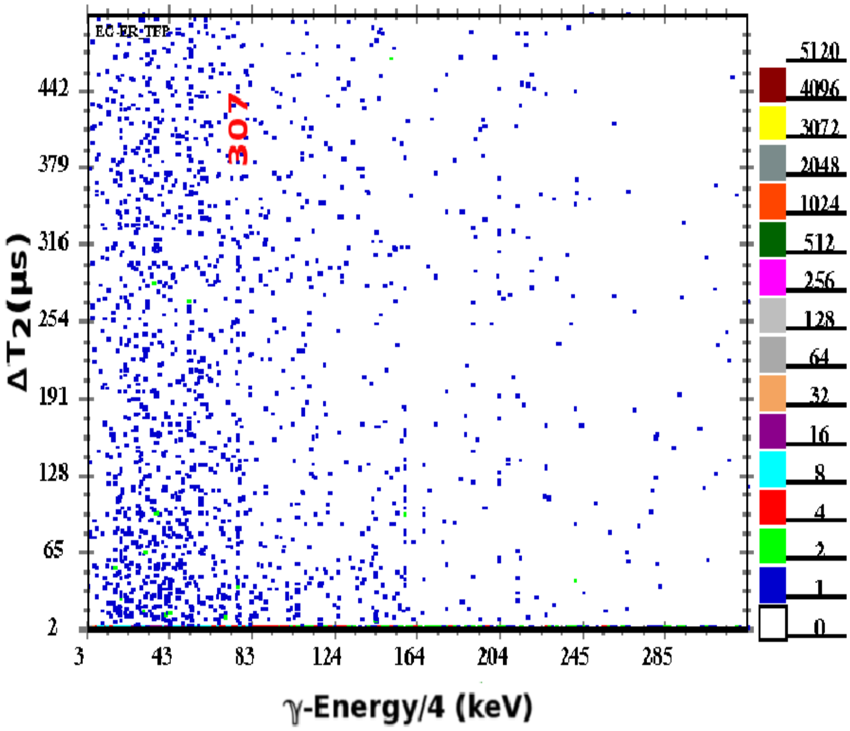

Figure 4.8: A 2D spectrum between $\triangle T_2$ and ER gated γ energies of ^{193}Bi at the focal plane clover detector used to determine the life time of the states by putting gate on 307-keV gamma ray and projecting its counts on time axis.

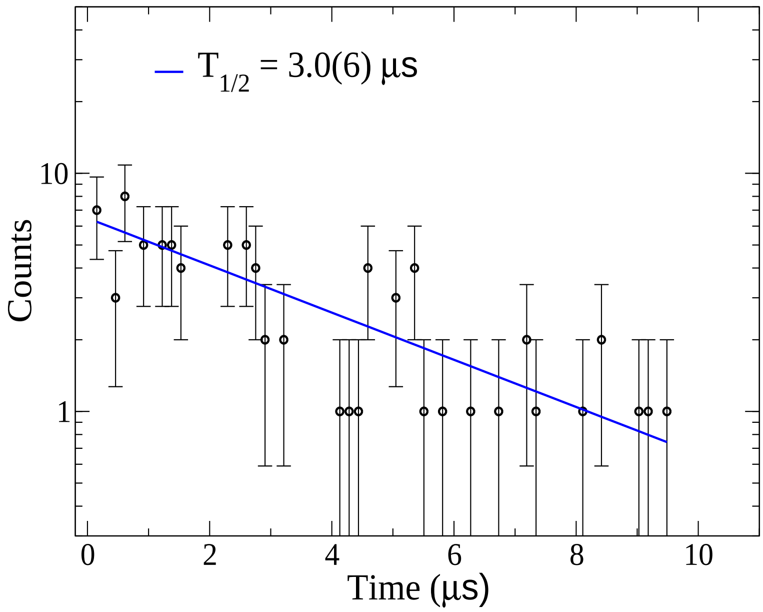

Figure 4.9: Time spectrum gated by the 307-keV transition in ^{193}Bi and its fit (blue line).

4.3.2 ^{195}Bi

All the known transitions in ^{195}Bi [2] are clearly observed in Figure. (4.10) and the peaks are marked with their energies. These are discussed later in detail. Other isomeric decays from Pb and Tl isotopes, which were also produced with smaller cross-sections, are marked by # in this spectrum.

The data were also analysed by treating the crystals of the clover detector as separate detectors to get coincidence relation between the decay γ-rays. In this analysis, an ER-gated $\gamma - \gamma$ matrix was obtained from the photo-peak events in the individual crystals of the clover detector with no "addback". A coincidence time window of 200 ns was put using the ΔT_3^i $(i = 1 - 4)$ time spectra. Because of the triple coincidence demand of ER-γ-γ, the number of counts is limited but this gives true correlations with very low background.

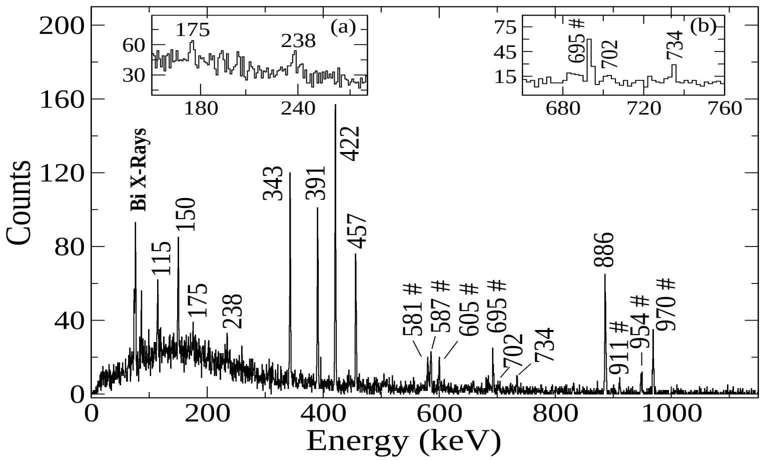

Figure 4.10: ER-gated “addback” γ-ray spectrum from the focal-plane clover detector for ^{195}Bi using a time window of 10 μs after the implantation of the recoils in the focal plane. The γ-ray peaks from the other ERs are indicated by #. The energy regions of the new γ-rays, 175-keV, 238-keV and 702 keV, assigned to the decay of a new isomer in ^{195}Bi are expanded and shown in the insets (a) and (b).

A higher-lying 750 (50) ns isomer was reported in ^{195}Bi by Lönnroth et al. [4] with $J^{\pi} = (29/2)^{-}$. Tentative excitation energy of 2396 keV and decay path of this isomer was reported recently by Pai et al. [2]. In that study, the band built on the $13/2^{+}$ state was extended up to 2923 keV of excitation energy but no new isomer was reported above the 750-ns isomer. A prompt γ-ray of energy 457 keV was known to decay from the highest observed level (2923 keV) in this nucleus.

As mentioned before, all known delayed γ-rays in ^{195}Bi have been observed in Figure. (4.10). The energy, intensity and the placement of the γ-rays in ^{195}Bi observed in this work are given in Table.-[4.1]. The observation of the 457-keV γ-ray in this delayed spectrum at the focal plane clearly indicates that there is a new high-lying isomer which feeds the level at 2923 keV from which the 457-keV γ-ray decays. In the prompt spectroscopy experiment in Ref. [2], the 457 keV transition was at least a factor of 5 weaker than the 343 keV transition. However, in the decay spectrum of the present work, these two γ rays are observed to be of comparable (within about a factor of 1.5) intensity. This indicates a stronger decay path of a higher-lying isomer via the 457-keV γ ray. Because of this stronger decay path of the isomer, the relative intensity of the 422-keV transition, which is doubly placed in the level scheme [2], has been found to be larger in this study (see Figure. (4.10)) compared to that in the prompt spectroscopy in Ref. [2].

The 115- and 150-keV transitions which decay from the 750-ns isomer are also observed clearly with similar intensity to that of 457-keV. The time-of-flight of the ERs, from the target to the focal plane, was about 1.5 μs in the present experiment which is equivalent to two half-lives of the 750-ns isomer and about one half-life of the new, high-lying isomer ($T_{1/2} = 1.6(1)$ μs). The population ratio of the two isomeric states has been found to be

Table 4.1: γ-ray energies (E_γ), relative intensities (I_γ), and assigned type of the γ rays in ^{195}Bi. The energies of initial states (E_i), spins and parities of initial (J_i^π) and final (J_f^π) states are also given.

E_γ (in keV)	E_i (in keV)	$J_i^\pi \rightarrow J_f^\pi$	I_γ	Eλ / Mλ
114.9(2)	2309.5	$\frac{25}{2}^{(-)} \rightarrow \frac{23}{2}^{+}$	7.9(17)	(E1)
150.2(2)	2194.6	$\frac{23}{2}^{+} \rightarrow \frac{19}{2}^{+}$	8.9(13)	E2
175.0(4)	3098.0	$(\frac{27}{2}^{+}) \rightarrow (\frac{23}{2}^{+})$	9.2(26)	(E2)
238.0(4)	3336.0	$(\frac{31}{2}^{-}) \rightarrow (\frac{27}{2}^{+})$	4.4(18)	(M2)
343.4(1)	1230.6	$\frac{15}{2}^{+} \rightarrow \frac{13}{2}^{+}$	29.2(22)	M1+E2
391.3(1)	1621.6	$\frac{17}{2}^{+} \rightarrow \frac{15}{2}^{+}$	27.9(18)	M1+E2
421.6(1)	2465.6	$\frac{21}{2}^{+} \rightarrow \frac{19}{2}^{+}$	44.3(22) [1]	(M1+E2)
421.6(1)	2044.9	$\frac{19}{2}^{+} \rightarrow \frac{17}{2}^{+}$		(M1+E2)
457.4(1)	2923.0	$\frac{23}{2}^{+} \rightarrow \frac{21}{2}^{+}$	18.8(22)	(M1+E2)
702.0(4)	3098.0	$(\frac{27}{2}^{+}) \rightarrow (\frac{29}{2}^{-})$	3.1(13)	(E1)
734.7(3)	1621.6	$\frac{17}{2}^{+} \rightarrow \frac{13}{2}^{+}$	5.3(9)	(E2)
886.7(1)	886.7	$\frac{13}{2}^{+} \rightarrow \frac{9}{2}^{-}$	34.9(22)	M2

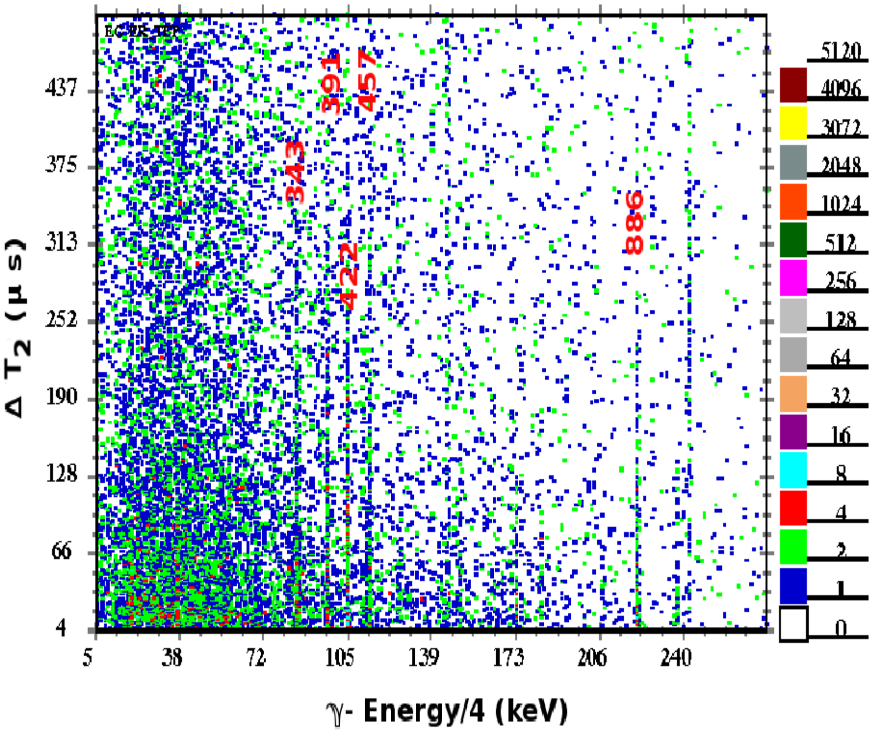

Figure 4.11: A 2D spectrum between $\triangle T_2$ and ER gated γ energies of ^{195}Bi at the focal plane clover detector used to determine the life time of the states by putting gate on 886-, 457-, 422-, 391-, 343-, 238- and 175-keV gamma rays and projecting its counts on time axis.

about 1.1 from the statistical model calculations using the $PACE$ code [14, 15] for the fusion evaporation reaction in the present experiment. Using this, the relative intensities of the decay γ-rays from the two isomers, e.g., 150-keV and 457-keV, can be estimated. Relatively larger intensity, compared to the estimated one, observed for the 150-keV γ-ray indicates that the lower lying 750-ns isomer is partly fed by the new, high-lying isomer. This gives two decay paths of the new isomer, one via 457-keV transition and another via the known 750-ns isomer.

In order to measure the life of this isomer a two-dimensional matrix between E_γ and ΔT_2 is created as shown in Figure. (4.11), where E_γ is the "addback" energy of the γ ray detected at the focal-plane clover detector. The energy-gated time spectra are shown in Figure. (4.12). The spectrum in Figure. (4.12)(a) is obtained by a sum gate on the low-lying 886-, 343-, and 391-keV γ-rays which were fed by both (new- and the 750-ns) isomers. Therefore, the following equation was fitted:

$$
\begin{aligned}
Y = & \frac{A0 * T_2}{T_1 - T_2} * \{exp(-\frac{0.693 * t}{T_1}) - exp(-\frac{0.693 * t}{T_2})\} \\
& + A1 * exp(-\frac{0.693 * t}{T_1}) + A2 * exp(-\frac{0.693 * t}{T_2}), \qquad (4.1)
\end{aligned}
$$

where, A0, A1 and A2 are three normalization parameters corresponding to the decay of the higher-lying isomer via the lower-lying isomer, the decay of the higher-lying isomer via the 457-keV transition and the independent decay of the lower-lying isomer, respectively. T_1 and T_2 are the half-lives of the higher-lying (new) and the lower-lying (750-ns) isomers, respectively. The fitting, shown in Figure. (4.12)(a), gives the half-life of the new isomer as $T_1 = 1.6(1)$ μs and the value of $T_2 = 0.7(1)$ μs agrees well with the half-life of the lower-lying isomer determined in Ref. [4]. The fitted values of $A0 = 0.5(1)$, $A1 = 3.5(3)$ and $A2 = 8.1(3)$ give ideas about the branching ratio of the decay of the new isomer and the relative population of the two isomers.

The time spectrum shown in Figure. (4.12)(b) is obtained by gating on 457-keV transition which is fed by the new isomer only. As the statistics was limited in this case, the time spectrum was time-binned into six "cuts" and fitted. This gives a half-life of 1.6(2) μs for the new isomer and is in very good agreement with that obtained in the first case using sum-gated spectrum. Therefore, the half-life of the new isomer is adopted to be 1.6(1) μs.

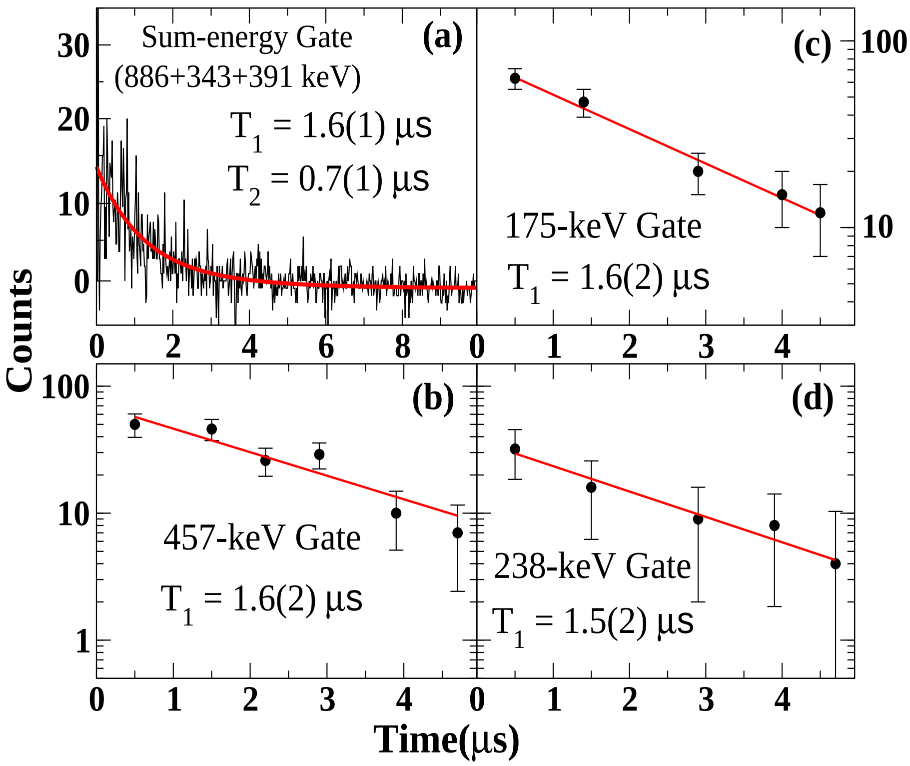

Figure 4.12: (a) Time spectrum with sum-energy gate on 886-, 343- and 391-keV transitions in ^{195}Bi. T_1 and T_2 are the half-lives of the higher-lying new isomer and the lower-lying known isomer in ^{195}Bi, respectively. See text for the details about the fitted equation. (b) Time spectrum gated by 457-keV transition in ^{195}Bi, (c) Time spectrum gated by 175-keV transition and (d) Time spectrum gated by 238-keV transition. Because of the limited statistics in the later three spectra, total data were time-binned into a few points.

In order to identify any possible decay γ rays from the new isomer, we have closely looked into the spectrum of Figure. (4.10) for any new γ ray which corresponds to the same half-life of the new isomer. Two possible γ-rays, 175- and 238-keV, have been identified which could be the possible decays of the new isomer in ^{195}Bi. The presence of these two lines are shown in the inset (a) in Figure. (4.10). They are not known to belong to any of the nuclei which are produced in our reaction and are isomeric in nature. We have projected the time spectra gated by 175-keV and 238-keV transitions and are shown in Figure. (4.12)(c) and 4.12(d), respectively. In these two cases also, the time spectra were binned into a few points and fitted. The half-lives of 1.6(2) μs and 1.5(2) μs were obtained for the 175-keV and 238-keV gated spectra, respectively. The excellent agreement of these half-lives with that obtained for the new isomer, clearly supports the placement of these transitions as the decay of the new isomer. These two γ-rays could also be observed in the ER-gated summed $\gamma - \gamma$ coincidence spectrum shown in Figure. (4.13) with gates on known γ-rays in ^{195}Bi. Although the statistics is limited but it gives clear indication that these two transitions belong to ^{195}Bi.

The Weisskopf estimate of half-life for a 238-keV $M2$ transition is calculated as 1.22 μs, considering hindrance factor HF($M2$) = 1 as suggested in Ref. [16,17] for $A > 150$ nuclei, which matches well with the measured half-life of the new isomer. Therefore, we propose that the new isomer decays by the 238-keV $M2$ transition. It may be noted here that in ^{190}W, the 97-keV transition, decaying from the 10^-, 240-μs isomer was assigned as $M2$ transition from the half-life consideration which also indicated a hindrance factor close to unity for the $M2$ transition [18]. For intensity balance with the 457-keV transition, total conversion coefficient of $\alpha_T = 4(1)$ is required for the 238-keV transition which is in good

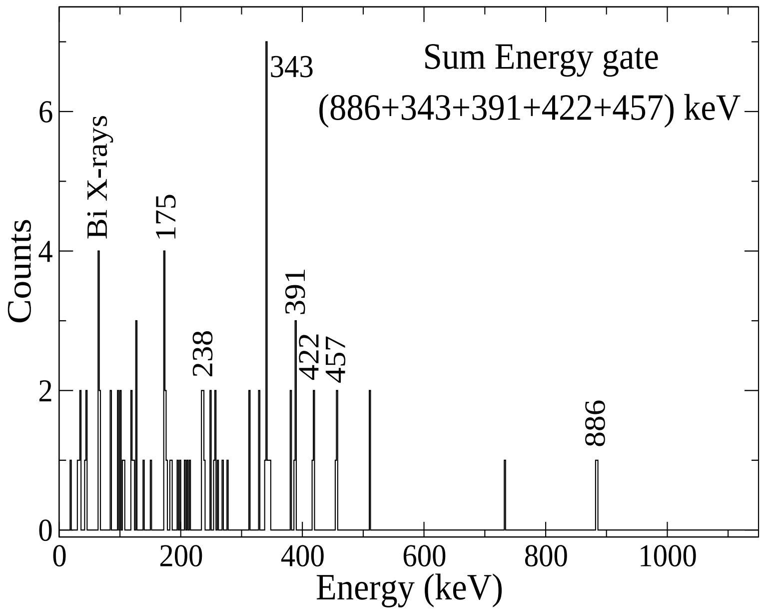

Figure 4.13: ER-gated summed γ-ray coincidence spectrum with gate on known transitions in ^{195}Bi.

agreement with the calculated value of 3.73(6) [19] considering the 238-keV γ-ray as an $M2$ transition. With this assignment, the total relative intensity of 238-keV transition comes out to be 21(7) (in arbitrary unit) which matches well, within uncertainties, with the total intensity of 16(4) (in the same arbitrary unit) for the 175-keV transition, considering it as an $E2$ transition. Hence, the 175-keV γ ray has been tentatively assigned as an $E2$ transition. Therefore, we propose that the new isomer decays by the 238-keV transition followed by the 175-keV transition to the 2923 keV level in ^{195}Bi as shown in Figure. (4.14). The excitation energy of the new isomer is, therefore, proposed to be 3336 keV with most-likely spin-parity of $31/2^{-}$.

As discussed above, the new isomer is expected to have another decay path through the 750-ns isomer as well. We have observed a weak 702-keV γ ray in the decay spectrum (shown in inset (b) in Figure. (4.10)). The energy of this γ-ray fits well between the

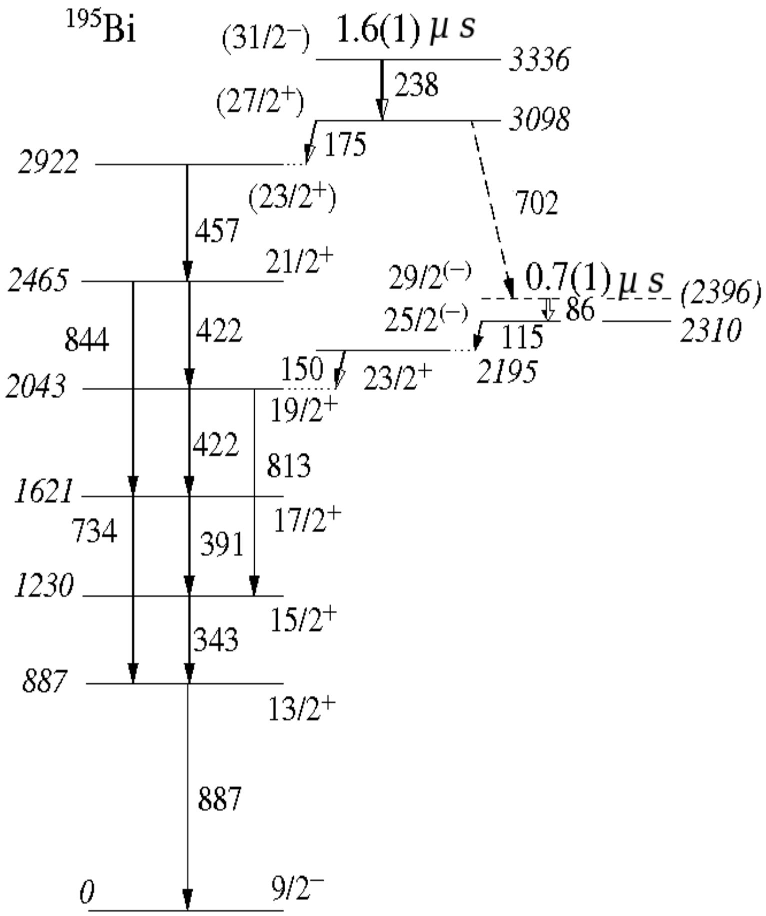

Figure 4.14: The new 1.6(1)-μs isomer identified in the present work and its decay are shown in the level scheme of ^{195}Bi. The lower part of the level scheme is adopted from Ref. [2]. The half-life of the $29/2^{(-)}$ isomer is given as obtained in the present work.

3098-keV $(27/2^{+})$ level and the 2396-keV $29/2^{(-)}$ isomer. The intensity ratio of 6.0(19) between the 702 and the 457-keV γ rays is in good agreement with the branching ratio, estimated from the $A0$ and $A1$ values in the fitting of Figure.(4.12)(a). However, the time spectrum gated by the 702 keV γ-ray could not be obtained. Also, this γ ray was not observed in the ER-gated $\gamma - \gamma$ coincidence spectrum. We understand that these are, most likely, due to limited statistics.

4.4 Discussion

The high-spin isomeric states in Bi isotopes are understood as three-quasi particle states arising from the coupling of the odd-proton in $h_{9/2}$ (ground state) or $i_{13/2}$ orbital coupled with the different two-quasi particle states (5^-, 7^-, 9^- and 12^+) in the even-even Pb ($Z = 82$) core. The two- quasi particle states in Pb core involve neutron-holes in negative-parity $f_{5/2}, f_{7/2}$ orbitals and positive parity $i_{13/2}$ orbital. In ^{197,199,201}Bi isotopes, the $29/2^-$, $31/2^-$ and $33/2^-$ states were interpreted as the multiplets of $\pi h_{9/2} \otimes \nu_{12^+}$ configuration [5,6]. In ^{197}Bi, a second $31/2^-$ state, observed at an energy very close to the first one, was interpreted as the coupling of the $\pi i_{13/2}$ orbital with the ν_{9^-} state [5]. The $29/2^-$ isomer has been observed in all the odd-A Bi isotopes from $A = 193$ to $A = 207$, but no isomer with spin higher than $29/2\ \hbar$ was known in $A < 197$ isotopes prior to the present study. In ^{195}Bi, the $29/2^{(-)}$ isomer was known at a tentative excitation energy of 2396 keV, while in ^{193}Bi, it was observed at an excitation energy of 2357+Δ keV [3]. Recently, a $29/2^+$ isomer has been reported in ^{193}Bi and was interpreted as $\pi h_{9/2} \otimes \nu_{11^-}$ [10]. However, no $29/2^+$ isomer has been reported in ^{195}Bi, yet. The systematics of the excitation energies of the high-spin isomers (and multi-quasi particle states) in Bi isotopes have been discussed in the subsequent paragraph and it supports the excitation energy and spin-parity assignment of the new isomer in ^{195}Bi as well as its configuration as $\pi i_{13/2} \otimes \nu_{9^-}$.

The excitation energy of the three-quasi particle configuration in the odd-A Bi isotopes can be estimated from the energy of the neighbouring core state and the excitation energy of the odd-particle state in the odd-A isotope using the following equation,

$$E^A_{3qp} = E^A_{1qp} + \frac{E^{A-1}_{2qp} + E^{A+1}_{2qp}}{2} \tag{4.2}$$

where E^A_{3qp} is the excitation energy of a three-quasi particle configuration in an odd-A Bi isotope, E^A_{1qp} is the excitation energy of the corresponding one-quasi proton configuration in that odd-A Bi isotope and the second term in the right hand side is the energy of the core state which is taken from the average of the excitation energies of the corresponding two-quasi particle configuration in the neighbouring Pb nuclei. The systematics of the observed excitation energies of $27/2^+$, $29/2^-$ and $31/2^-$ states are shown in Figure. (4.15) along with the estimated values calculated from Eq. (3) for the $\pi h_{9/2}{\otimes}\nu_{9^-}$, $\pi h_{9/2}{\otimes}\nu_{12^+}$ and $\pi i_{13/2}{\otimes}\nu_{9^-}$ configurations. It can be seen that the observed energies of the $27/2^+$ states for most of the isotopes match well with the estimated values for the $\pi h_{9/2}{\otimes}\nu_{9^-}$ configuration. Similarly, the estimated values for the $\pi h_{9/2}{\otimes}\nu_{12^+}$ configuration is in between the observed energies of the $29/2^-$ and $31/2^-$ multiplets. The excitation energy of the new isomer in ^{195}Bi is in close proximity with the estimated value for the $\pi i_{13/2} \otimes \nu_{9^-}$ configuration. The lowest energy state in this configuration is $31/2^-$ as discussed in Ref. [5]. It was also argued in Ref. [5] that this configuration in ^{197}Bi becomes more attractive because of the increasing involvement of $\nu f_{7/2}$ orbital in the 9^- state in ^{196}Pb. The relative contribution of $\nu f_{7/2}$ orbital increases with the decreasing neutron number. In ^{193}Bi, the $31/2^-$ state with the above configuration is expected at 3066 keV, but could not be identified yet.

^{195}Bi having neutron number $N = 112$ has the distinction of a transitional nucleus with the observation of onset of deformation in this nucleus as one moves from the neutron closed-shell towards the mid-shell in the isotopic chain of Bi nuclei. No rotational band was observed in the Bi isotopes for $A > 195$, whereas, the $31/2^-$ isomer, that we have

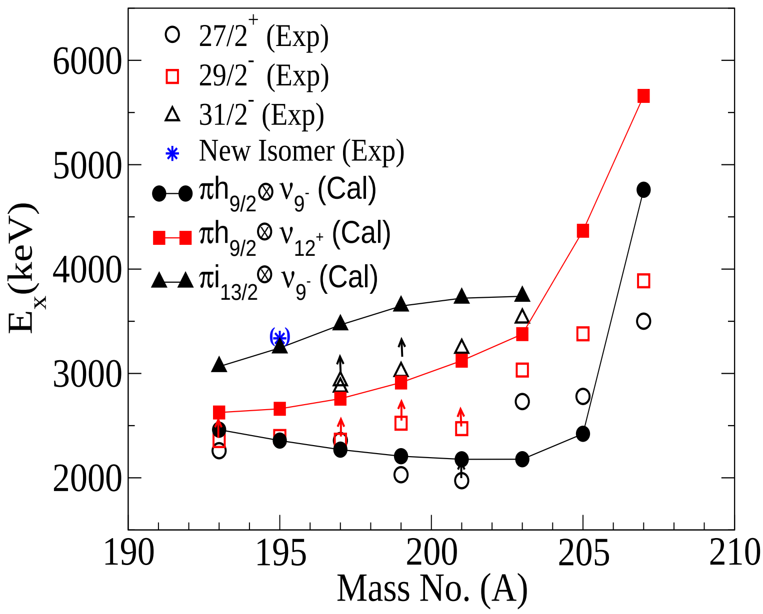

Figure 4.15: Systematics of the measured excitation energies, denoted by (Exp), of the high-spin isomers in Bi isotopes. The arrows indicate that the value is the lower limit. The estimated values for the configurations, denoted by (Cal), are calculated using Eq. (3) and as described in the text.

observed in ^{195}Bi, has not been identified in the Bi isotopes for $A < 195$. Therefore, ^{195}Bi behaves more like ^{193}Bi (and lighter isotopes) in the low-spin and low-excitation regime while it behaves more like ^{197}Bi (and heavier isotopes) in the high-spin and high-excitation regime.

4.5 TRS Calculations

In order to investigate the deformation driving effect of the single-particle proton orbitals above the $Z = 82$ shell closure, the shapes of ^{195}Bi and its even-even core ^{194}Pb, in the configurations under discussion, have been studied from the Total Routhian Surface (TRS) calculations. In these plots, $\gamma = 0°$ ($\gamma = -60°$) corresponds to prolate (oblate) shape.

The TRSs are calculated for the three configurations in ^{195}Bi those have been discussed in the previous section i.e., for $\pi i_{13/2} \otimes \nu_{9^-}$, $\pi h_{9/2} \otimes \nu_{9^-}$ and $\pi h_{9/2} \otimes \nu_{12^+}$ and the surfaces are shown as contour plots in Figures. (4.16)(a), (4.16)(b) and (4.16)(c), respectively. The TRS for the two-quasi particle ν_{12^+} ($\nu i_{13/2}^{-2}$) configuration in the neighbouring even-even ^{194}Pb is also shown in Figure. (4.16)(d). These Figures show that a minimum in the TRS occurs at an oblate deformation ($\gamma \sim -60°$) with $\beta_2 \sim 0.12$ for the $\pi i_{13/2} \otimes \nu_{9^-}$ configuration (Figure. (4.16)(a)) but for other configurations, including the two-quasi particle configuration in ^{194}Pb, the minimum in the TRSs are almost at spherical shape ($\beta_2 \leq 0.05$). The difference between the configuration in panel (a) and others in Figure. (4.16) is the involvement of a proton $i_{13/2}$ orbital. In the Nilsson diagram, the low-Ω components of a high-j orbital have larger deformation driving effect compared to the high-Ω orbitals for

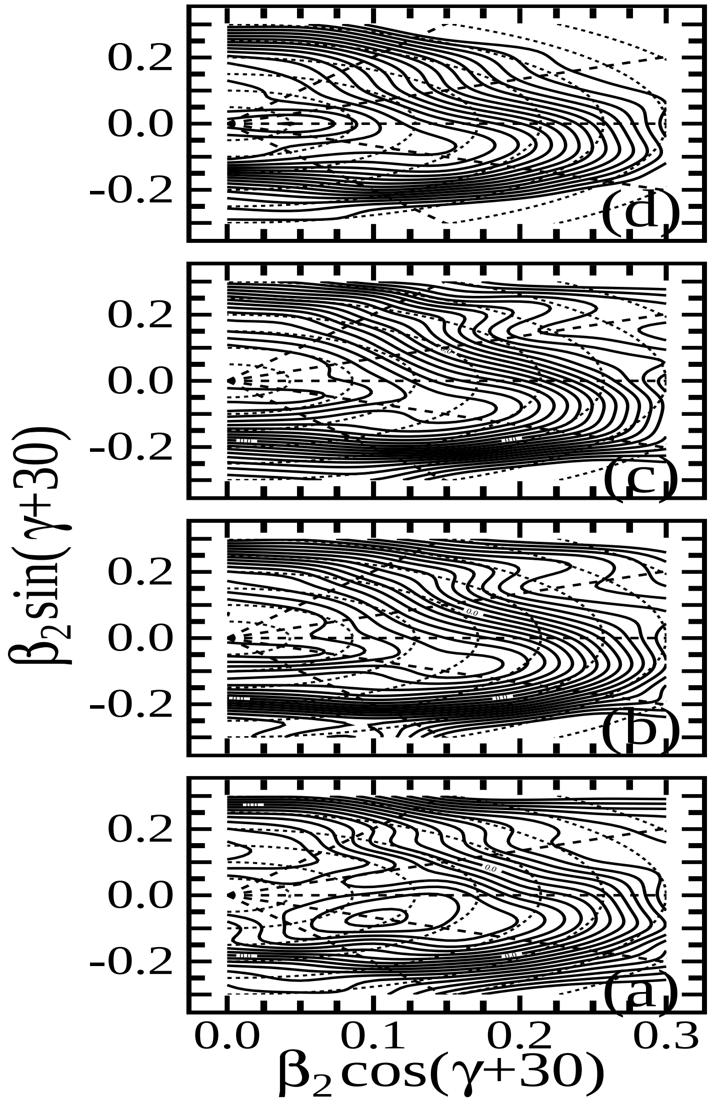

Figure 4.16: Total Routhian Surface (TRS) for different configurations of the ^{195}Bi and ^{194}Pb. The panels (a), (b), (c) are for $\pi i_{13/2} \otimes \nu_{9^-}$, $\pi h_{9/2} \otimes \nu_{9^-}$, $\pi h_{9/2} \otimes \nu_{12^+}$ configurations in ^{195}Bi and the panel (d) is for the two-neutron $i_{13/2}^{-2}$ configuration in ^{194}Pb. The contours are 300 keV apart.

the prolate shape where as, for oblate shape, the opposite is true. This indicates that if a high-j shell is fully or nearly fully occupied then there is not much shape driving effect of the last occupied orbital. For neutron number $N \sim 114$, the neutron Fermi level lies near the tip of the neutron $i_{13/2}$ orbitals and therefore, $\nu i_{13/2}$ orbital do not have much deformation driving effect for these nuclei. This is reflected in the near-spherical shape obtained for the two-neutron configurations of two-$i_{13/2}$ (ν_{12^+}) (Figure. (4.16)(d)) as well as $i_{13/2}f_{5/2}$ (ν_{9^-}) in ^{194}Pb. Inclusion of an additional proton in the $h_{9/2}$ orbital to any of these two-neutron configurations does not alter the shape and it remains near spherical as seen in Figure. (4.16)(b,c). However, inclusion of a proton in $i_{13/2}$ orbital to the ν_{9^-} changes the shape to substantial oblate deformation as seen in Figure. (4.16)(a). This shows that the proton $i_{13/2}$ orbital has a large oblate driving effect in ^{195}Bi compared to the proton in $h_{9/2}$ orbital. The TRS calculations for the one-quasi particle $\pi i_{13/2}$ configuration show similar deformation in ^{195}Bi [2]. A rotational band in ^{195}Bi has also been observed which is based on the low-lying $\pi i_{13/2}$ orbital but no rotational band has been observed in this nucleus based on the $\pi h_{9/2}$ ground-state. However, in ^{193}Bi rotational bands based on both $\pi h_{9/2}$ ground-state and $\pi i_{13/2}$ excited state have been observed. This indicates that because of the lower neutron number, the neutron Fermi level lies close to the lower half of the $\nu i_{13/2}$ orbitals which affect the shape in the lighter Bi isotopes. It is worthwhile to note that the TRS calculations in Ref. [2] show triaxial shape at higher rotational frequencies, after the back-bending, for the $\pi i_{13/2}$ band that is, for the positive-parity 3-quasi-particle configuration, whereas, an axial oblate shape is predicted in the present calculations for the negative-parity 3-quasi-particle isomer.

As the TRS calculations predict a well deformed oblate shape for the new isomeric state having deformation similar to the low-lying $\pi i_{13/2}$ state, therefore, a rotational band-structure, similar to that observed on the $13/2^{+}$ state, is expected to be built up on this isomeric state. The observation of such band structure was beyond the scope of the present experiment. However, it would be interesting to look for such a band-structure above this high-spin isomer in ^{195}Bi in a future experimental investigation.

4.6 Conclusion

Isomer decay spectroscopic study of ^{193}Bi and ^{195}Bi have been done for the first time at the focal plane of the gas-filled HYbrid Recoil mass Analyzer (HYRA) using the fusion evaporation reaction of ^{30}Si on ^{169}Tm target. A couple of new gamma transitions i.e 186- and 279- keV have been identified in ^{193}Bi. The decay of the known 3-μs isomer in ^{193}Bi is confirmed and its half-life is remeasured. The value obtained for the half-life of this isomer in the present measurement agrees well with the known value. A new high-spin isomer has been identified in ^{195}Bi. The decay of the new isomer clearly indicates that it lies above all the known states in this nucleus. The half-life of the new isomer has been measured and found to be 1.6(1) μs. The spin-parity of the new isomer is proposed to be $31/2^{-}$ with a three-quasi particle configuration of $\pi i_{13/2} \otimes \nu_{9^{-}}$ from the systematics of the high-spin isomers in the neighbouring isotopes. Indication of a 702 keV transition in the second decay path of the new isomer via the 700-ns isomer could be observed in the present work, however, more works are needed to establish this. The TRS calculations show an oblate deformation for this isomer similar to the low-lying one-quasi particle $\pi i_{13/2}$ state in this nucleus. The calculations also suggest that the $i_{13/2}$ proton orbital has a larger shape driving effect in ^{195}Bi compared to the $h_{9/2}$ proton orbital. A rotational band is expected to be built on the newly observed isomer which would be an interesting case to study in future.

Bibliography

[1] M. Lipoglavsek et al., Phys. Lett **B 593**, 61 (2004).

[2] H. Pai et al.,Phys. Rev. **C 85**, 064317 (2012)

[3] P. Nieminen et al.,Phys. Rev. **C 69**, 064326 (2004).

[4] T. Lönnroth et al.,Phys. Rev. **C 33**, 1641 (1986).

[5] T. Chapuran et al.,Phys. Rev. **C 33**, 130 (1986).

[6] W.F. Piel et al.,Phys. Rev. **C 31**, 2087 (1985).

[7] A. Hürstel et al., Eur. Phys. J **A 15**, 329 (2002).

[8] X. Zhou et al., Z. Phys. **A 353**, 3 (1995).

[9] G.K. Mabala et al., Eur. Phys. J **A 25**, 49 (2005).

[10] A. Herzáň et al., Phys. Rev. **C 92**, 044310 (2015).

[11] N. Madhavan et al.,Pramana - journal of physics **75**, 317 (2010).

[12] Ajith Kumar B.P, E.T. Subramaniam, Kusum Rani and Kundan Singh, Proceedings of the DAE-BRNS Symposium on Nuclear Physics, Saha Institite of Nuclear Physics, Kolkata, India, Dec. 26 - 30, 2001, edited by Arun K. Jain and D.C. Biswas, Vol. **44B**, 390 (2001).

[13] G. Duchene et al., Nucl. Inst. and Meth. Phys. Res. **A 432**, 90 (1999).

[14] A. Gavron, Phys. Rev. **C 21**, 230 (1980).

[15] O.A. Capurro et al., Phys. Rev. **C 55**, 766 (1997).

[16] J.K. Tuli (Ed.), Nuclear Data Sheets, **124**, p iv (General Policies) (2015).

[17] W. Reviol et al., Phys. Rev. **C 61**, 044310 (2000).

[18] G.J. Lane et al., Phys. Rev. **C 82**, 051304(R) (2010).

[19] Online Computer code "BRICC" at http://bricc.anu.edu.au/ and T. Kibedi et al., Nucl. Instr. and Meth. **A 589**, 202 (2008).

Chapter 5

Study of Rotational Bands in ^{195}Tl

5.1 Introduction

The thallium nuclei with proton number Z = 81 is situated close to the spherical lead nuclei at Z = 82 compared to the prolate deformed rare earth nuclei. At the same time various nuclear shapes have been reported in several Hg, Tl and Pb isotopes in the mass region A $\sim$ 180-190. The low and high Ω components of $\pi h_{9/2}$ and $\pi i_{13/2}$ orbitals come down in energy for both prolate and oblate deformation, respectively from above the Z = 82 spherical shell closure. These orbitals play a crucial role in breaking the nuclear spherical symmetry. On the other hand $\nu i_{13/2}$ orbital gets filled up at neutron number N = 114, opens up the possibility of neutron hole states in $i_{13/2}$ orbital for N$\leq$114. So it is important to study the effect of these high-j proton and neutron orbitals in determining the nuclear shape at high spin in this mass region. Also this unique set of high-j proton and neutron orbitals near their Fermi surface with various deformation driving effects have presented suitable playing ground to study other exotic phenomena like Magnetic

Rotation in various Pb and Hg isotopes [1,2], Nuclear Chirality [3,4] etc. for the nuclear structure physics.

The ground-state spin-parity of odd-A Tl isotopes has been observed as $1/2^+$ [5–8] corresponding to the proton hole in the $3s_{1/2}$ orbital and the low lying $3/2^+$ excited state has been interpreted by the occupation of the odd proton in the $\pi d_{3/2}$ orbital. Experimentally $9/2^-$ state, assigned for $h_{9/2}$ orbital situated above the Z = 82 shell closure, in all odd-A thallium isotopes have been established as an isomeric state [5–8]. In neutron mid shell odd-A Tl isotopes ranging from mass number 185 to 201, decoupled rotational bands have been observed based on prolate deformation in ^{185,187,191}Tl [9, 10] isotopes and strongly coupled rotational bands based on oblate deformation in odd-A $^{191-201}$Tl isotopes [7, 11, 12, 14, 15]. The strongly coupled bands based on $\pi h_{9/2}$ state has been observed beyond neutron pair breaking in ^{189,191,193}Tl isotopes [11, 12] but a very limited high spin information is available for ^{195,197,199}Tl isotopes [7, 14] and are restricted below neutron pair alignment.

In the neighbourhood of ^{195}Tl, "quasi-vibrational" bands have been reported in the even-even γ- soft ^{192,194}Hg [17] in the mid spin range. Also the low lying excited states in $^{190-202}$Hg isotopes could be interpreted by rigid-triaxial-rotor model [18]. This shows the Hg core in this mass region have substantial triaxiality with γ- softness. Recently, candidates of chiral partner bands have been reported in the odd-odd isotopes neighbouring ^{195}Tl. In ^{194}Tl a pair of doubly degenerate bands have been reported based on 4-qp ($\pi h_{9/2} \otimes \nu i_{13/2}^{-3}$) configuration [3]. These bands have near-degeneracy in the excitation energies, with $\triangle$E not longer than 110 keV in the whole spin range of I = 19-23. Whereas, degenerate bands based on 2qp ($\pi h_{9/2} \otimes \nu i_{13/2}$) configuration were reported in ^{198}Tl [4] with average energy separation $\triangle$E$\sim$459 keV.

Therefore, it is very important to have high spin data for ^{195,197}Tl isotopes to have comprehensive understanding of the effect of neutron pair alignment in $\nu i_{13/2}$ orbital in odd-A Tl isotopes. Also it is interesting to look for similar degenerate bands based on odd quasiparticle configuration to have a better understanding of their mechanism irrespective of the mass region.

Prior to the present work, the high spin information for ^{195}Tl was limited to only two bands: the band based on $\pi h_{9/2}$ orbital was known up to spin and excitation energy of $27/2^-$ and 3156 keV, respectively (below the neutron pair breaking region). A band based on 3-qp configuration was known up to spin and excitation energy of $35/2^-$ and 4394 keV, respectively using α induced fusion evaporation reaction with one planar Ge detector and two large volume Ge(Li) detectors. In the present thesis work, high spin gamma- ray spectroscopy study has been carried out for ^{195}Tl using high resolution, higher-efficiency germanium clover detector array using heavy ion fusion evaporation reaction. This allowed us to populate higher spin states with the observation of several new band structures. The ground state band based on $\pi h_{9/2}$ orbital has been extended beyond first band crossing. Various other band structure observed in the present study have been discussed in the following sections.

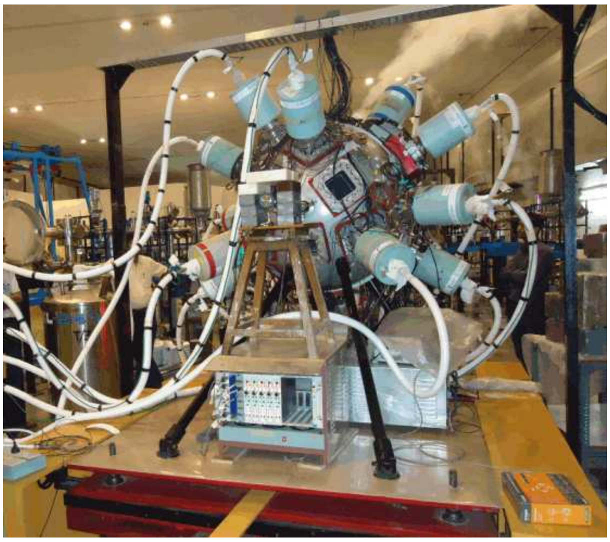

Figure 5.1: Indian National Gamma Array (INGA) at TIFR.

5.2 Experimental Methods

In the present thesis work, the excited states of ^{195}Tl was populated via ^{185,187}Re(^{13}C, xn)^{195}Tl fusion evaporation reaction at 14-UD BARC-TIFR Pelletron at Mumbai, India using the Indian National Gamma Array (**INGA**). During the experiment **INGA** consisted of 15 clover detectors with BGO anti-Compton shields as shown in Figure. (5.1). Natural Rhenium foil of isotopic ratio 37:63 ($^{185-187}$Re), thickness 18.5 mg/cm^2 was used as target. The experiment was carried out at 75 MeV of beam energy to maximize the yield of ^{195}Tl according to PACE-IV calculations as shown in Figure. (5.2). The clover detectors were placed in six angles with two clovers each at $\pm 40^\circ$ and $\pm 65^\circ$ while four clovers were at 90° and three were at -23° angles. The average count rate to each crystal was limited to $\sim$4000/s. The clover detectors were calibrated by using ^{133}Ba and ^{152}Eu radioactive sources.

Two and higher-fold coincidence data with time stamp were recorded in a fast digital data acquisition system based on Pixie-16 modules of XIA LLC [20, 21]. A time window of 150 ns is set for the coincidence between the first triggers of individual channels, and the coincidence trigger was kept open for 1.5 μs. For photopeak efficiency measurement, the digital acquisition system was used in the singles mode. The **M**ulti p**AR**ameter time-stamped based **CO**incidence **S**earch **(MARCOS)** program, developed at TIFR was used to sort time-stamped data to generate a E_γ-E_γ matrix and E_γ-E_γ-E_γ cube in RADWARE compatible format. A time window of 400 ns was selected to generate E_γ-E_γ matrix and E_γ-E_γ-E_γ cube. The matrix contained a total of 3.1 $\times$ 10^8 γ-γ coincidence events. The analysis has been done with RADWARE package [22]. The new modified level scheme of ^{195}Tl has been constructed using coincidence and intensity relations of γ- rays. The intensities of the γ- rays are obtained from the E_γ-E_γ matrix using a single-gated spectrum. The spin and parity of the nuclear states have been assigned using mutipolarity and type (E/M) of the decaying gamma- transitions.

The multipolarity of the γ- rays are determined from the gated angular distribution [23] and directional correlation of oriented states (DCO) ratio method [24]. For DCO ratio analysis, the coincidence events were stored into an asymmetry matrix with data from the $\theta_1(90^\circ)$ detectors on one axis and data from the $\theta_2(157^\circ)$ detectors on the other axis with respect to the beam line. The DCO ratios are obtained from the formula

$$R_{DCO} = \frac{I_{\gamma_1}\ at\ 90^\circ,\ gated\ by\ \gamma_2\ at\ 157^\circ}{I_{\gamma_1}\ at\ 157^\circ\ gated\ by\ \gamma_2\ at\ 90^\circ} \tag{5.1}$$

where I_{γ_1} is the intensity of the γ_1- transition determined by putting a gate on stretched gamma ray (γ_2) on the above stated R_{DCO} matrix. The calculated DCO ratio for stretched

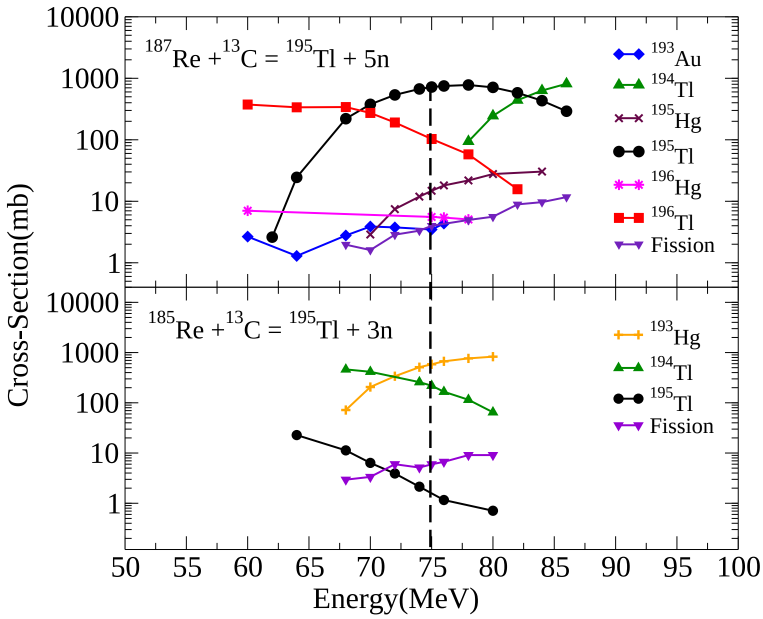

Figure 5.2: Excitation function drawn from PACE-IV calculation to identify the beam energy where production cross-section for ^{195}Tl maximizes.

quadrupole and dipole transition gated by stretched quadrupole transition comes out to be $\sim$ 1.0 and $\sim$ 0.5, respectively from the computer code angcor of E.S. Macias et. al., [25] for the above stated angular combination. The value of the DCO ratio depends on the detectors angle (θ_1 and θ_2) as well as the mixing ratio (δ) of the gamma- transitions. The validity of the R_{DCO} measurement is checked with the known transitions in ^{194}Tl and ^{196}Tl nuclei also populated in the present reaction. The DCO ratio for the known 278 keV dipole quadrupole mixed and 523 keV stretched quadrupole gamma transitions determined to be 1.96(6) and 0.95(4) gated by known 687 keV stretched quadrupole transition in ^{194}Tl [26]. The calculated values of DCO ratio came out to be 1.97 and 1.00 for the above stated γ transitions with mixing ratio (δ) 0.25 and 0, respectively.

The clover HPGe detectors used in the experiment, allowed us to assign definite parities of the excited states from the measurement of integrated polarization asymmetry (IPDCO)

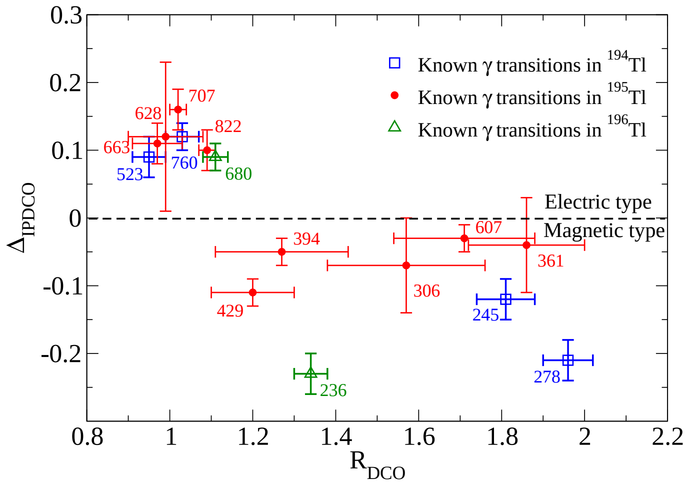

Figure 5.3: The DCO and the IPDCO ratios for a few known γ- rays in $^{194-196}$Tl obtained in the present work. The DCO ratios for various γ- rays are determined by gating on stretched quadrupole transition.

ratio [27, 28]. The γ-rays scattered parallel ($N_{\parallel}$) and perpendicular ($N_{\perp}$) to the reaction plane inside the detector medium gives us qualitative idea about the type of transition (E/M) through IPDCO ratio. The IPDCO ratio is obtained from the Eq.,

$$\Delta_{IPDCO} = \frac{a(E_{\gamma})N_{\perp} - N_{\parallel}}{a(E_{\gamma})N_{\perp} + N_{\parallel}}, \tag{5.2}$$

The correction due to the asymmetry in the array and response of the clover segments, defined by $a(E_{\gamma}) = \frac{N_{\parallel}}{N_{\perp}}$, has been checked using ^{152}Eu and ^{133}Ba sources. The asymmetry factor $[a(E_{\gamma})]$ comes out to be 1.011(16) (for details see Chapter 3), for this experiment. A positive or negative value of Δ_{IPDCO} indicates the transition to be electric or magnetic type in nature. In the present experiment Δ_{IPDCO} values could not be determined for γ- energy below 260- keV for weaker transitions. Below this energy the probability of

Compton scattering of a γ- ray from one crystal to another reduces considerably, giving very small measurable signal above threshold in both the crystals.

A comparative representation of DCO and IPDCO ratio for known γ- transitions in $^{194-196}$Tl [7, 19, 29] are shown in Figure. (5.3). The detailed results of DCO and IPDCO ratio for gamma- transitions belonging to ^{195}Tl are given in Table. [5.1].

5.3 Experimental Results

In the present experiment the strongly populated gamma- rays in coincidence with 707 keV transition belonging to ^{195}Tl [7] along with several new γ- transitions can be seen in Figure. (5.4). About 57 new gamma- transitions with asterisks (*) has been placed in the extended level scheme in Figure. (5.5). The respective informations like excitation energies of the nuclear levels, intensity, multipolarity and type of the decaying γ- transitions are given in Table. [5.1]. In order to get clear coincidence information for the nucleus of intent γ-γ-γ cube has been made. The gamma- rays in coincidence with double gated spectra in γ-γ-γ cube shows them to be in coincidence with two gamma- rays belonging to that nucleus.

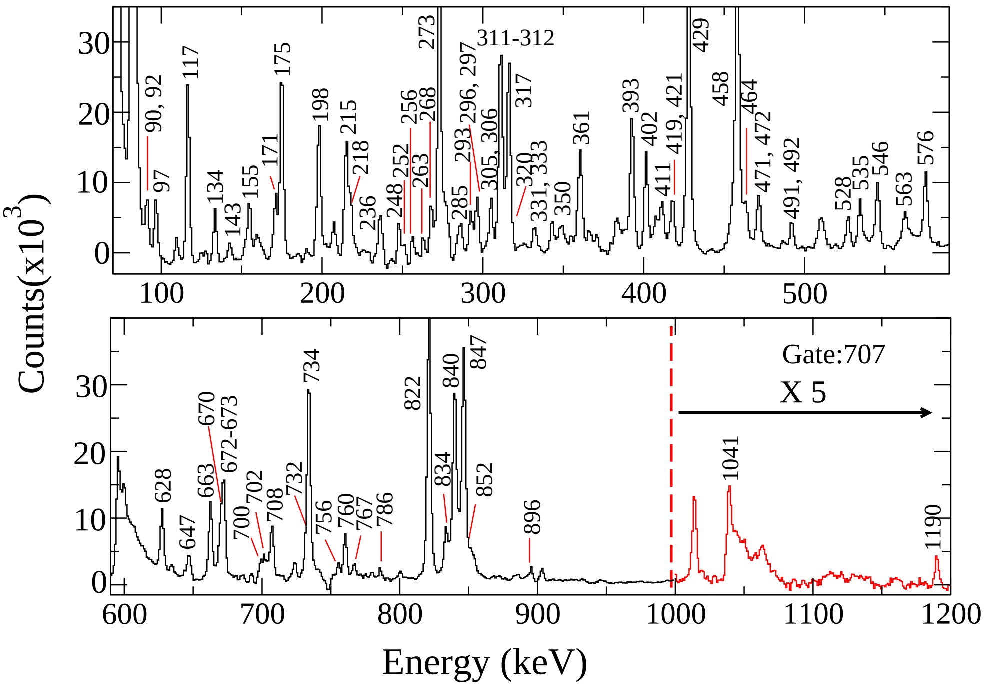

Figure 5.4: The strongly populated γ- transitions belonging to ^{195}Tl, gated by 707 keV transition are shown in two panels. In bottom panel the γ- ray counts from energy 1000 to 1200 are multiplied by 5.

The gamma- transitions belonging to ground state band based on $\pi h_{\frac{9}{2}}$ orbital (i.e., 117-, 306-, 393-, 429-, 458-, 546-, 576-, 663-, 734-, 822-, 852 keV gamma- rays) can be seen in coincidence with 707 keV gamma- ray in Figure. (5.4). In the same spectrum there is a strong presence of 708 keV γ- ray. It has been seen in coincidence with 742-546 keV double gated spectrum but absent in 742-663 keV double gated spectrum in γ-γ-γ cube. This led us to place 708 keV γ- ray above the 2470 keV level in the present study. The R_{DCO} value of this transition (see Table. 5.1) gated by stretched quadrupole 707- keV transition indicates it to be quadrupole in nature.

Earlier unplaced 402 keV transition in Ref. [7], is seen in coincidence with 97-, 198-, 273- and 472 keV transitions along with all other gamma- transitions belonging to band B1.

On the basis of its intensity, it has been placed above 3156 keV level in the present study. Several new transitions like 268-, 464-, 296-, 471-, 285- keV (dipole based on their R_{DCO} value) can be seen in the Figure. [5.6](a) along with 670-, 732-, 760-, 767-, 756 keV new (quadrupole based on their RDCO value) transitions. These transitions are placed in a regular sequence of band B2 by applying suitable double gates in the γ-γ-γ cube. In the same spectrum there are 256-, 700-, 786-, 844 keV new gamma- transitions which are seen in coincidence with the gamma- rays belonging to band B1 but not with transitions above 402 keV gamma- ray of band B2. The sum double gates of 273/786, 273/256, 822/786, and 458/786 gamma- transitions from γ-γ-γ cube (in the upper panel of Figure. (5.6)(b)) shows the presence of new gamma- transitions like 245-, 325-, 356-, 570-, 601-, 612 keV. These gamma- transitions are placed using suitable gates on γ-γ-γ cube, forming a band like structure B2a in the present level scheme as shown in Figure. (5.5). From DCO and IPDCO ratio, the 786 keV (see Table. 5.1) gamma- ray appears to be M1+E2 in nature fixing the spin band parity of 3647 keV level as $25/2^-$ for band B2a. Also the interconnecting 844- and 1041 keV gamma- rays between bands B2a and B2 comes out to be M1+E2 and E2 in nature based on their DCO and IPDCO ratio values as given in Table. 5.1.

The 563- and 834- keV gamma- rays seen in the Figure. (5.6)(a), are placed above the 2861 and 3826 keV level of band B2 in the present level scheme considering their coincidence relation by applying appropriate gating transitions in γ-γ-γ cube.

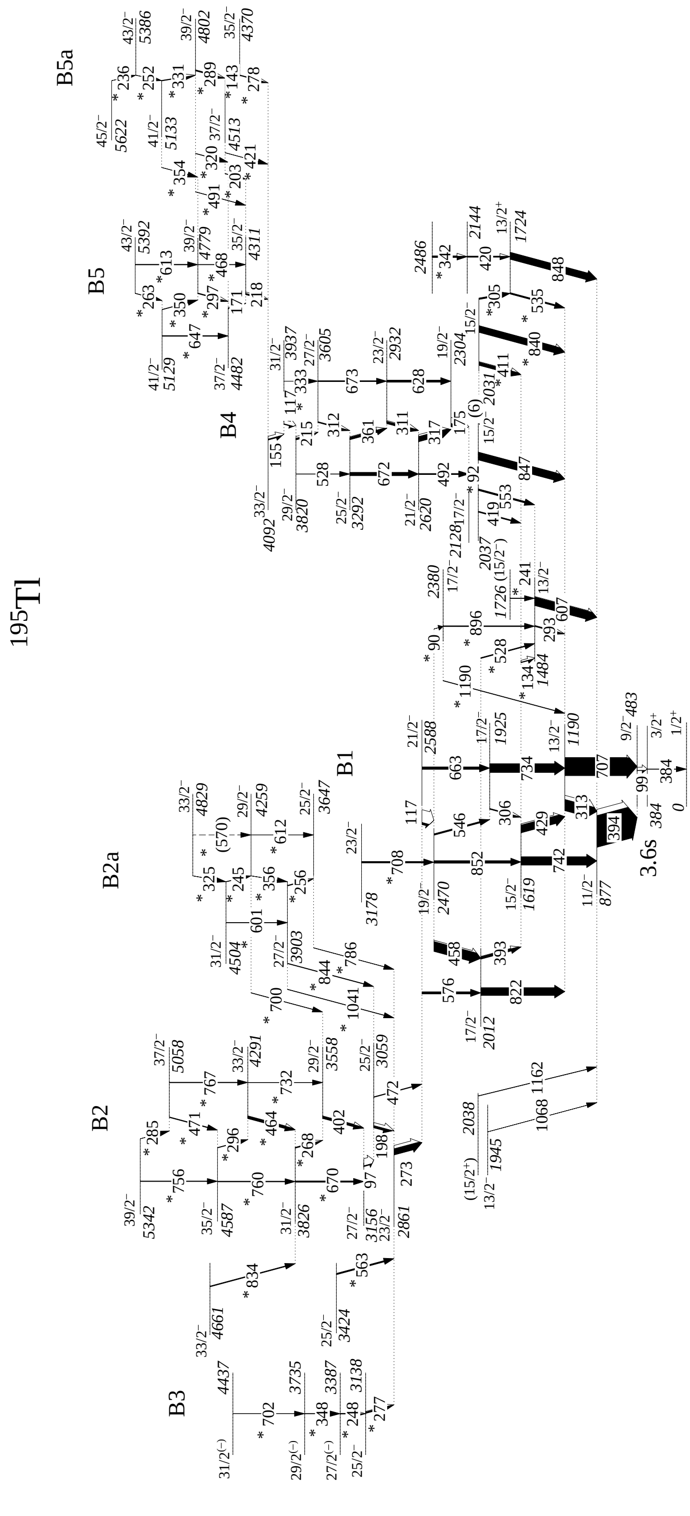

Figure 5.5: The proposed level scheme of ^{195}Tl obtained from the present work. The new gamma transitions observed in this work are shown by asterisk *. The width of the gamma transitions are proportional to their intensity.

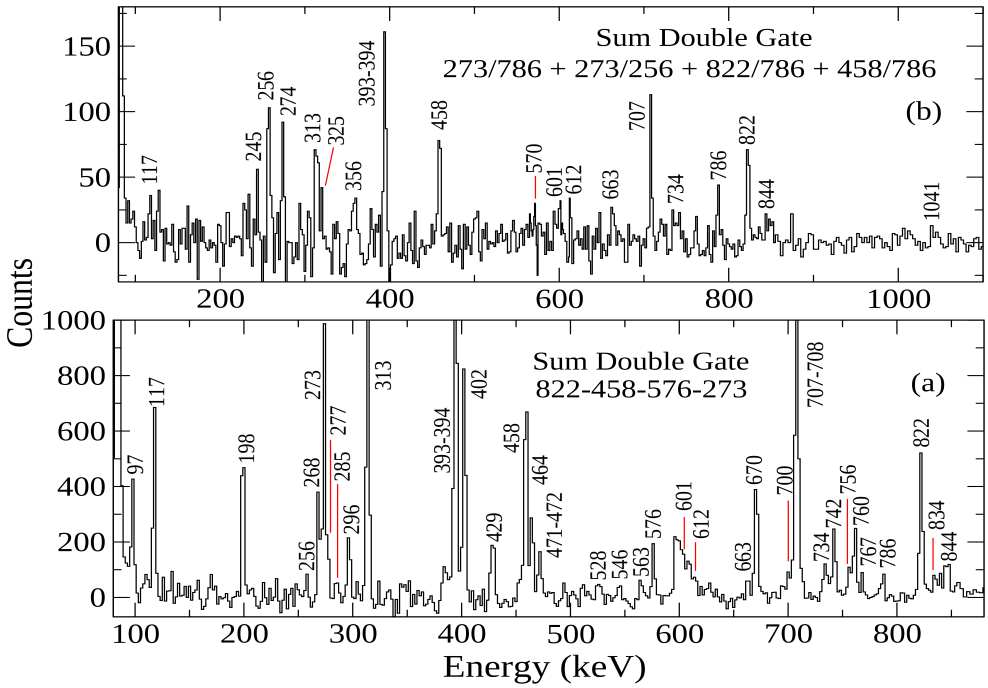

Figure 5.6: Spectra of γ- ray transitions belonging to band B2, B2a and their interconnecting transitions obtained from γ-γ-γ cube. (a) The spectrum generated by sum of double gates of 822-, 458-, 576-, 273-, 198 keV transitions in γ-γ-γ cube, shows γ- transitions belonging to both bands B2 and B2a along with their interconnecting γ- transitions like 700-, 786-, 844-, and 1041 keV. (b) The sum of double gates of 273/786, 273/256, 822/786 and 458/786 keV, shows γ- transitions belonging to band B2a and some of the lower lying γ- transitions of band B1.

In the double gated of spectrum of 394/607 keV gamma- rays as shown in Figure. (5.7)(a) we could identify new 134-, 241-, 896- keV gamma- rays. The DCO and IPDCO ratios of these transitions given in Table.[5.1], forms a irregular nuclear level structure. The 896- keV gamma- ray (level energy 2380 keV) above the 1484 keV level is in coincidence with 117 keV and rest of the gamma- transitions belonging to band B2 via newly placed 90 keV gamma- ray in the present level scheme. In the same Figure there is a 277 keV gamma-ray which, according to the coincidence relation, is placed above the 2861 keV level in the present study. The sum double gated spectrum of 273/277 + 458/277 + 277/822 keV transitions from γ-γ-γ cube in Figure. (5.7).(b) shows 248-, 348-, 702- keV transitions, which are in coincidence with each other. These gamma- rays are arranged in regular band like sequence B3 based on their intensity, multipolarity and type (see Table. [5.1]).

There is a 1190 keV gamma- ray in coincidence with 707 keV transition which can be seen in the bottom panel of Figure. (5.4), placed as the connecting transition between the 2380- and 1190- keV levels. The DCO and IPDCO ratio of this transition suggest it to be E2 in nature.

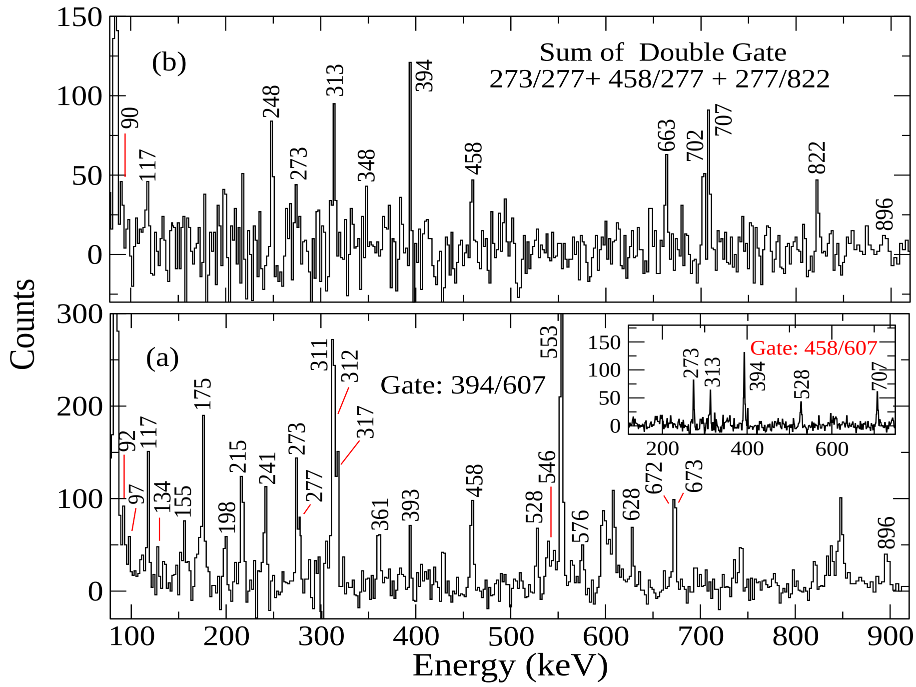

Figure 5.7: The spectra showing the gamma transition belonging to regular structures of band B3 and band B4. (a) Double gate of 394-607 keV gamma transitions shows the presence of 241-, 896 keV gamma- rays of irregular sequence above 1484 keV level. (b) Sum double gated spectrum of 273-277, 458-277, 277-822 shows the gamma transitions belong to band B3 and some of the gamma transitions belonging to band B1 (see Figure. (5.5)).

From the coincidence relation using suitable gates in γ-γ-γ cube 419-, 553- and 846- keV gamma- rays are found to be decaying from the 2037 keV energy state whereas 411- and 840- keV gamma- rays from the 2031 keV energy level 9see Figure. (5.5). The 419-, 553 and 846- keV gamma- rays were reported in Ref. [7] as tentative dipole (E1) transitions based on their angular distribution coefficients. In the present work polarization measurement for 419-, 553- and 846 keV gamma- rays allowed us to assign the parity of the 2037 keV level. In Figure. (5.8) the parallel scattering (solid black line) events are seen to be more than perpendicular scattering (dashed red line) events for 419-, 553- and 846 keV gamma-

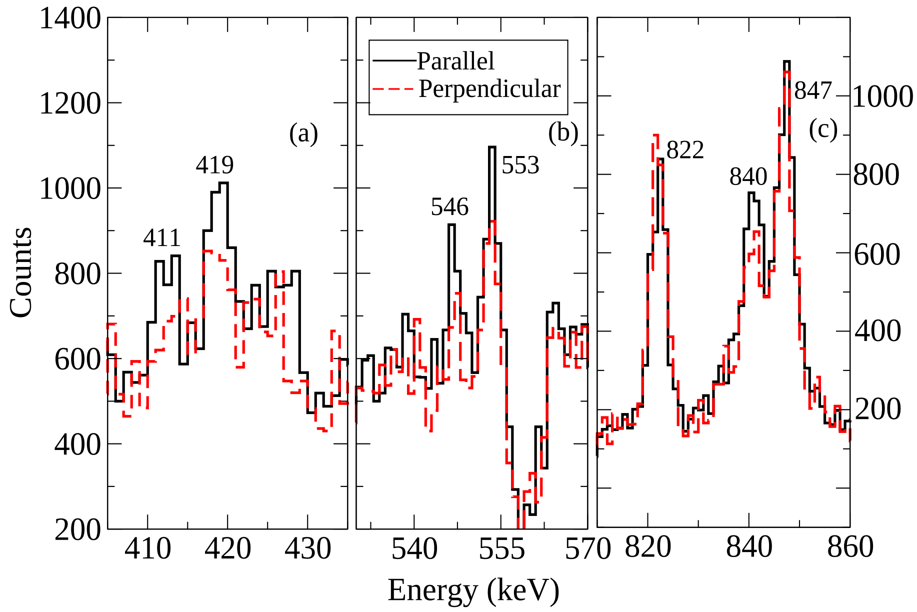

Figure 5.8: The parallel (solid) and perpendicular (dashed) components of 411-, 418-, 546-, 553-, 840-, 847- keV gamma transitions in ^{195}Tl obtained for IPDCO analysis from the present work. Here 546- and 822- keV transitions are known as magnetic and electric type. Whereas 419-, 553-, 840- keV transitions comes out to be magnetic type.

rays. In the same Figure 546- and 822- keV gamma rays can be seen predominantly magnetic and electric in nature. From the DCO and IPDCO ratio (as given in Table. 5.1) of these transitions the spin and parity of the 2037 keV level has been changed from $15/2^+$ to $15/2^-$. Recently a very similar band head spin and parity has been reported by H. Pai et al., [16] in ^{197}Tl.

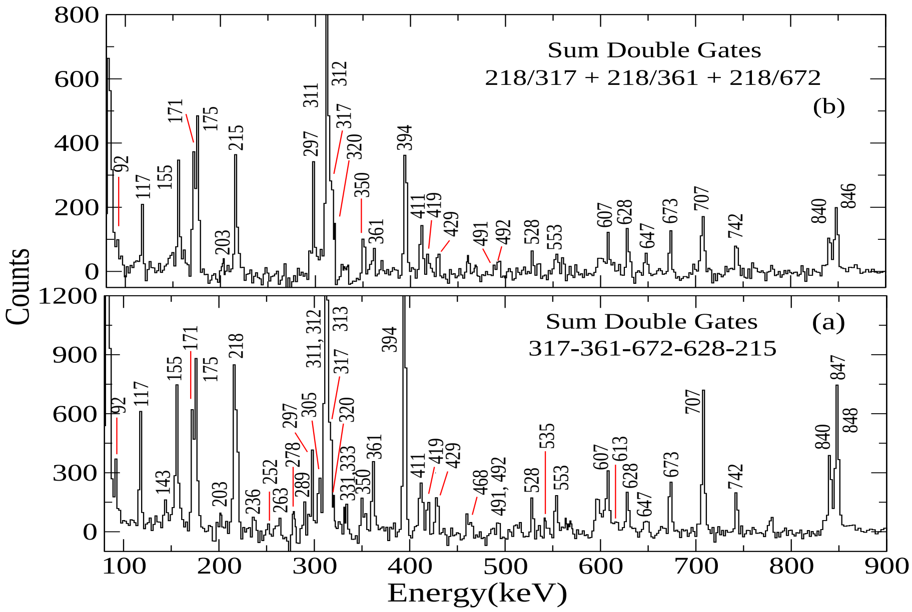

Figure 5.9: The spectrum (a) sum double gates of 317-361-672-628-215 keV gamma rays of band B4 shows the transitions belonging to bands B4, B5 and B5a in the new level scheme. (b) The sum double gates of 218/317 + 218/361 + 218/672 transitions shows only gamma- transitions belonging to bands B4 and B5.

A new 92 keV γ-ray has been placed within $17/2^- \rightarrow 15/2^-$ state which is in coincidence with 175-, 317-, 628- etc gamma- transitions decaying through both 2037 and 2031 keV levels. So there might be an unobserved 6 keV transition connecting these two energy levels. Earlier reported band in Ref. [7] above the 2037 keV level has been extended up to spin $43/2^-$ state with the observation of 263-, 297-, 350 keV dipole gamma- rays along with the 468-, 615-, 647 keV E2 crossover transitions as shown in Figure. (5.9)(a). In the same Figure there is also 143-, 236-, 252-, 278-, 289- and 331 keV gamma- transitions which are not present in the sum double gated spectrum of 218/317 + 218/361 + 218/672 keV gamma- rays in Figure. (5.9)(b). Therefore, 143-, 236-, 252-, 289-, and 331 keV gamma-rays are found to be in coincidence with each other according to the coincidence relation, forming a band structure B5a decays through 278 keV gamma- ray to the 4092 keV level in the present level scheme. There are several interconnecting gamma- rays like 203-, 320-, 354-, 421- and 491 keV linking band B5a with band B5 as shown by the boxed transitions in Figure. (5.10)(a). These interconnecting transitions are absent in the single gated spectrum of 143 keV gamma- ray in Figure. (5.10)(b). Further the presence of 320-, and 491- keV connecting transition has been confirmed with the single gated spectrum of 628 keV gamma- ray in Figure. (5.10)(a) inset.

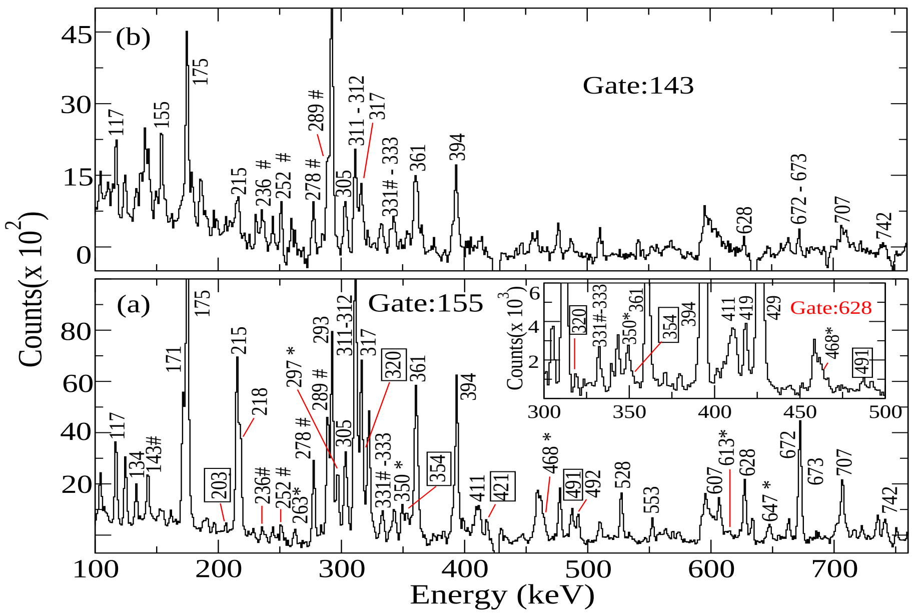

Figure 5.10: $\gamma-\gamma$ coincidence spectra (a) gated on 155- keV shows gamma- rays belonging to band B5 (marked as $*$) and gamma- rays belonging to band B5a (marked as #). (b) 143- keV gated spectrum shows # marked transitions belonging to band B5a with the absence of $*$marked transitions belonging to band B5. The interconnecting gamma- rays between bands B5a and B5 are enclosed inside the square box in the lower panel.

The double gated spectrum of 458-607 keV gamma- rays (see inset of Figure. (5.7).(a)), shows the presence of 528 keV gamma transitions which confirms it to be doublet in nature.

The DCO and IPDCO ratio for this transition establishes it to be E2 in nature which led to its placement between 2012 and 1484 keV levels (see level scheme Figure. (5.5)). The sum double gated spectrum of 317-361-672-628-215 keV gamma- rays in Figure. (5.9).(a) there are 305 and 535 keV gamma transitions. The former transition has been placed between 2031 and 1724 keV levels and the later one in between 1724 and 1190 keV levels.

Table 5.1: Energies (E_γ), intensities (I_γ), DCO ratios (R_{DCO}), IPDCO ratios (Δ_{IPDCO}) and deduced multipolarities of the γ rays in ^{195}Tl. The energies of initial states (E_i), spins and parities of initial (J_i^π) and final (J_f^π) states are also given.

E_γ [1] (in keV)	E_i (in keV)	$J_i^\pi \rightarrow J_f^\pi$	I_γ	R_{DCO} (Err)	Δ_{IPDCO} (Err)	Deduced multipolarity
90.2	2470.3	$\frac{19}{2}^- \rightarrow \frac{17}{2}^-$	0.14(17)	-	-	(M1+E2)
91.5	2128.4	$\frac{17}{2}^- \rightarrow \frac{15}{2}^-$	1.68(10)	0.93(15) [2]	-	(M1+E2)
97.1	3156.3	$\frac{27}{2}^- \rightarrow \frac{25}{2}^-$	2.86(9)	0.88(10) [2]	-	(M1+E2)
117.1	2587.5	$\frac{21}{2}^- \rightarrow \frac{19}{2}^-$	7.01(11)	1.23(8) [3]	-	M1+E2
117.4	3937.3	$\frac{31}{2}^- \rightarrow \frac{29}{2}^-$	2.23(10)	0.85(7) [4]	-	M1+E2
133.9	1618.8	$\frac{15}{2}^- \rightarrow \frac{13}{2}^-$	2.08(6)	0.50(6) [2]	-	(M1)
143.4	4235.7	$\frac{35}{2}^- \rightarrow \frac{33}{2}^-$	1.09(4)	0.58(10) [5]	-	(M1+E2)
155.1	4092.3	$\frac{33}{2}^- \rightarrow \frac{31}{2}^-$	3.35(10)	0.65(6) [4]	-	M1+E2
171.3	4482.0	$\frac{37}{2}^- \rightarrow \frac{35}{2}^-$	2.63(10)	1.33(15) [2]	-	M1+E2
175.4	2303.8	$\frac{19}{2}^- \rightarrow \frac{17}{2}^-$	10.43(19)	1.35(5) [2]	-	M1+E2
198.4	3059.2	$\frac{25}{2}^- \rightarrow \frac{23}{2}^-$	7.36(16)	1.24(8) [2]	-	M1+E2

Table 5.1: Continued...

E_γ [1] (in keV)	E_i (in keV)	$J_i^\pi \rightarrow J_f^\pi$	I_γ	R_{DCO} (Err)	Δ_{IPDCO} (Err)	Deduced multipolarity
203.2	4513.2	$\frac{37}{2}^- \rightarrow \frac{35}{2}^-$	0.56(19)		-	M1+E2
215.3	3819.9	$\frac{29}{2}^- \rightarrow \frac{27}{2}^-$	5.49(39)	1.28(16) [2]	-	M1+E2
218.4	4310.7	$\frac{35}{2}^- \rightarrow \frac{33}{2}^-$	4.83(38)	1.40(19) [5]	-	M1+E2
236.5	5622.0	$\frac{45}{2}^- \rightarrow \frac{43}{2}^-$	0.21(3)	0.58(7) [5]		(M1+E2)
241.5	1725.6	$\frac{15}{2}^{(-)} \rightarrow \frac{13}{2}^-$	0.61(6)	-	-	(M1+E2)
244.6	4503.9	$\frac{31}{2}^- \rightarrow \frac{29}{2}^-$	0.96(7)	1.29(44) [3]	-	M1+E2
248.4	3386.7	$\frac{27}{2}^- \rightarrow \frac{25}{2}^-$	2.13(6)	1.33(28) [3]	-	M1+E2
251.6	5386.0	$\frac{43}{2}^- \rightarrow \frac{41}{2}^-$	0.45(4)	1.38(30) [5]		M1+E2
256.7	3902.9	$\frac{27}{2}^- \rightarrow \frac{25}{2}^-$	1.33(4)	0.87(15) [3]	-	M1+E2
263.4	5392.1	$\frac{43}{2}^- \rightarrow \frac{41}{2}^-$	0.62(6)	1.38(18) [5]	-	M1+E2
268.4	3826.5	$\frac{31}{2}^- \rightarrow \frac{29}{2}^-$	2.02(11)	0.61(9) [2]	-0.09(13)	M1+E2
273.3	2860.8	$\frac{23}{2}^- \rightarrow \frac{21}{2}^-$	19.76(5)	1.80(6) [3]	-0.15(4)	M1+E2
277.5	3138.3	$\frac{25}{2}^- \rightarrow \frac{23}{2}^-$	4.24(15)	1.62(22) [3]	-0.24(6)	M1+E2
278.0	4370.0	$\frac{35}{2}^- \rightarrow \frac{33}{2}^-$	1.38(8)	0.82(9) [4]	-0.15(3)	M1+E2
284.6	5342.5	$\frac{39}{2}^- \rightarrow \frac{37}{2}^-$	0.23(4)	1.62(22) [6]	-	M1+E2
289.0	4802.0	$\frac{39}{2}^- \rightarrow \frac{37}{2}^-$	2.55(14)	0.64(7) [7]		(M1+E2)
292.8	1484.1	$\frac{13}{2}^- \rightarrow \frac{13}{2}^-$	2.52(11)	1.37(27) [2]	-0.23(12)	M1+E2
296.1	4586.7	$\frac{35}{2}^- \rightarrow \frac{33}{2}^-$	1.11(11)	0.77(18) [3]	-	(M1+E2)
297.2	4779.2	$\frac{39}{2}^- \rightarrow \frac{37}{2}^-$	1.70(15)	1.37(23) [4]	-0.06(6)	M1+E2
305.2	2030.5	$\frac{15}{2}^- \rightarrow \frac{13}{2}^+$	4.63(20)	0.59(11) [4]	0.22(4)	E1

Table 5.1: Continued...

E_γ [1] (in keV)	E_i (in keV)	$J_i^\pi \rightarrow J_f^\pi$	I_γ	R_{DCO} (Err)	Δ_{IPDCO} (Err)	Deduced multipolarity
305.9	1924.7	$\frac{17}{2}^- \rightarrow \frac{15}{2}^-$	2.04(11)	1.57(19) [2]	-0.07(7)	M1+E2
311.2 [8]	2931.5	$\frac{23}{2}^- \rightarrow \frac{21}{2}^-$	7.30(29)	1.59(29) [7]	- 0.22(5)	M1+E2
312.3 [8]	3604.6	$\frac{27}{2}^- \rightarrow \frac{25}{2}^-$	2.19(17)			M1+E2
313.3	1190.2	$\frac{13}{2}^- \rightarrow \frac{11}{2}^-$	35.55(68)	1.60(10) [6]	-0.13(3)	M1+E2
316.5	2620.3	$\frac{21}{2}^- \rightarrow \frac{19}{2}^-$	16.61(38)	1.37(19) [7]	-0.16(5)	M1+E2
320.0	4802.0	$\frac{39}{2}^- \rightarrow \frac{37}{2}^-$	0.83(10)			(M1+E2)
325.0	4828.7	$\frac{33}{2}^- \rightarrow \frac{31}{2}^-$	0.11(5)	1.20(27) [2]	-	(M1+E2)
331.2	5133.0	$\frac{41}{2}^- \rightarrow \frac{39}{2}^-$	0.56(7)	0.52(6) [5]		(M1)
333.9	3937.3	$\frac{31}{2}^- \rightarrow \frac{27}{2}^-$	0.34(25)	-	-	(E2)
342.0	2486.5	$- \rightarrow -$	4.29(20)	-		-
347.8	3734.5	$\frac{29}{2}^- \rightarrow \frac{27}{2}^-$	1.07(21)	1.22(20) [3]	-	(M1+E2)
349.7	5128.9	$\frac{41}{2}^- \rightarrow \frac{39}{2}^-$	1.00(19)	1.80(21) [5]	-0.08(9)	M1+E2
354.0	5133.0	$\frac{41}{2}^- \rightarrow \frac{39}{2}^-$	0.43(7)	-	-	(M1+E2)
356.0	4258.9	$\frac{29}{2}^- \rightarrow \frac{27}{2}^-$	0.96(16)	1.74(36) [2]	-	M1+E2
360.8	3292.3	$\frac{25}{2}^- \rightarrow \frac{23}{2}^-$	7.67(22)	1.86(14) [2]	-0.04(7)	M1+E2
393.2	2011.8	$\frac{17}{2}^- \rightarrow \frac{15}{2}^-$	7.42(23)	1.64(10) [2]	-0.15(6)	M1+E2
394.2	876.9	$\frac{11}{2}^- \rightarrow \frac{9}{2}^-$	100.0(91)	1.27(16) [10]	-0.05(2)	M1+E2
401.8	3558.1	$\frac{29}{2}^- \rightarrow \frac{27}{2}^-$	6.97(21)	1.21(8) [2]	-0.12(6)	M1+E2
411.4	2030.5	$\frac{15}{2}^- \rightarrow \frac{15}{2}^-$	6.37(21)	1.17(7) [2]	-0.03(6)	(M1+E2)
418.5	2036.5	$\frac{15}{2}^- \rightarrow \frac{15}{2}^-$	2.86(17)	0.71(8) [2]	-0.04(8)	(M1+E2)

Table 5.1: Continued...

E_γ [1] (in keV)	E_i (in keV)	$J_i^\pi \rightarrow J_f^\pi$	I_γ	R_{DCO} (Err)	Δ_{IPDCO} (Err)	Deduced multipolarity
420.1	2144.5	$-\rightarrow\frac{13}{2}^+$	3.42(25)	-	-	-
421.0	4513.0	$\frac{37}{2}^-\rightarrow\frac{35}{2}^-$	0.49(5)	-	-	(E2)
428.6	1618.8	$\frac{15}{2}^-\rightarrow\frac{13}{2}^-$	24.60(42)	1.20(10) [10]	-0.11(2)	M1+E2
458.5	2470.3	$\frac{19}{2}^-\rightarrow\frac{17}{2}^-$	31.19(52)	3.22(16) [7]	-0.10(2)	M1+E2
464.1	4290.6	$\frac{33}{2}^-\rightarrow\frac{31}{2}^-$	2.95(23)	2.28(25) [2]	-0.13(5)	M1+E2
468.0	4779.0	$\frac{39}{2}^-\rightarrow\frac{35}{2}^-$	1.21(24)	1.03(34) [4]		(E2)
471.2	5057.9	$\frac{37}{2}^-\rightarrow\frac{35}{2}^-$	2.02(16)	-	-	(M1+E2)
471.7	3059.2	$\frac{25}{2}^-\rightarrow\frac{21}{2}^-$	1.91(25)	0.96(10) [2]	0.04(8)	E2
491.0	4802.0	$\frac{39}{2}^-\rightarrow\frac{35}{2}^-$	0.84(27)			(E2)
492.8	2620.3	$\frac{21}{2}^-\rightarrow\frac{17}{2}^-$	3.55(15)	1.01(16) [2]	0.19(5)	E2
527.7	2011.8	$\frac{17}{2}^-\rightarrow\frac{13}{2}^-$	2.74(18)	1.01(12) [11]	0.15(8)	E2
527.8	3819.9	$\frac{29}{2}^-\rightarrow\frac{25}{2}^-$	0.91(8)	0.95(15) [4]	0.06(5)	E2
535.4	1724.4	$\frac{13}{2}^+\rightarrow\frac{13}{2}^-$	4.59(22)	0.66(6) [2]	0.17(6)	E1
545.7	2470.3	$\frac{19}{2}^-\rightarrow\frac{17}{2}^-$	4.30(19)	2.61(58) [12]	-0.03(7)	M1+E2
552.8	2036.9	$\frac{15}{2}^-\rightarrow\frac{13}{2}^-$	5.05(19)	0.55(12) [4]	-0.16(5)	M1
563.2	3424.0	$\frac{25}{2}^-\rightarrow\frac{23}{2}^-$	4.0(22)	1.20(14) [2]	-0.09(11)	(M1+E2)
570.0	4829.0	$\frac{33}{2}^-\rightarrow\frac{29}{2}^-$	0.10(8)	-	-	(E2)
575.7	2587.4	$\frac{21}{2}^-\rightarrow\frac{17}{2}^-$	7.15(24)	0.93(4) [3]	0.14(6)	E2
601.0	4504.0	$\frac{31}{2}^-\rightarrow\frac{27}{2}^-$	0.61(17)	-	-	(E2)
607.2	1484.1	$\frac{13}{2}^-\rightarrow\frac{11}{2}^-$	26.94(66)	1.71(17) [4]	-0.03(2)	M1+E2

Table 5.1: Continued...

E_γ [1] (in keV)	E_i (in keV)	$J_i^\pi \rightarrow J_f^\pi$	I_γ	R_{DCO} (Err)	Δ_{IPDCO} (Err)	Deduced multipolarity
611.9	4260.9	$\frac{29}{2}^- \rightarrow \frac{25}{2}^-$	0.56(14)	1.01(13) [5]	-	(E2)
613.3	5392.1	$\frac{43}{2}^- \rightarrow \frac{41}{2}^-$	1.90(16)	-	-	(E2)
627.7	2931.5	$\frac{23}{2}^- \rightarrow \frac{19}{2}^-$	6.82(27)	0.99(9) [2]	0.12(11)	E2
647.3	5128.9	$\frac{41}{2}^- \rightarrow \frac{37}{2}^-$	2.52(25)	1.07(18) [5]	0.06(11)	E2
663.1	2587.5	$\frac{21}{2}^- \rightarrow \frac{17}{2}^-$	8.06(26)	0.97(6) [2]	0.11(3)	E2
670.2	3826.5	$\frac{31}{2}^- \rightarrow \frac{27}{2}^-$	4.11(21)	1.10(9) [3]	0.08(7)	E2
672.2	3296.2	$\frac{25}{2}^- \rightarrow \frac{21}{2}^-$	10.9(14)	0.97(10) [13]	0.10(5)	E2
673.1	3604.6	$\frac{27}{2}^- \rightarrow \frac{23}{2}^-$	2.97(14)	1.01(5) [4]	0.10(4)	E2
700.0	4259.1	$\frac{29}{2}^- \rightarrow \frac{29}{2}^-$	0.27(5)	-	-	(M1+E2)
702.0	4436.5	$\frac{31}{2}^- \rightarrow \frac{29}{2}^-$	0.69(40)	1.44(12) [3]	-0.12(12)	M1+E2
707.5	1190.2	$\frac{13}{2}^- \rightarrow \frac{9}{2}^-$	58.6(15)	1.02(2) [3]	0.16(3)	E2
708.1	3178.4	$\frac{23}{2}^- \rightarrow \frac{19}{2}^-$	4.99(74)	1.01(14) [2]	-	(E2)
732.3	4290.6	$\frac{33}{2}^- \rightarrow \frac{29}{2}^-$	0.77(10)	0.99(15) [3]	0.09(9)	E2
734.5	1924.7	$\frac{17}{2}^- \rightarrow \frac{13}{2}^-$	27.67(54)	0.99(11) [12]	0.11(7)	E2
741.7	1618.8	$\frac{15}{2}^- \rightarrow \frac{11}{2}^-$	27.18(51)	0.97(7) [5]	0.06(3)	E2
755.6	5342.5	$\frac{39}{2}^- \rightarrow \frac{35}{2}^-$	1.74(17)	1.01(11) [2]	0.10(7)	E2
760.8	4586.7	$\frac{35}{2}^- \rightarrow \frac{31}{2}^-$	2.44(19)	1.10(7) [2]	0.13(5)	E2
767.3	5057.9	$\frac{37}{2}^- \rightarrow \frac{33}{2}^-$	1.11(12)	1.05(13) [2]	0.08(7)	E2
786.4	3647.2	$\frac{25}{2}^- \rightarrow \frac{23}{2}^-$	0.71(16)	1.90(26) [2]	-0.08(6)	M1+E2
821.6	2011.8	$\frac{17}{2}^- \rightarrow \frac{13}{2}^-$	25.35(49)	1.09(2) [2]	0.10(3)	E2

Table 5.1: Continued...

E_γ [1] (in keV)	E_i (in keV)	$J_i^\pi \rightarrow J_f^\pi$	I_γ	R_{DCO} (Err)	Δ_{IPDCO} (Err)	Deduced multipolarity
834.2	4660.7	$\frac{33}{2}^- \rightarrow \frac{13}{2}^-$	2.51(32)	1.75(15) [2]	-0.12(19)	M1+E2
840.3	2030.5	$\frac{15}{2}^- \rightarrow \frac{13}{2}^-$	20.74(51)	1.12(3) [2]	-0.11(3)	M1+E2
844.1	3903.9	$\frac{27}{2}^- \rightarrow \frac{25}{2}^-$	1.54(36)	1.66(24) [10]	-0.20(9)	M1+E2
846.7	2036.5	$\frac{15}{2}^- \rightarrow \frac{13}{2}^-$	24.18(71)	2.24(6) [2]	-0.03(2)	M1+E2
847.5	1724.4	$\frac{13}{2}^+ \rightarrow \frac{11}{2}^-$	22.3(12)			E1 [15]
852.3	2470.3	$\frac{19}{2}^- \rightarrow \frac{15}{2}^-$	8.22(23)	0.93(10) [7]	0.11(5)	E2
896.0	2380.1	$\frac{17}{2}^- \rightarrow \frac{13}{2}^-$	2.68(18)	1.03(19) [2]	0.02(7)	(E2)
1041.2	3902.9	$\frac{27}{2}^- \rightarrow \frac{23}{2}^-$	1.09(18)	1.05(27) [2]	0.18(8)	E2
1067.7	1944.9	$\frac{13}{2}^- \rightarrow \frac{11}{2}^-$	0.46(29)	-	-	M1, E2 [15]
1161.6	2038.5	$(\frac{15}{2}^+) \rightarrow \frac{11}{2}^-$	1.00(12)	-	-	(M2, E3) [15]
1190.5	2380.1	$\frac{17}{2}^- \rightarrow \frac{13}{2}^-$	1.09(14)	1.03(39) [2]	0.07(10)	E2

[1] Gamma energies accurate to ±0.3 keV unless otherwise indicated.
[2] From 707.5 keV (E2) DCO gate.
[3] From 821.6 keV (E2) DCO gate.
[4] From 627.7 keV (E2) DCO gate.
[5] From 672.2 keV (E2) DCO gate.
[6] From 734.5 keV (E2) DCO gate.
[7] From 741.7 keV (E2) DCO gate.
[8] Combined intensity, DCO and IPDCO ratio.
[10] From 663.1 keV (E2) DCO gate.
[11] From 576.1 keV (E2) DCO gate.
[12] From 761.0 keV (E2) DCO gate.
[13] From 527.7 keV (E2) DCO gate.
[15] Adopted from Ref. [30].

5.4 Discussion

The proton Fermi level for the Tl isotopes lies below the Z = 82 shell closure near $3s_{1/2}$ and $2d_{3/2}$ orbitals and neutron Fermi level lies close to the $1i_{13/2}$, $3p_{3/2}$ and $2f_{5/2}$ orbitals. The proton $h_{9/2}$ orbital comes down in energy with oblate deformation in lighter thallium isotopes in mass A $\sim$ 190 region. Therefore the observation of band structure above the $9/2^-$ isomeric state in lighter thallium isotopes has been interpreted as band based on proton [505]9/2 Nilsson orbital upto ^{201}Tl. Apart from this band, theoretical calculation done by Toki et al., [7], predicted $15/2^-$ and $17/2^-$ states in ^{195,197}Tl which are not member of $9/2^-$ band. Experimentally we have been able to identify $(15/2^-)$ and $17/2^-$ states at excitation energies 1726 and 2380 keV respectively. These states lie closer to the theoretically predicted states based on triaxial rotor-plus-particle model [5, 6].

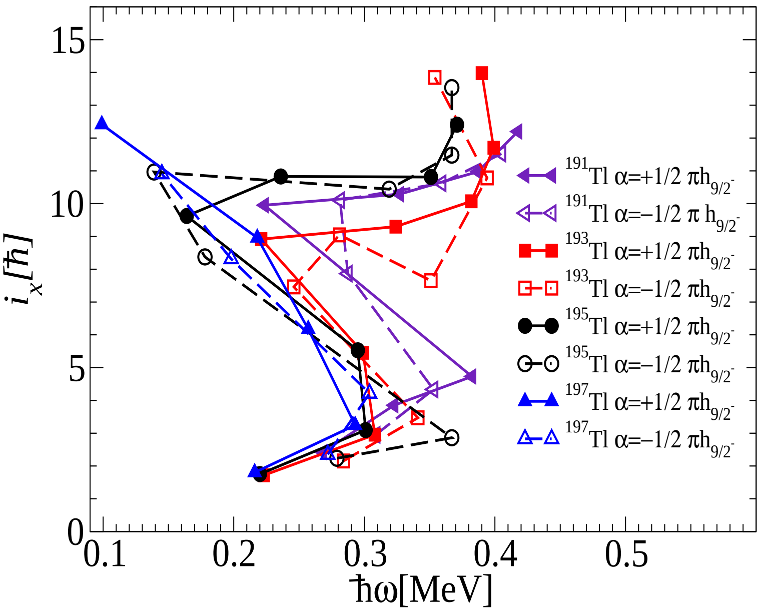

Figure 5.11: Experimental alignment (i_x) as a function of rotational frequency $\hbar\omega$ for the ground state band of ^{195}Tl has been compared with the neighbouring odd (A) Tl isotopes for positive signature (α=+1/2 by filled symbol) and negative signature partners (α=-1/2 by unfilled symbol), respectively. The Harris reference parameters are taken as J_0= 8 $\hbar^2 MeV^{-1}$ and J_1=40$\hbar^4 MeV^{-3}$.

5.4.1 Bands: B1-B2

The band based on $\pi h_{9/2}$ orbital in odd-A $^{189-193}$Tl isotopes has been observed beyond the band crossing [11, 12]. In the present thesis work this band has been extended upto spin 39/2$^-$ with the observation of band B2. The alignment (i_x) for bands B1 and B2 in ^{195}Tl observed in the present work are shown in Figure. (5.11) as a function of rotational frequency $\hbar\omega$, along those of the neighbouring isotopes ^{191}Tl, ^{193}Tl and ^{197}Tl. The initial alignment for band based on $\pi h_{9/2}$ orbital for all the four isotopes are very similar. The experimental band crossing for positive (α=$\frac{1}{2}$) signature partner band for

^{191}Tl, ^{193}Tl, ^{195}Tl and ^{197}Tl take place at rotational frequencies $\hbar\omega \sim$ 0.38, 0.31, 0.30 and 0.29 MeV, respectively. Whereas the band crossing for negative (α=-$\frac{1}{2}$) signature partner band for these isotopes takes place at rotational frequencies $\hbar\omega \sim$ 0.35, 0.34, 0.36 and 0.30 MeV, respectively. In spite of difference in crossing frequencies, the gain in alignment ($\triangle i_x \simeq 7\hbar$ for ^{191,193}Tl and $\triangle i_x \simeq 8\hbar$ for ^{195}Tl) and after the band crossing are seen to be very similar for both signature partner bands in ^{191,193,195}Tl isotopes. The first band crossing observed in ^{191}Tl and ^{193}Tl isotopes were interpreted as alignment of a $i_{\frac{13}{2}}$ neutron pair [11, 12]. Similarly the observed band crossing of band B1 in ^{195}Tl can be attributed to the alignment in $\nu i_{13/2}$ orbital. Therefore, the configuration of the higher lying states in band B2 and B2a (above 2588 keV) would be $\pi h_{9/2} \otimes \nu i^{-2}_{13/2}$.

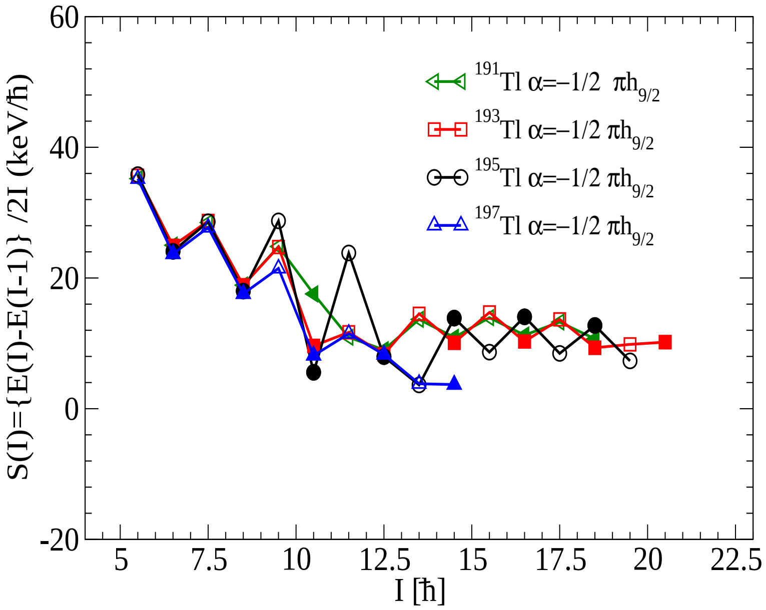

Figure 5.12: The energy staggering S(I)=[E(I)-E(I-1)]/2I as a function of spin(I) for the ground state band (before and after first band crossing) of ^{195}Tl has been compared with neighbouring odd (A) Tl isotopes. For ^{195}Tl, signature inversion observed at spin $\frac{27}{2}^-$ where filled symbol correspond to α=+1/2 and unfilled symbol represents α=-1/2.

The energy staggering plot in terms of S(I) = [E(I)−E(I−1)]/2I, where E(I) is the energy of the state with spin I, has been plotted for odd-A $^{191-197}$Tl isotopes as a function of spin(I) in Figure. (5.12). The signature of the favoured and unfavoured states is defined as [33]

$$\alpha_f = \frac{1}{2}(-1)^{j-1/2} \qquad \alpha_u = \frac{1}{2}(-1)^{j+1/2} \tag{5.3}$$

where the angular momentum of the odd particle is expressed by j. Here $\alpha = +1/2$ is the favoured signature for $\pi h_{9/2}$ band in odd-A Tl isotopes. After first band crossing the band configuration changes to $\pi h_{9/2} \otimes \nu i^{-2}_{13/2}$ for ^{191,193,195}Tl isotopes. This makes $\alpha = -1/2$ as the favoured signature when the proton is in $h_{9/2}$ orbital and neutron pair breaking take place in $i_{13/2}$ orbital in compliance with the following Eq.

$$\alpha_f = \frac{1}{2}\sum_i (-1)^{j_i-1/2} \tag{5.4}$$

where j_i as the qp angular momentum.

Therefore a signature inversion is expected after the neutron pair alignment. A signature inversion is indeed obtained at spin $27/2^-$ in ^{195}Tl with neutron number N = 112. But there is no indication of signature inversion in ^{191,193}Tl isotopes with N = 110, 112. In ^{197}Tl similar signature inversion appears at spin $27/2^-$ but there is no high spin experimental data beyond this spin state. Therefore it will be interesting to see what happens to energy staggering after $27/2^-$ states in ^{197}Tl. The signature inversion has been interpreted in terms of Coriolis effect [33–35] for spins I$\lesssim j_\pi + j_\nu$, triaxial shape [36] and interplay of residual p-n interaction [37, 38] in this mass region. So detail theoretical calculation is required to understand this signature inversion in odd-A Tl isotopes for neutron number $N \geq 114$.

5.4.2 Sequnce: B3

The irregular sequence observed in the present study does not show any rotational structure. These states lie close to the neutron pair breaking in ^{195}Tl where numerous shell model states are available near the neutron Fermi level. Therefore, it is quite possible for them to be generated because of single particle excitation in this region. Whereas detail shell model calculation need to be done to asserting the nature of this sequence.

5.4.3 Band: B4

From the excitation energy of the negative parity band above 2031 keV level in ^{195}Tl appears to be based on 3-qp configuration. In the neighbouring even-even Hg nuclei similar negative parity bands have been interpreted as a coupling of two unpaired neutron in $i_{13/2}$ and low j $p_{3/2}$ or $f_{5/2}$ orbital [17, 39].

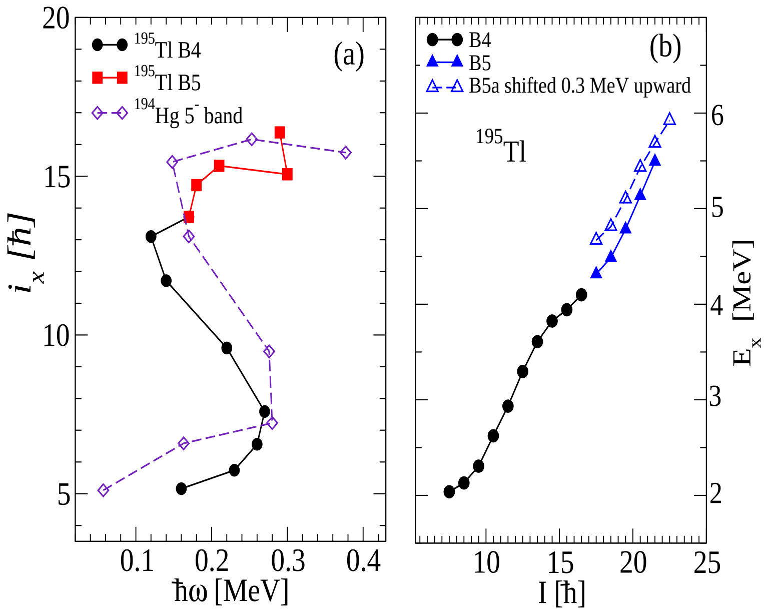

Figure 5.13: The schematic representation of (a) comparison in alignment (i_x) vs rotational frequency ($\hbar\omega$) for bands B4-B5 of ^{195}Tl along with 5^- band of ^{194}Hg with rotational reference Harris parameters J_0= 8 $\hbar^2 MeV^{-1}$ and J_1=40$\hbar^4$MeV^{-3}. (b) Excitation energy (E_x) vs spin(I) for bands B4-B5 and B5a. The band B5 becomes degenerate with band B5a after first band crossing. The band B5a has been shifted upward by 0.3 MeV for viewing convenience.

The alignment pattern for the band B4 and B5 in ^{195}Tl is quite similar to the 5^- band in its immediate even-even neighbour ^{194}Hg nucleus as shown in Figure. (5.13)(a). The alignment of this band in ^{194}Hg was interpreted as a coupling of fully aligned $i_{13/2}$ neutron with a poorly aligned low-j ($p_{3/2}$) neutron [17]. The gain in alignment for these bands in ^{194}Hg and ^{195}Tl is $\triangle i_x \sim 9\hbar$. The similarity of i_x (before band crossing) for 5^- band in ^{194}Hg with bands B4 in ^{195}Tl indicate that their intrinsic structures are quite similar. Since most of the angular momentum contribution comes from the neutron configurations, the contribution from the odd proton is very small which is quite possible as the odd proton occupies high Ω orbital of $h_{9/2}$ or $i_{13/2}$ in case of oblate deformation. Considering the negative parity of the band B4 in ^{195}Tl, the intrinsic configuration of this band head can be assigned as $\pi i_{13/2} \otimes \nu i_{13/2}^{-1}(p_{3/2}f_{5/2})^{-1}$ which, after band crossing attains $\pi i_{13/2} \otimes \nu i_{13/2}^{-3}(p_{3/2}f_{5/2})^{-1}$ configuration. Also the presence of 305 keV (E1) (see Figure. (5.5)) transition from the $15/2^{-}$ state to $\pi i_{13/2}$ state at 1724 keV justifies this assignment [30].

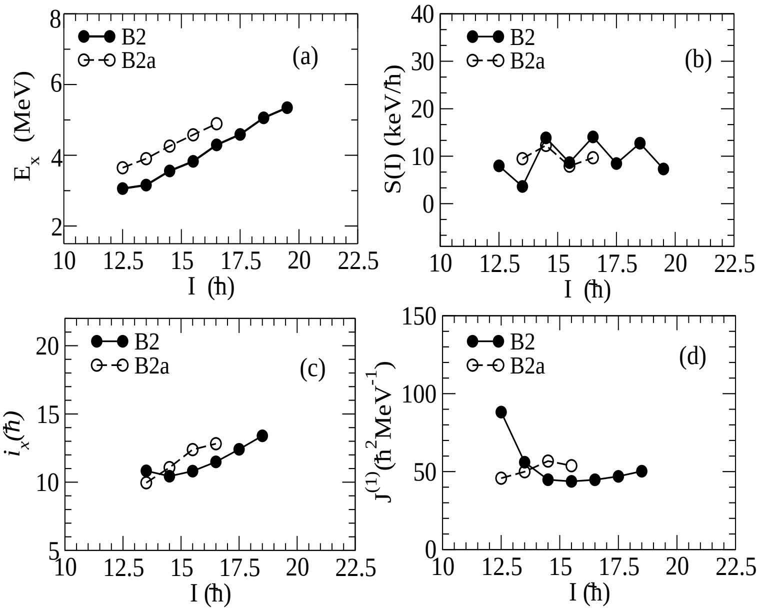

Figure 5.14: Comparative study of various experimental parameters belonging to band B2 and B2a. (a) Excitation energy(E_x) of the two bands maintains similar energy difference over the entire spin(I) range. (b) Energy staggering S(I)=[E(I)-E(I-1)]/2I for bands B2 and B2a is almost spin(I) independent. (c) The variation in alignment (i_x) with spin(I) for bands B2 and B2a, deduced with Harris reference parameters as J_0= 8 $\hbar^2 MeV^{-1}$ and J_1=40$\hbar^4 MeV^{-3}$. (d) The kinetic moment of inertia $J^{(1)}$ for bands B2 and B2a.

5.4.4 Bands: B2-B2a

The band B2 and B2a maintains average relative excitation energy $\triangle$E $\sim$ 677 keV in the spin range $\frac{25}{2}^{-} \leq I \leq \frac{33}{2}^{-}$ as shown in Figure. (5.14)(a). The similarity in alignment (i_x) value and several interconnecting transitions from band B2a to B2 indicates them to have similar configuration. The energy staggering S(I) of band B2a is much reduced with respect to band B2 while they are in similar phase over the spin(I) range as shown in Figure. (5.14)(b). The measured quasi-particle alignments ($\triangle i_x$) and kinetic moment of inertia (J$^{(1)}$) of these two bands are very similar as shown in Figure. (5.14)].

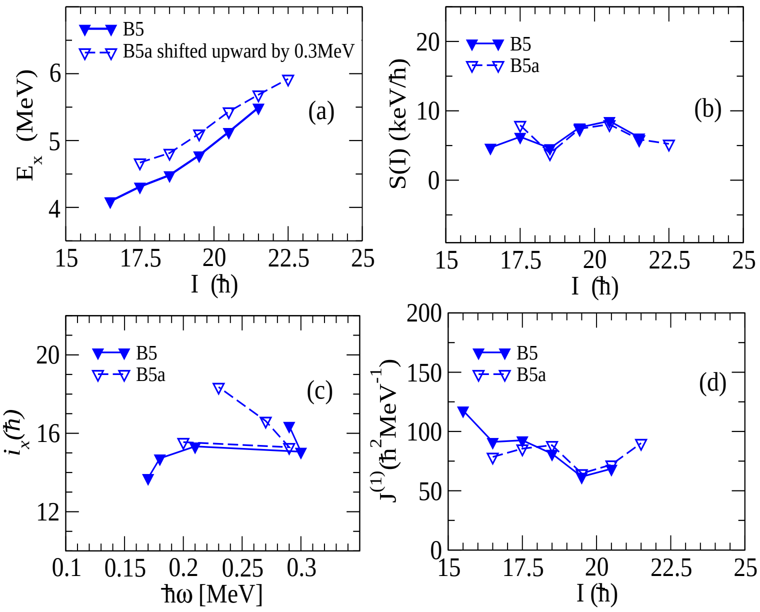

Figure 5.15: Comparison of various experimental parameters of band B5 and B5a. (a) The excitation energy of band B5 and B5a is quite degenerate therefore B5a excitation energy is shifted 0.3 MeV upwards for viewing convenience. (b) Energy staggering S(I)=[E(I)-E(I-1)]/2I for bands B5 and B5a is seen to be independent of spin(I). (c) Comparison in alignment (i_x) vs rotational frequency ($\hbar\omega$) for bands B5 and B5a of ^{195}Tl with rotational reference Harris parameters $J_0= 8\ \hbar^2 MeV^{-1}$ and J_1=40$\hbar^4$MeV^{-3}. (d)The kinetic moment of inertia $J^{(1)}$ for bands B5 and B5a.

5.4.5 Bands: B5-B5a

The band B4 after neutron pair alignment has been drawn in the present level scheme (see Figure. (5.5)) as band B5. The side band B5a is connected to the former with several interconnecting transitions. The band head spin-parity of B5a is decided by the DCO and IPDCO ratio of 278 keV transition. Therefore, the bands B5 and B5a have similar parity. The excitation energy (E_x) is quite similar for both of these bands as shown in

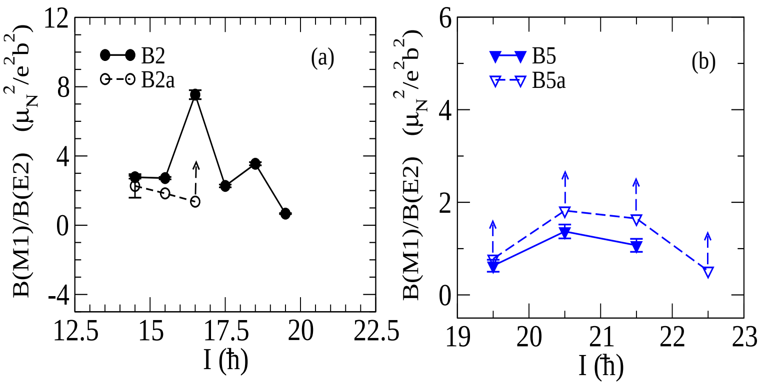

Figure 5.16: Plots of experimentally obtained transition probabilities (a) B(M1)/B(E2) ratio for bands B2 and B2a (b)B(M1)$_{in}$/B(M1)$_{out}$ ratio for bands B5 and B5a.

Figure. (5.15). The excitation energy of band B5a is higher than band B5 at spin $35/2^{-}$ by 59 keV which reduces to -6 keV at spin $43/2^{-}$. The similarity in excitation energy of these B5 and B5a bands, indicates them to be build on similar configuration.

The energy staggering (S(I)) parameter indicator of Coriolis coupling, is independent of spin(I) for both bands B5 and B5a as shown in Figure. (5.15)(b). This indicates that quasi-particle angular momentum is perpendicular to the core rotational angular momentum. The similarity of aligned angular momentum ($\triangle i_x$) and kinetic moment of inertia (J$^{(1)}$) of these two bands shown in Figure. (5.15)(c)-(d) lends further support on their similar configuration.

The B(M1)/B(E2) transition probability ratios for bands B2-B2a and B5-B5a are shown in Figure. (5.16)(a)-(b). For bands B2-B2a this ratio is quite identical apart from spin $33/2^{-}$. The crossover E2 transition for the above stated spin in band B2a is very weak, therefore only the lower limit of the B(M1)/B(E2) ratios could be obtained. This similarity of B(M1)/B(E2) transition probability ratios for bands B2 and B2a indicates them to based on the same configuration ($\pi h_{9/2} \otimes \nu i_{13/2}^{-2}$). In band B5a we could not identify any crossover E2 transitions. So considering the higher limit of the intensity of the unobserved crossover E2 transitions as the level of background in the data, the lower limit of the B(M1)/B(E2) ratio has been estimated for band B5a. But the trend of these ratios for band B5 and B5a are quite identical. This further establishes band B4 after band crossing have identical configuration i.e., $\pi i_{13/2} \otimes i_{13/2}^{-3}(p_{3/2}f_{5/2})^{-1}$ with band B5a.

The details of all the bands belonging to ^{195}Tl and their respective configurations except sequence B3 are given in Table. 5.2.

Table 5.2: Different bands and their proposed configurations in ^{195}Tl.

Name of Band	Number of quasi-particle	Configuration
B1	1 qp	$\pi h_{9/2}$
B2	3 qp	$\pi h_{9/2} \otimes \nu i_{13/2}^{-2}$
B2a	3 qp side band of B2	$\pi h_{9/2} \otimes \nu i_{13/2}^{-2}$
B4	3 qp	$\pi i_{13/2} \otimes \nu i_{13/2}^{-1}(p_{3/2}f_{5/2})^{-1}$
B5	5 qp	$\pi i_{13/2} \otimes \nu i_{13/2}^{-3}(p_{3/2}f_{5/2})^{-1}$
B5a	5 qp side band of B5	$\pi i_{13/2} \otimes \nu i_{13/2}^{-3}(p_{3/2}f_{5/2})^{-1}$

5.4.6 Systematics comparison of degenerate bands with neighbouring odd-odd Tl isotopes

The excellent near degeneracy of 3qp bands B2-B2a and in particular the 5qp bands B5 (after first band crossing above B4)-B5a in ^{195}Tl has been compared with degenerate bands

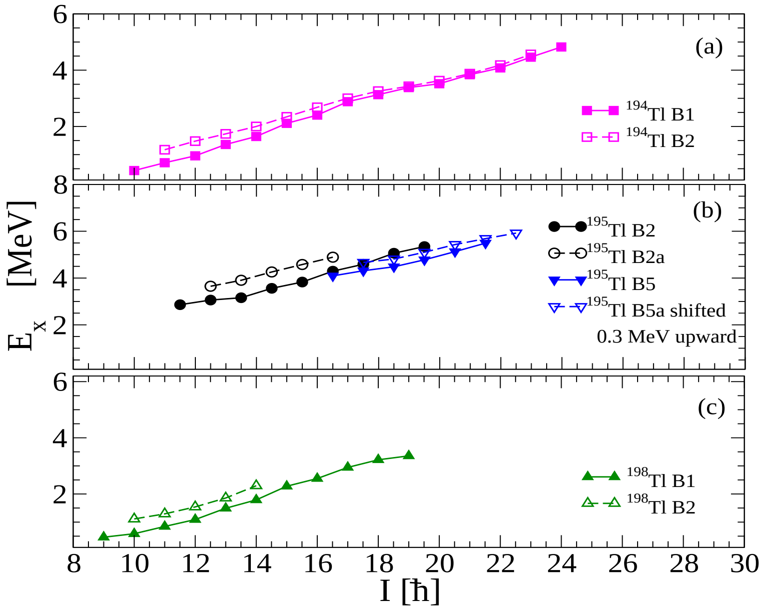

Figure 5.17: Comparison of excitation energy (E_x) as a function of spin (I) for doubly degenerate bands in ^{194,195,198}Tl isotopes.

based on 2-qp configuration in ^{198}Tl and 4-qp configuration in ^{194}Tl and in Figures. (5.17)-(5.21).

The 4-qp bands in ^{194}Tl shows near degeneracy in the excitation energies with $\triangle$E not larger than 110 keV for the whole observed spin range of I = 19-23, reaching a value of $\triangle$E=37 keV at I=21 see Figure. (5.17),(a) The B2 and B2a bands of ^{195}Tl maintains average $\triangle$E = 677 keV whereas band B5 and B5a maintains continuous decreasing trend of energy separation of 59 keV to -6 keV from spin range I =3 $5/2^{-}$-$43/2^{-}$ as shown in Figure. (5.17)(b). In ^{198}Tl, degenerate 2qp bands maintains average $\triangle$E = 459 keV in the spin range of I = 10-14 (see Figure. (5.17)(c)). So bands B2 and B2a in ^{195}Tl maintains similar energy separation as degenerate bands in ^{198}Tl and bands B5 and B5a comes closer to each other with increasing spin as the degenerate bands observed in ^{194}Tl.

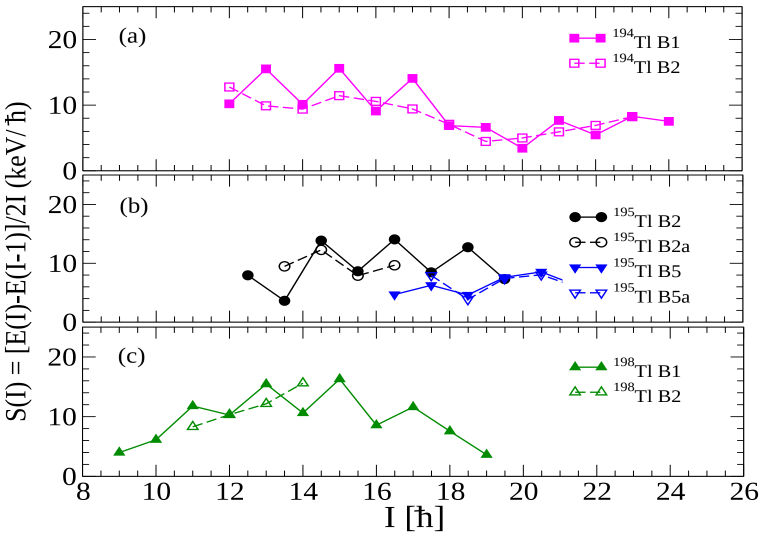

Figure 5.18: Comparison of energy staggering S(I)=[E(I)−E(I-1)]/2I as a function of spin (I) for ^{194,195,198}Tl isotopes.

Energy staggering S(I) for degenerate bands in ^{194}Tl and ^{195}Tl (B5-B5a) is independent of spin(I). Whereas the S(I) parameter for band B2 in ^{198}Tl and B2a in ^{195}Tl is quite independent of I as shown in Figure. (5.18).

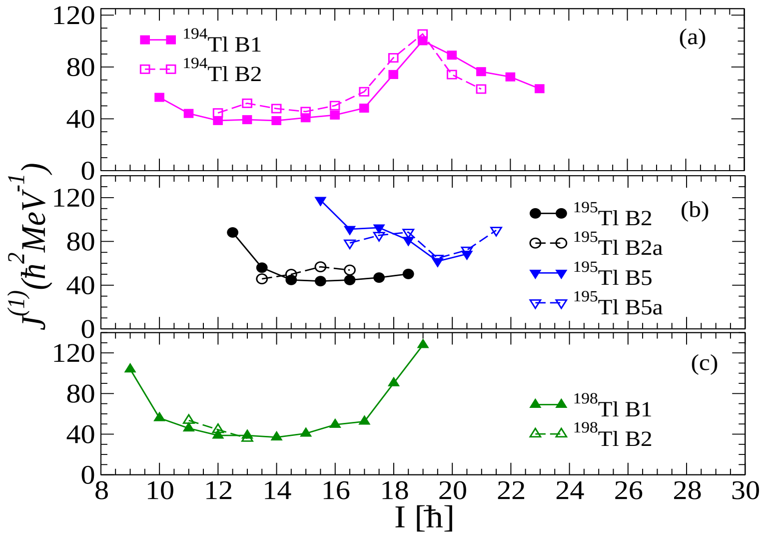

Figure 5.19: Comparison of kinetic moment of inertia $J^{(1)}$ as a function of spin (I) for ^{194,195,198}Tl isotopes.

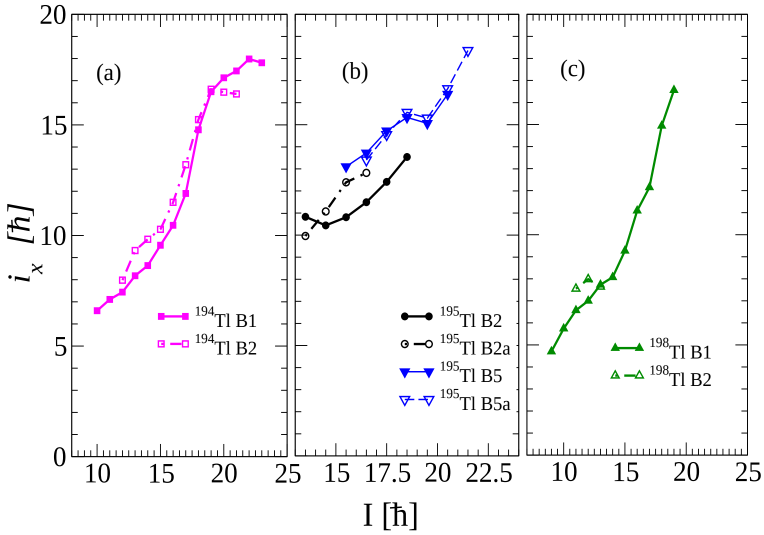

Figure 5.20: Comparison of alignment (i_x) as a function of spin (I) for ^{194,195,198}Tl isotopes with rotational Harris parameters $J_0 = 8\ \hbar^2 MeV^{-1}$ and $J_1 = 40\hbar^4 MeV^{-3}$.

The comparison of kinetic moment of inertia ($J^{(1)}$) and aligned angular momentum (i_x) for degenerate bands in ^{194,195,198}Tl isotopes shows identical behaviour with spin in Figures. (5.19)-(5.20).

The B(M1)/B(E2) ratio for bands B2-B2a and B5-B5a in ^{195}Tl matches quite well compared to degenerate bands in ^{194}Tl and ^{198}Tl isotopes as shown in Figure. (5.21). Therefore in all possible way B2-B2a and B5-B5a bands in ^{195}Tl appears to be degenerate with the previously reported degenerate bands in ^{194}Tl and ^{198}Tl isotopes in this mass region.

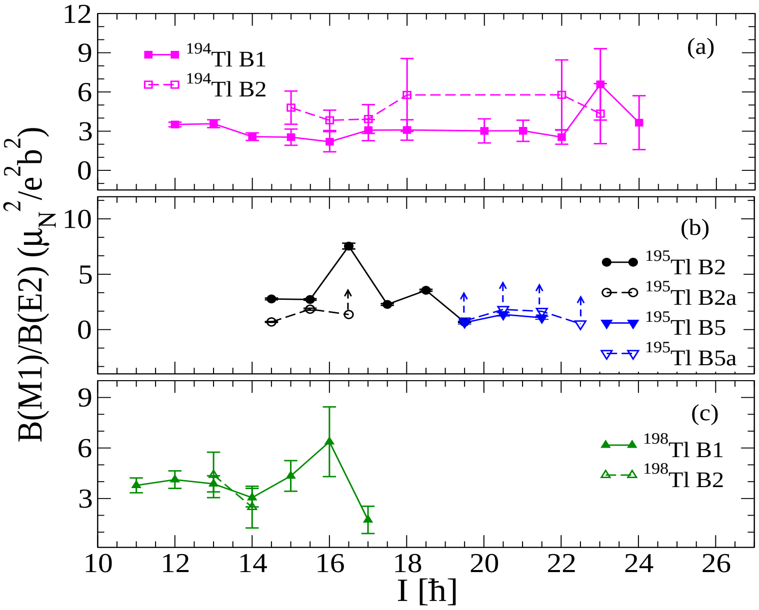

Figure 5.21: Comparison of B(M1)/B(E2) ratio with respect to spin (I) for ^{194,195,198}Tl isotopes in the case of doubly degenerate bands.

Pairs of near-degenerate partner bands built on particle and hole configuration above axially asymmetric nuclear deformation are most often interpreted as chiral symmetry candidates in the angular momentum space [40, 41]. In the chiral geometry the valence nucleons with particle (hole) angular momentum aligned along the short (long) nuclear axes and core rotational angular momentum is predominantly oriented along the intermediate nuclear axis. This three-dimensional orientation of the angular momenta of the odd nucleons and the collective rotation determines the chiral geometry of the system based on left-handed or a right-handed orientation of the three angular momenta. The nucleon configuration of the degenerate bands in ^{195}Tl have a valence proton of predominantly particle nature and valence neutron(s) with predominantly hole nature, thus forming a suitable nucleon configuration for chiral geometry formation. Furthermore there are several indications that the nuclear shape could be triaxial in this mass region. There is observation of near degenerate bands in ^{194,198}Tl isotopes [3, 4]. While in the former nucleus, first observation of four quasi-particle $\pi h_{9/2} \otimes \nu i_{13/2}^{-3}$ has been reported and in ^{198}Tl 2- quasi-particle bands based on $\pi h_{9/2} \otimes \nu i_{13/2}^{-1}$ configuration has been observed. Secondly, the theoretical Total Routhian Surface (TRS) calculation done based on $\pi h_{9/2} \otimes \nu i_{13/2}^{-2}$ and $\pi i_{13/2} \otimes \nu i_{13/2}^{-3}(\mathrm{p}_{3/2}\mathrm{f}_{5/2})^{-1}$ configurations shows the presence of triaxial minimum for these bands (see Table. 5.2), which further supports chiral geometry in angular momentum space (discussed in the following section).

Other very good candidate of multi quasi-particle chiral bands have been reported in ^{105}Rh [42] based on $\pi g_{9/2}^{-1} \otimes \nu h_{11/2}(g_{7/2}d_{5/2})$ configuration and in ^{135}Nd based on $\pi(g_{7/2}/g_{9/2}/h_{11/2}) \otimes \nu h_{11/2}^{2}$ [43, 44] configuration.

5.4.7 TRS calculations

In order to investigate the deformation driving effect of single- particle proton orbital above the Z = 82 shell closure and the effect of neutron $i_{13/2}$ orbitals (for the configurations under consideration) in determining the shape of ^{195}Tl, Total Routhian Surface (TRS) calculations have been performed. The TRS code of Nazarewicz et al. [45, 46] was used in these calculations. A deformed Woods-Saxon potential and BCS pairing was used to calculate the single-particle energies and the total energy of the system was obtained by employing the Strutinsky shell correction method. The universal parameter set was used for the Woods-Saxon potential and pairing calculations. The Routhian energies were calculated in (β_2, γ, β_4) deformation mesh points with minimization on hexadecapole deformation β_4. The procedure of such calculations have been outlined in Ref. [47]. The Routhian surfaces are plotted in the conventional $\beta_2 - \gamma$ plane. In these plots, $\gamma = 0^0$ ($\gamma = -60^0$) corresponds to prolate (oblate) shape.

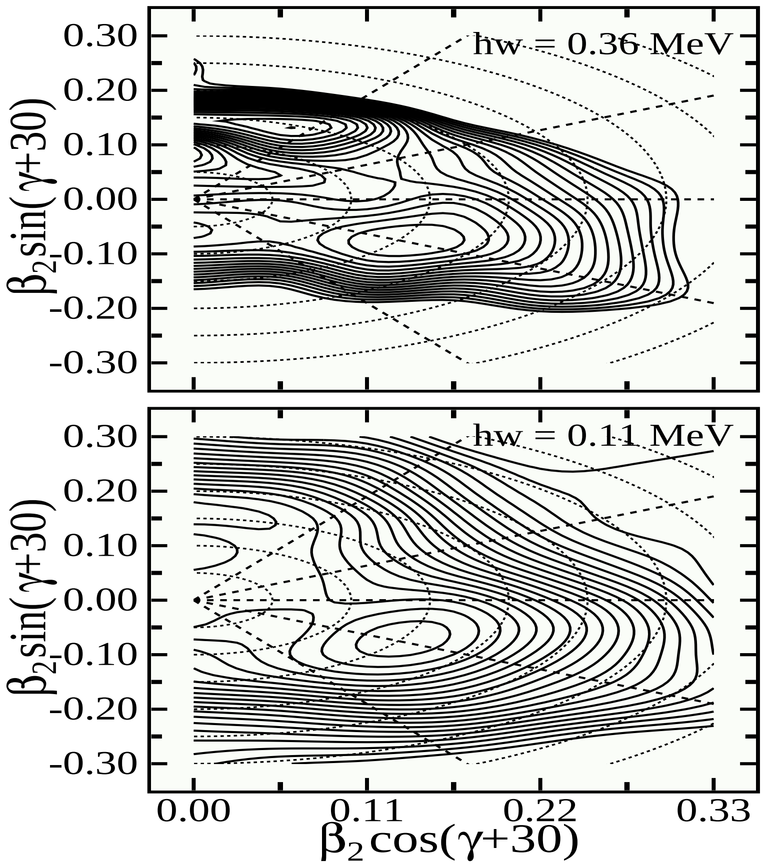

Figure 5.22: Contour plots for Total Routhian Surface (TRS) in the β_2-γ deformation mesh for the $\pi h_{9/2}$ configuration calculated at rotational frequency $\hbar\omega$=0.11 MeV and $\pi h_{9/2} \otimes \nu i_{13/2}^{-2}$ configuration at rotational frequency 0.36 MeV for bands B2 and B2a respectively. The contours are 250 keV apart.

The TRS calculation performed at $\hbar\omega$=0.11 MeV for the $\pi h_{9/2}$ configuration of band B1, shows a clear minimum at β_2=0.15 and γ=-58^0 as shown in the lower panel of Figure. (5.22) and this deformation persists over a rotational frequency up to first band crossing. Therefore the rotational band observed in ^{195}Tl based on this configuration is due to this oblate deformation as in other Tl isotopes in this mass region. As the rotational frequency increased upto $\hbar\omega$=0.36 MeV, a neutron pair alignment takes place and the TRS calculation based on $\pi h_{9/2} \otimes \nu i^{-2}_{13/2}$ configuration shows two deformed minimum in the contour plot, one at β_2=0.15 and γ=-58^0 with oblate deformation and the other one at β_2=0.15 and γ=39^0 with triaxial deformation as shown in the upper panel of Figure. (5.22). This triaxial minimum also gives the possibility of the nucleus to rotate around its intermediate axis.

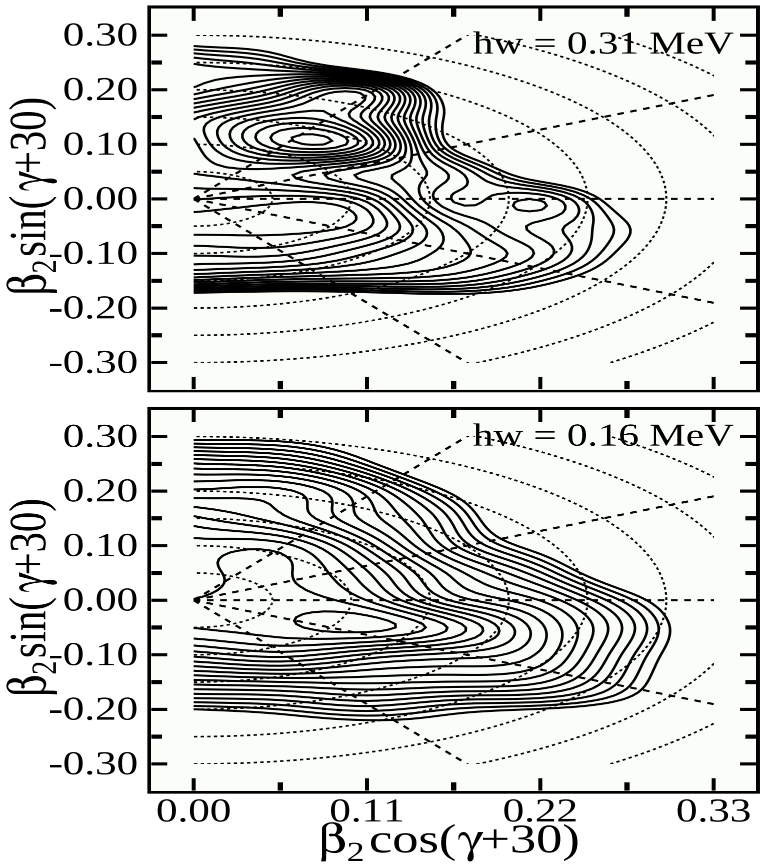

Figure 5.23: Contour plots for Total Routhian Surface (TRS) in the β_2-γ deformation mesh for the $\pi i_{13/2} \otimes \nu\ i^{-1}_{13/2}(p_{3/2}f_{5/2})^{-1}$ configuration calculated at rotational frequency $\hbar\omega$=0.16 for band B4 and $\pi i_{13/2} \otimes i^{-3}_{13/2}(p_{3/2}f_{5/2})^{-1}$ configuration at rotational frequency $\hbar\omega$= 0.31 MeV for band B5 and B5a, respectively. The contours are 250 keV apart.

The surfaces calculated for $\pi i_{13/2} \otimes \nu i^{-1}_{13/2}(\mathrm{p}_{3/2}\mathrm{f}_{5/2})^{-1}$ configuration at rotational frequency $\hbar\omega$=0.16 MeV for band B4, shows a oblate minimum at β_2=0.11 and γ=-55^0 in the lower panel in Figure. (5.23). This deformation persist upto neutron pair breaking and TRS calculation done at rotational frequency $\hbar\omega$=0.31 MeV for configuration $\pi i_{13/2}$ $\otimes i^{-3}_{13/2}(p_{3/2}f_{5/2})^{-1}$ a stable triaxial minimum appears at β_2=0.14 and γ=25^0 deformation as shown in the upper panel in Figure. (5.23). This further supports nuclear rotation about its intermediate axis. Therefore the TRS calculation done for the $\pi h_{9/2}$ and $\pi i_{13/2}$ $\otimes$ ν $i^{-1}_{13/2}(p_{3/2}f_{5/2})^{-1}$ configuration bands (B1, B4) after neutron pair alignment shows the presence of triaxial minimum.

So in the light of above discussions the bands B5 and B5a appears to be quite degenerate with configuration $\pi i_{13/2} \otimes \nu i^{-3}_{13/2}(p_{3/2}f_{5/2})^{-1}$, similar to the 4-qp degenerate bands observed in ^{194}Tl. The TRS calculation based on the above stated configuration shows a triaxial minimum, which can give rise to chiral geometry with proton-neutron angular momenta along the short and long axis with the core angular momenta along the intermediate axis. This makes band B5 and B5a be a potential candidate of chiral partner bands based on 5-qp configuration in this mass region.

The bands B2 and B2a based on $\pi h_{9/2} \otimes \nu i^{-2}_{13/2}$ configuration are identical to the 2-qp degenerate bands in ^{198}Tl. The TRS calculation based on the above configuration shows a triaxial minimum for this configuration in ^{195}Tl. The excitation energy separation between the bands B2a and B2 is quite high compared to the degenerate bands in ^{198}Tl. Therefore the possibility of B2a be a γ- vibrational band can not be ruled out.

5.5 Conclusion

The nuclear structure study of ^{195}Tl has been done with gamma- ray spectroscopy using fusion evaporation reaction of ^{185,187}Re target with ^{13}C beam at 75 MeV. A new and improved level scheme of ^{195}Tl has been constructed with 102 gamma- transitions among which 57 of them observed for the first time in the present work. The DCO ratio and the polarization asymmetry ratio (IPDCO) measurements have been used for the assignment of spin and parities of the levels.

The band based on $\pi h_{9/2}$ has been extended up to spin $39/2^-$ (B2) beyond first band crossing with the observation of a sideband B2a, linking to the band B2 with several interconnecting transitions. These bands are assigned $\pi \mathrm{h}_{9/2} \otimes \nu i_{13/2}^{-2}$ configuration.

The 3-qp band B4 after first band crossing changes to band B5 which is extended up to spin $43/2^-$. There is weakly populated degenerate band B5a connected to the former with several interconnecting transitions. These degenerate pair of bands B5 and B5a have been assigned $\pi i_{13/2} \otimes i_{13/2}^{-3}(p_{3/2}f_{5/2})^{-1}$ configuration. The variation of excitation energy (E_x), energy staggering, kinetic moment of inertia, alignment and B(M1)/B(E2) ratio are studied with spin(I) for these pair of degenerate bands and compared with similar degenerate bands reported in ^{194}Tl and ^{198}Tl isotopes.

From the TRS calculation based on $\pi h_{9/2} \otimes \nu i_{13/2}^{-2}$ and $\pi i_{13/2} \otimes i_{13/2}^{-3}(p_{3/2}f_{5/2})^{-1}$ configurations the bands B2-B2a and B5-B5a comes out to be based on triaxial deformation. Whereas the relatively large energy difference between bands B2 and B2a, the possibility of B2a to be γ band of B2 can not be ruled out.

Further the measurement of individual B(M1) and B(E2) reduced transition probabilities from life time measurement can give us quantitative understanding of the deformation of these bands which is beyond the scope of the present study. Also the microscopic calculation like tilted axis cranking can shed further insight into the stabilization of chiral geometry at these high angular momentum.

Bibliography

[1] R.M. Clark and A.O. Macchiavelli. Annu. Rev. Nucl. Part. Sci. **50**, 1 (2000).

[2] H. Hübel et al., Prog. Part. Nucl. Phys. **54**, 1 (2005).

[3] P.L. Masiteng et al., Phys. Lett.**B 719**, 83 (2013).

[4] E.A. Lawrie et al., Phys. Rev. **C 78**, 021305(R) (2008).

[5] R.M. Diamond and F.S. Stephens et al., Nucl. Phys. **A 45**, 632 (1963).

[6] V.T. Gritsyna and H.H. Foster et al., Nucl. Phys. **A 61**, 129 (1965).

[7] J.O. Newton et al., Nucl. Phys. **A 148**, 593 (1970).

[8] J.O. Newton et al., Nucl. Phys. **A 236**, 225 (1974).

[9] G.J. Lane et al., Nucl. Phys. **A 586**, 316 (1995).

[10] M.G. Porquet et al., Phys. Rev. **C 44**, 2445 (1991).

[11] W. Reviol et al., Physica. Scripta. **T 56**, 167 (1995).

[12] W. Reviol et al., Nucl. Phys. **A 548**, 331 (1992).

[13] R.M. Leider et al., Nucl. Phys. **A 299**, 255 (1978).

[14] N. Mărginean et al., Eur. Phys. J.**A 46**, 329 (2010).

[15] S. Dasgupta et al., Phys. Rev. **C 88**, 044328 (2013).

[16] H. Pai et al., Phys. Rev. **C 88**, 064302 (2013).

[17] H. Hübel et al., Nucl. Phys. **A 453**, 316 (1986).

[18] L. Esser et al., Phys. Rev. **C 55**, 206 (1997).

[19] P.L. Masiteng et al., Eur. Phys. J.**A 50**, 119 (2014).

[20] R. Palit et al., Nucl. Instrum. Methods Phys. Res. **A 680**, 90 (2012).

[21] H. Tan et al., in Nuclear Science Symposium Conference Record 2008 (IEEE, Washington, DC, 2008),p.3196.

[22] D.C. Radford Nucl. Instrum. Methods Phys. Res. **A 361**, 297 (1995).

[23] E.L. Brady et al., Phys. Rev. **78**, 558 (1950).

[24] A. Krämer-Flecken et al., Nucl. Instrum. Methods Phys. Res. **A 275**, 333 (1989).

[25] E.S. Macias et al., Computer Phys. Comm **11**, 75 (1976).

[26] H. Pai et al., Phys. Rev. **C 85**, 064317 (2012).

[27] K. Starosta et al., Nucl. Instrum. Meth. Phys. Res. **A 423**, 16 (1999).

[28] Ch. Droste et al., Nucl. Instrum. Meth. Phys. Res. **A 378**, 518 (1996).

[29] A.J. Kreiner et al., Nucl. Phys. **A 308**, 147 (1978).

[30] K.H. Hicks., et al., Phys. Rev. **C 25**, 2710 (1982).

[31] J. Meyer-ter-Vehn et al., Phys. Rev. Lett. **32**, 1383 (1974).

[32] J. Meyer-ter-Vehn et al., Nucl. Phys. **A 249**, 111 and 141 (1975).

[33] I. Hamamoto Phys. Lett. **B 193**, 399 (1987).

[34] I. Hamamoto Phys. Lett. **B 235**, 221 (1990).

[35] A.K. Jain and A. Goel Phys. Lett. **B 277**, 233 (1992).

[36] R. Bengston et al., Nucl. Phys. **A 309**, 158 (1982)

[37] A.J. Kreiner Phys. Rev. **C 22**, 2570 (1980).

[38] H. Toki et al., Phys. Lett. **B 71**, 1 (1977).

[39] R.M. Leider et al., Nucl. Phys. **A 248**, 317 (1975).

[40] S. Frauendrof and J.Meng et al., Nucl. Phys. **A 617**, 131 (1997).

[41] S. Frauendrof Rev. Mod. Phys. **73**, 463 (2001).

[42] J. Timer Phys. Lett. **B 598**, 178 (2004).

[43] S. Zhu et al., Phys. Rev. Lett. **91**, 132501 (2003).

[44] S. Mukhopadhyay et al., Phys. Rev. Lett. **99**, 172501 (2007).

[45] W. Nazarewicz et al., Nucl. Phys. **A 435**, 397 (1985).

[46] W. Nazarewicz et al., Nucl. Phys. **A 512**, 61 (1990).

[47] G. Mukherjee et al., Nucl. Phys. **A 829**, 137 (2009).

Chapter 6

Summary and outlook

6.1 Summary

In the present work prompt coincident γ- ray spectroscopy in ^{195}Tl and recoil gated decay spectroscopy including life-time measurements have been performed for ^{193}Bi and ^{195}Bi nuclei using clover HPGe detectors and recoil spectrometer (with associated focal plane recoil detection system), respectively. Theoretical calculations have also been performed in this thesis work in the microscopic-macroscopic approach in the cranked shell model formalism using Woods-Saxon potential to interpret the data. The high spin level structure has been improved considerably with the observation of several new band structures, identification of band crossing above the ground state band based on $\pi h_{9/2}$ orbital, definite spin and parity assignment to the levels in ^{195}Tl and observation of a new high spin isomer of life-time ($T_{1/2}$) 1.6(1) μs and its decay in ^{195}Bi along with a known 3.02(8) μs isomer in ^{193}Bi have been observed.

The high spin states of ^{195}Tl has been populated via ^{185,187}Re(^{13}C, xn)^{195}Tl fusion evaporation reaction at 75 MeV beam energy at TIFR-BARC pelletron facility, Mumbai with 15 HPGe clover detectors with BGO anti-Compton shield of Indian National Gamma Array (INGA). Time stamped digital DAQ system based on Pixie-16 modules were used for data acquisition in two or more gammas in coincidence mode. In the the analysis γ-γ coincidence matrix and γ-γ-γ cube were made to obtain the coincidence relation among the γ- rays for building the level scheme. Angle dependent asymmetry matrix were constructed for DCO and IPDCO ratio measurement to assign definite spin and parity to the earlier known nuclear states along with the new ones.

Heavy ion induced reaction was employed for the first time in the present study, allowed us to explore the high spin regime and extend our knowledge considerably on the high spin states in ^{195}Tl. A total of 57 new gamma- transitions are arranged in several new band structures. The ground state band (B1) based on $\pi h_{9/2}$ orbital has been extended upto spin $39/2^-$ and with this, it was possible to observe, for the first time, the band crossing due to particle alignment and extend this band beyond band crossing as 3-quasi-particle band (B2). Also a side band (B2a) close to the Band B2 has been identified which are quite identical in terms of excitation energy, gain in alignment (i_x), kinetic moment of inertia (J$^{(1)}$) and B(M1)/B(E2) transition probability ratio. These two bands are based on $\pi h_{9/2} \otimes \nu i^{-2}_{13/2}$ configuration. The TRS calculation shows a triaxial minimum for this configuration which does not rule out the possibility of band B2a to be a gamma band of B2. The 3-qp band B4 has been extended beyond band crossing (levelled as band B5) up to spin $43/2^-$ with the observation of a weakly populated side band B5a. The band B5a is connected with band B5 with several interconnecting transitions. These two bands are very close to each other in excitation energy varying from 59 keV at spin $35/2^-$ to -6 keV at spin $43/2^-$. The gain in alignment (i_x), kinetic moment of inertia ($J^{(1)}$) and B(M1)/B(E2) transition probability ratio are quite similar for these two bands. The TRS calculation done based on $\pi i_{13/2} \otimes i_{13/2}^{-3}(p_{3/2}f_{5/2})^{-1}$ configuration for these bands shows a triaxial minimum which makes them to be a potential candidate of degenerate bands based on 5-qp configuration.

Candidate of degenerate bands have been reported in recent years in the odd-odd Tl nuclei (e.g., ^{194}Tl, ^{198}Tl) in this mass region but it would be for the the first time that such candidate partner bands have been seen in an odd-A nucleus in this region. The near degenerate bands in ^{195}Tl have been compared with those in ^{194,198}Tl. Several other band structures have been observed in this nucleus.

Isomer decay study of ^{193,195}Bi isotopes has been carried out at the focal plane of gas-filled HYbrid Recoil mass Analyzer (HYRA) at IUAC, New Delhi. The high spin states in these nuclei were populated using fusion evaporation reaction of ^{30}Si on ^{169}Tm (0.8 mg/cm^2) target at 168 and 145 MeV beam energy, respectively. The focal plane chamber consisted of one MWPC, three Si- pad detectors and one HPGe clover detector outside the chamber. To detect prompt γ- rays one HPGe clover detector was placed at the target site. The time and pulse height information of each γ- rays both in focal plane and target site detectors were recorded event by event basis using CAMAC- based data acquisition system. HYRA was used for the first time for the measurement of isomeric half-life and its decay. In order to validate the method and the set up, decay of a known 3 μs isomer in ^{193}Bi was measured in the beginning and the known decay gamma- rays from this isomer were observed. The half-life of the isomer was also remeasured in the present work and found to be in excellent agreement with the previous measurement. Moreover, new gamma- rays of energy 186- and 279- keV were identified in ^{193}Bi in this work, which were later confirmed by Herzáň et al. [1]. In ^{195}Bi a new high spin isomer of life-time ($T_{1/2}$) 1.6(1) μs at an excitation energy of 3336 keV has been identified, apart from the 700 ns (J^{π}=(29/2^{-})) earlier known isomer. The spin and parity of the new isomer has been assigned as (31/2^{-}) with three quasi-particle configuration $\pi i_{13/2} \otimes \nu_{9^{-}}$. The TRS calculations show an oblate deformation (γ=-60^{0}) with $\beta_2 \sim 0.12$ for this isomer.

From the experimental work along with the theoretical calculations done in the present thesis work, there are two main outcome: First we get a better idea about the relative deformation driving effects of the high-j $h_{9/2}$ and $i_{13/2}$ proton orbitals. The intruder $h_{9/2}$ orbital in ^{195}Tl, has rather strong effect in deforming the system which persist up to high spin through neutron alignments. No deformed band structure based on $i_{13/2}$ proton orbital could be observed in this nucleus. This suggests that the proton $h_{9/2}$ orbital has more shape driving effect than the $i_{13/2}$ orbital. This is also supported by the fact that deformed band structure based on $h_{9/2}$ orbital in near proton closed shell Tl isotopes could be observed even up to ^{201}Tl (i.e., upto neutron number N = 120, close to the N = 126 spherical shell closure). Whereas, the deformed band structure based on $i_{13/2}$ orbital could be observed only up to N = 112 isotope ^{193}Tl. Similar conclusion could be drawn from the Bi nuclei as well in which the deformed band structure built on $i_{13/2}$ proton orbital has been observed for the lighter isotopes with an onset of deformation at neutron number N = 112 in ^{195}Bi isotope. On the other hand, the calculations suggest that the long lived high-spin isomeric state, with the configuration of an $i_{13/2}$ proton coupled with two-neutron 9^{-} state, observed in this work is a band head of a deformed oblate structure. However, no rotational band structure could be observed in the heavier isotopes in this nucleus with N > 112. Therefore, it can be concluded that the proton $i_{13/2}$ orbital has deformation driving effect only for neutron number N $\leq$ 112. In the single particle diagram for neutrons, it can be seen that neutron $i_{13/2}$ orbital is completely filled at N = 114 and hence, the neutron $i_{13/2}$ orbitals are unfilled and become active for N < 112. Therefore, the deformation driving effect of proton $i_{13/2}$ orbital is realized only when supported by high-j neutron $i_{13/2}$ orbital. But for $h_{9/2}$ proton orbital can deform a system even without such support from neutron orbitals. Secondly, the high-spin phenomena in Tl nuclei, situated below the Z = 82 spherical spherical shell closure, are richer in variety of observed phenomena than in Bi isotopes which lies above the shell closure. This is evident from the observation of rich variety of phenomena like bands based on oblate deformation, band crossing, chiral partner bands etc., observed in a single nucleus ^{195}Tl. Moreover, the observation of the long-lived isomer in ^{195}Bi in the present study helps to understand the issue of non-observation of high spin levels in this nucleus which was limited up to 2.9 MeV of excitation energy prior to the present work. After the present work, the level scheme of ^{195}Bi has been extended in the thesis work of Herzáň [4].

6.2 Future outlook

Deformed band structure based on $\pi h_{9/2}$ orbital has been observed in odd-A Tl (Z=81) isotopes in A $\sim$ 190 mass region. Based on total Routhian surface calculations of these isotopes it was conjectured that they are based on oblate deformation. Till now there is no life-time measurement of states of band based on deformed proton $h_{9/2}$ orbital. Recently, in odd-odd ^{194,198}Tl isotopes doubly degenerate bands are reported based on triaxial deformation [2,3]. Also there are some triaxial core plus particle rotor model [5–8] calclulations in ^{194,198}Tl isotopes which can interpret the experimentally observed nuclear energy levels quite well. Therefore, it will be interesting to have life-time measurement of these deformed band structures of respective isotopes. These will give quantitative information regarding their deformation and shape driving effect of the proton $h_{9/2}$ orbital.

Also the bands B5 and B5a in ^{195}Tl, appears to be doubly degenerate. In order them to be degenerate bands, they should be formed on triaxial deformation with proton particle angular momentum ($\mathbf{j}_\pi$) along the the short(s) axis, neutron hole angular momentum ($\mathbf{j}_\nu$) along the long(l) axis and core rotational ($\mathbf{R}$) angular momentum along the intermediate(i) axis. Thus it is important to have information about B(M1) and B(E2) transition probability through life-time measurement for conclusive idea about the orbitals involved in forming these bands along with their deformation. At the same time Tilted Axis Cranking (TAC) calculation is required for better understanding of the nature of these bands.

The TRS calculation done for ^{195}Bi indicates an oblate deformation for newly observed 3 quasi-particle ($\pi i_{13/2} \otimes \nu_{9^-}$) isomer in the present study, suggesting a shape driving effect of the $\pi i_{13/2}$ orbital. Therefore, it is quite possible to have rotational band structure above this isomer. Further investigation is required for the search of deformed band structure above this isomer by prompt and delayed coincidence method. However, in a recently unpublished result of ^{195}Bi suggest to have an isomer of life-time 1.49(1) μs (quite similar to our new isomer of life-time 1.6(1) μs) at an excitation energy of 2615 keV (I^π=29/2$^+$) with configuration $\pi i_{13/2} \otimes \nu_{8^+}$ [4]. Therefore it will be interesting to study, whether there is two or one isomer and their configuration can be ascertain unambiguously by g-factor measurement.

In the present work, it has been concluded that the deformation driving effect of the $\pi i_{13/2}$ orbital is effective to manifest rotational band structure in nuclei with neutron number N < 112 i.e., when supported by active holes in $\nu i_{13/2}$ orbital. This conclusion was based on the observation of high spin states in Bi and Tl isotopes. However, the proton $i_{13/2}$ orbital is quite accessible for At (Z = 85) and Fr (Z = 87) isotopes but there is no data for high spin states in these nuclei. Therefore, it will be interesting to look for states above the $\pi i_{13/2}$ orbital in At and Fr isotopes (N $\leq$ 112) to see whether high-j, $\nu \mathrm{i}_{13/2}$ orbital supports the deformation driving effect in proton $i_{13/2}$ orbital in these isotopes as seen in Tl and Bi isotopes.

Bibliography

[1] A. Herzáň et al., Phys. Rev. **C 92**, 044310 (2015).

[2] P.L. Masiteng et al., Phys. Lett. **B 719**, 83 (2013).

[3] E.A. Lawrie et al., Phys. Rev. **C 78**, 021305(R) (2008).

[4] A. Herzáň Ph.D. thesis, University of Jyväskyl*ä*, (2015).

[5] J. Meyer-ter-Vehn., et al., Phys. Rev. Lett. **32**, 1383 (1974).

[6] J. Meyer-ter-Vehn., et al., Nucl. Phys. **A 249**, 111 (1975).

[7] R.M. Leider et al., Nucl. Phys. **A 299**, 255 (1978).

[8] H.L. Yadav, et al., Phys. Rev. Lett. **39**, 1128 (1977).